Design and Implementation of a W-Band Single-Antenna Frequency-Modulated Continuous-Wave Radar Front-End System-on-Chip for Automotive Applications

by

Milad KALANTARIMAHMOUDABADI

A Thesis Submitted to

The Hong Kong University of Science and Technology
in Partial Fulfillment of the Requirements for
the Degree of Doctor of Philosophy
in the Department of Electronic and Computer Engineering

December 2019, Hong Kong

Authorization

I hereby declare that I am the sole author of the thesis.

I authorize the Hong Kong University of Science and Technology to lend this thesis to other institutions or individuals for purpose of scholarly research.

I further authorize the Hong Kong University of Science and Technology to reproduce the thesis by photocopying or by other means, in total or in print, at the request of other institutions for the purpose of scholarly research.

Milad KALANTARIMAHMOUDABADI

19 December 2019

Design and Implementation of a W-Band Single-Antenna Frequency-Modulated Continuous-Wave Radar Front-End System-on-Chip for Automotive Applications

by

Milad KALANTARIMAHMOUDABADI

This is to certify that I have examined the above PhD thesis and have found that it is complete and satisfactory in all respects, and that any and all revisions required by the thesis examination committee have been made.

Professor Chik Patrick YUE, Supervisor

Professor Kevin CHEN, Acting Head of Department

Thesis Examination Committee

Prof. C Patrick YUE (Supervisor)
 Department of Electronic and Computer Engineering
 Prof. Ross MURCH
 Department of Electronic and Computer Engineering
 Prof. Howard Cam LUONG
 Lilong CAI
 Department of Electronic and Computer Engineering
 Department of Mechanical and Aerospace Engineering
 Prof. Jri LEE
 National Taiwan University

Department of Electronic and Computer Engineering

December 2019

Acknowledgments

I would like to express my most sincere gratitude and appreciation to my supervisors Prof. Patrick Yue and Prof. Ali Fotowat for their full support and guidance during my research at the Hong Kong University of Science and Technology and Sharif university of Technology. Without their foresight and encouragement, I was not able to finish the maze track of my Ph.D.

I thank the members of our research group at HKUST Qualcomm Optical Wireless Lab (HQ-OWL), Dr. Duona Luo, Dr. Guang Zhou, and Prof. Xiangyu Meng (Andy) for technical and scientific discussions that we had during these years. Special thanks to Babar Hussain and Wang Li, as my always supportive friends.

Last but not least, I would like to thank my lovely parents and my sisters who have been always my engine in the journey of my life. Dedicated to them with love, as a small gift instead of their priceless support.

Contents

\mathbf{A}	utho	zation	i
Si	\mathbf{gnat}	re Page	iii
\mathbf{A}	ckno	${f ledgments}$	v
\mathbf{A}	bstra	${f t}$	viii
1	Intr	$\mathbf{duction}$	1
	1.1	Automotive Radar	5
2	Rac	ar principle	9
	2.1	Radar equation	9
	2.2	False alarm rate and probability of detection	11
	2.3	Pulse integration	12
	2.4	Range resolution	14
	2.5	Range ambiguity and minimum detectable range	15
	2.6	Doppler and velocity resolution	16
	2.7	Continuous-wave radars	18
		2.7.1 FMCW radars	18
		2.7.2 Doppler frequency shift in FMCW radars	20
		2.7.3 Range and velocity resolution in FMCW radars	20
	2.8	Conclusion	21

3	\mathbf{Sys}	tem ar	d RF specifications for the automotive radar	23
	3.1	Choos	ing the radar type	25
	3.2	Dynar	nic range in radars	27
	3.3	Noise	in FMCW radars	30
		3.3.1	Thermal noise of the RX	31
		3.3.2	Flicker noise	31
		3.3.3	Thermal noise of the TX	32
		3.3.4	PN of the oscillator	33
	3.4	Concl	ısion	36
4	Sing	gle-ant	enna architecture	39
	4.1	Motiv	ations	39
	4.2	Sharin	g a single antenna and the TX leakage issue	41
	4.3	Dynar	nic range enhancement techniques in FMCW radars	45
		4.3.1	Feedback analysis of the RPC	47
		4.3.2	Noise analysis of the closed-loop receiver	48
		4.3.3	Effect of IQ-imbalance on the leakage cancellation performance	50
		4.3.4	Stability of the feedback loop in the cancellation architecture	55
		4.3.5	System level implementation of the RPC	56
	4.4	Propo	sed cancellation technique	58
5	Des	ign an	d simulation of building blocks	63
	5.1	Transı	mission line structure	64
	5.2	Anten	na coupler	64
	5.3	LNA		65
	5.4	IQ-de	nodulator	70
	5.5	Phase	compensator	74
	5.6	Varial	ole reflector (VR)	75
		5.6.1	Proposed arbitrary phase and amplitude hybrid coupler	78
		562	Proposed VP	89

	5.7	TX block	. 83
	5.8	TRX simulations	. 84
6	Mea	asurement	91
	6.1	Probe measurements	. 92
		6.1.1 TX block	. 92
		6.1.2 RX block	. 96
	6.2	Field tests	. 102
	6.3	Performace summary	. 107
7	Con	nclusion	111
	7.1	Future works	. 112
A	crony	ym Glossary	114
Bi	blios	vranhv	116



List of Figures

1-1	Applications of the mm-wave sensors in (a) security monitoring, (b) auto-	
	motive safety, and (c) vital signal detection	2
1-2	Average attenuation level of electromagnetic waves in the air [1]	3
1-3	Radar miniaturization trend	4
2-1	A simple radar waveform	10
2-2	(a) Omnidirectional, and (b) directive wave propagation	10
2-3	PD versus SNR for different FARs [2]	12
2-4	Incident of a burst of electromagnetic wave to the targets	14
2-5	Received signal from two targets	15
2-6	Transmitted pulses with a specified pulse width and PRI	16
2-7	(a) Transmitted signal, (b) Received signal with Doppler frequency shift	17
2-8	Sinc function.	18
2-9	Transmitted and received signals in an FMCW radar	19
2-10	Transmitted and received signals in the presence of the Doppler effect in	
	FMCW radars	20
3-1	Reflection of a target, covered the whole antenna beam, such as a flat mirror.	29
3-2	Minimum and maximum received power versus target distance for LRR	29
3-3	Minimum and maximum received power versus target distance for MRR. $$.	30
3-4	Minimum and maximum received power versus target distance for SRR	30
3-5	Block diagram of an FMCW radar transceiver	31
3-6	Noise in the TX.	33
3-7	A worst-case scenario for studying the PN effect	34

3-8	Output spectrum of the baseband signal in the (a) absence, and (b) pres-	
	ence of the PN	34
3-9	PN requirement for LRR, MRR and SRR in the worst-case scenario	36
4-1	(a) A conventional phased-array radar TRX. (b) A single-antenna-based	
	phased-array radar TRX	40
4-2	Range improvement ratio of the single-antenna-based phased-arrays to con-	
	ventional phased-arrays with the same array size and a similar performance	
	of the TXs and RXs	41
4-3	Sharing the antenna port using (a) a circulator and (b) a directional coupler	
	in a single-antenna front-end	42
4-4	Leakage cancellation schemes using (a) impedance tuning, and (b)cancellation	
	path	44
4-5	Block diagram of a FMCW radar TRX using an SFC	46
4-6	Feedback architecture to the relax RF dynamic range of the receiver in	
	FMCW radars	47
4-7	Simplified model of the feedback circuit	47
4-8	Noise sources in the feedback model	49
4-9	(a) PN cancellation at the IF port in a down-converter due to PN correla-	
	tion effect. (b) PN modulation in an up-converter	50
4-10	AN and PN of the TX in the RPC	51
4-11	Limited open-loop image-rejection due to IQ-imbalance	51
4-12	Image-rejection in the closed-loop operation	52
4-13	Closed-loop versus open-loop image-rejection ratio for the different loop	
	gains	54
4-14	Cancellation factor versus open-loop image-rejection ratio for the different	
	loop gains	54
4-15	Full block diagram of the closed-loop single-antenna architecture	56
4-16	Schematic diagram of IQ-modulator, summing node and antenna coupler	57
4-17	Block diagram of the proposed leakage cancellation architecture	59

5-1	Simplified cross section of 65-nm process used in the EM-simulations	64
5-2	Simulated insertion loss and matching of CPW t-line	65
5-3	Schematic, layout, and simulation results of the 90° hybrid coupler	66
5-4	Cutoff frequency (f_t) versus current density of a 10 μ m NMOS transistor	67
5-5	Transconductance (g_m) versus current density of a 10 μ m NMOS transistor.	67
5-6	Differential transistor configurations suitable for a high frequency, low noise	
	amplifier design: (a) common source, (b) cascode and (c) common source	
	with neutralization capacitors	69
5-7	Stability criteria (k-factor) of the standard RF-NMOS transistors versus	
	frequency for different transistor topologies.	69
5-8	Minimum noise figure versus frequency for a common source, cascode and	
	common source with neutralized gate-drain capacitor configurations	70
5-9	Maximum stable power gain of a minimum length (60-nm) RF NMOS	
	transistor with a width of 10- μ m	70
5-10	(a) Schematic, and (b) 3D-layout view of a three-stage fully differential	
	transformer-based LNA. (c) 3D layout of the differential pair, including	
	the cross-capacitors	71
5-11	Simulated Gain, NF and Stability factor for the LNA in different corners	72
5-12	IQ-demodulation using (a) RF path quadrature generation, and (b) LO	
	path quadrature generation	72
5-13	RF path quadrature generation using a 90° hybrid coupler for the IQ-	
	$\ demodulator. \ \ldots \ldots \ldots \ldots \ldots \ldots$	73
5-14	Schematic of the IQ demodulator	74
5-15	Simulated (a) conversion gain and NF, and (b) IQ-imbalance of the IQ-	
	$\ demodulator. \ \ldots \ldots \ldots \ldots \ldots \ldots$	75
5-16	Block diagram of the phase compensator	75
5-17	Schematic of the proposed VR	76
5-18	Coverage area of the input reflection coefficient of the VR on the Smith	
	chart	77

5-19	Proposed schematic of a hybrid coupler with arbitrary phase and amplitude.	78
5-20	Equivalent circuit model for even-odd mode analysis	78
5-21	(a) Simulated S-parameters of the proposed 45° hybrid coupler. (a) Am-	
	plitude response. (b) Phase response	83
5-22	Schematic and layout of the proposed VR circuit at 80 GHz	84
5-23	Schematic of the transmitter	85
5-24	Simulated locking range of the ILFT versus controlling digital bits	85
5-25	The layout of the chip	86
5-26	Simulated conversion gain and SSB NF of the single-antenna TRX with	
	the closed-loop leakage cancellation	87
5-27	Simulated chip output power, SSB NF, and conversion gain of the RX	
	versus LO frequency	88
5-28	Simulated chip output power, RX conversion gain and receiver noise figure	
	versus antenna port's matching for the 360° phase sweep	89
6-1	Schematic of the supply regulators on the FR-4 low frequency PCB	92
6-2	Schematic of baseband amplifiers with 40 dB of differential to single-ended	
	voltage gain	93
6-3	W-band single-antenna radar front-end module including the chip, on-PCB	
	antenna, baseband amplifiers, and voltage regulators	94
6-4	Programming the internal shift register of the chip using the GUI app and	
	the Labjack serial programmer	95
6-5	Chip microphotograph of the fabricated chip on 65 nm CMOS technology.	96
6-6	Measurement equipment	97
6-7	TX measurement setup	98
6-8	Measured frequency locking range and the output power of the TX	98
6-9	SSB Phase noise performance of Agilent E8527D	99
6-10	Measured PN of the TX in the locking and unlocking conditions	99
6-11	Measurement setup for RX conversion gain and NF	LOC
6-12	Measured conversion gain and NF of the RX	100

6-13	Measurement setup for characterization of the RX cancellation 1	.01
6-14	Measured adaptive cancellation characteristic of the proposed closed-loop	
	leakage cancellation RX	01
6-15	(a) Manufactured chip on the radar PCB module using bonding wires. (b)	
	Simulated input matching of the antenna, including the half wavelength	
	bonding wire transition. (c) Simulated radiation pattern of the 4×8 patch	
	antennas array	04
6-16	${\it Measurement setup for demonstration of the proposed single-antenna FMCW}$	
	radar operation	L05
6-17	Detection of a 40 cm \times 50 cm metal sheet using the proposed radar chip at	
	a distacne of (a) 6.25 m, (b) 12.5 m and (c) 19 m	L06
6-18	Detection of a flying drone using the proposed radar chip at a distacne of	
	(a) 2.5 m, and (b) 10 m	107



List of Tables

3.1	Automotive radar classification and specification	24
3.2	Radar types comparison	27
3.3	Dynamic range requirement for LRR, MRR and SRR	29
5.1	List of equations and values of the components for the proposed hybrid	
	coupler with arbitrary phase and amplitude	32
5.2	Supply voltages and current consumption of the chip	35
5.3	Number of pads and types	36
5.4	Digital pads	37
6.1	Performance summary and comparison to the previous arts)8
6.2	Comparison with two commercialized products)9

Design and Implementation of a W-Band Single-Antenna Frequency-Modulated Continuous-Wave Radar Front-End System-on-Chip for Automotive Applications

by Milad KALANTARIMAHMOUDABADI

Department of Electronic and Computer Engineering
The Hong Kong University of Science and Technology
Abstract

Millimeter-wave sensors are a promising technology that can enrich human's quality of life by bringing the next level of awareness and sensing to the smart devices. Thanks to the advanced nanoscale CMOS technology as a core of high-performance digital circuits, low-cost CMOS transistors can operate up to terahertz frequencies, which opens up this opportunity for designing mm-wave system-on-chips (SoCs). As a result of the higher frequency, bulky radar sensors which have been traditionally used in limited applications can be implemented within hand size boxes. This miniaturization has been ever continued so that the antenna is integrated on the chip with the transceiver and other parts of the system. Among different applications for the mm-wave radars, automotive radars in Wband have been studied in this dissertation as vital sensors in the active safety monitoring and the autonomous driverless vehicles. While phased-array transceivers, on-chip antennas, and fully integrated radar chips have been the focus of the past reported literature, in this thesis we emphasize to further reduce the size and cost of the radar sensor by adopting a single-antenna approach. We propose an adaptive leakage cancellation scheme to improve the isolation level of a single-antenna architecture for frequency-modulated continues-wave (FMCW) radars at the mm-wave frequencies. Our suggested architecture employs an analog closed-loop feedback circuit to flexibly track and nullify leakage signals at the input of the receiver. The proposed transceiver was implemented in 65-nm CMOS and was measured at 80 GHz. Besides, a radar module using the chip attached to an on-PCB antenna was fabricated. A metallic object (40cm×50cm) was detected within a range of 19 m which demonstrates our approach is capable of being used in short-range automotive applications.

Chapter 1

Introduction

In this chapter, a brief introduction to the millimeter wave mm-wave band is given and its potential applications are demonstrated. Then automotive radar as a specific application will be covered.

The frequency range of 30-300 GHz with the corresponding wavelength of 0.1-10 mm is called the mm-wave band. There are many applications such as high-speed wireless communications (802.11ad standard [3]), mm-wave radar for automotive (Fig. 1-1(b)), mm-wave imaging for security system (Fig. 1-1(a)) [4-9], and vital sign detection systems [10-12] in the mm-wave frequencies (Fig. 1-1(c)). Today, because of the advancement of the semiconductor industry, analog circuit designers are benefiting from scaling and improvement of the frequency response of nano-scaled CMOS transistors, which makes it possible to design circuits and systems at mm-wave frequencies. Unique features that make the mm-wave band attractive for analog and system designers are as follows.

1. Large bandwidth: The increasing demand for higher data rate has been a driving force to system designers. One of the big challenges from the 1st to 5th generation of wireless communication systems is the assignment of the limited bandwidth in the frequency range of less than few gigahertz to the users. However, there is much more bandwidth available in the mm-wave band comparing to UHF or microwave frequencies. For example, there is only 1 GHz bandwidth from dc to UHF band while in the 60 GHz unlicensed band, a 4 GHz bandwidth is already available.



Fig. 1-1. Applications of the mm-wave sensors in (a) security monitoring, (b) automotive safety, and (c) vital signal detection.

According to Shannon's theory [13], increasing the bandwidth results in a higher data rate and this is the main motivation for system designers to move toward mm-wave technology.

2. Higher propagation loss: The attenuation of electromagnetic waves versus frequency of the electromagnetic waves is depicted in Fig. 1-2. There are several spikes in the attenuation characteristics of the air due to the wave absorption by oxygen and H₂O molecules at these frequencies. Traditionally, in the long-range wireless systems, it is not desirable to have any extra attenuation since it requires higher transmit power. Specifically, at the mm-wave band, generating a high level of power is a big challenge. However, this attenuation helps to reduce the interference signals of the other transceivers (TRXs) working simultaneously at the same frequency band. Therefore, better spatial diversity and more efficient frequency reuse are possible,

which are suitable for high data rate short-range wireless links such as wireless HDMI.

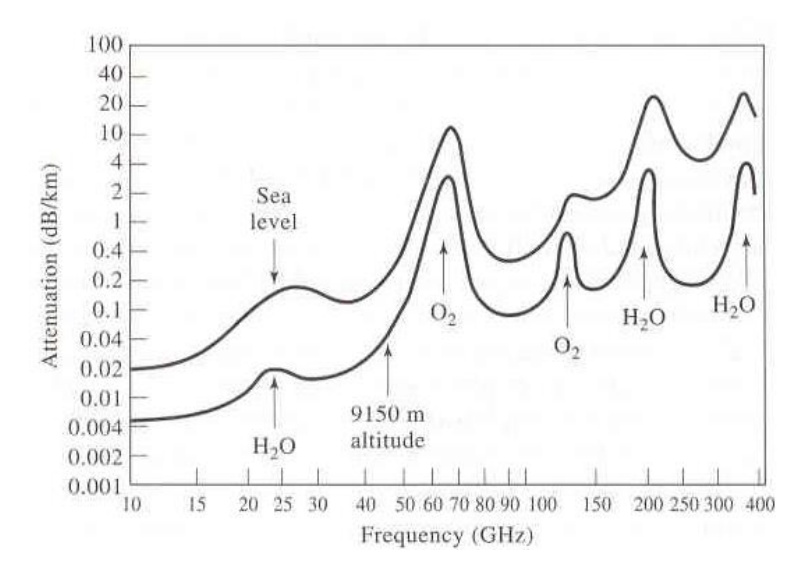


Fig. 1-2. Average attenuation level of electromagnetic waves in the air [1].

3. Lower size of passive circuits and antennas: As we know, the size of passive components is inversely proportional to the operating frequency of a circuit. The higher the frequency, the smaller the passive component size. Therefore, another important motivation for circuit and system designers is to reduce the size of the bulky passive components such as antennas. More specifically, the antenna performance and radiation pattern can be well controlled using miniaturized phased array systems at the mm-wave band. In this regard, studies have been conducted in the past years showing the feasibility of the on-chip antennas for automotive radars and imaging systems at the mm-wave band [4–6]. Utilizing higher gain antennas reduces the interference and relaxes the transmitter's output power for the communication systems as well as obtains better angular resolution for radars and imaging systems [7–9].Fig. 1-3 shows this miniaturization trend for the radars thanks to the mm-wave band. In this dissertation, we will address even more miniaturized radar sensor by proposing a single-antenna architecture.

While the overview shows the motivations and opportunities of mm-wave technology, it is not as straight forward as it seems at first glance. Some of the challenges that arise in this regime are as follows.

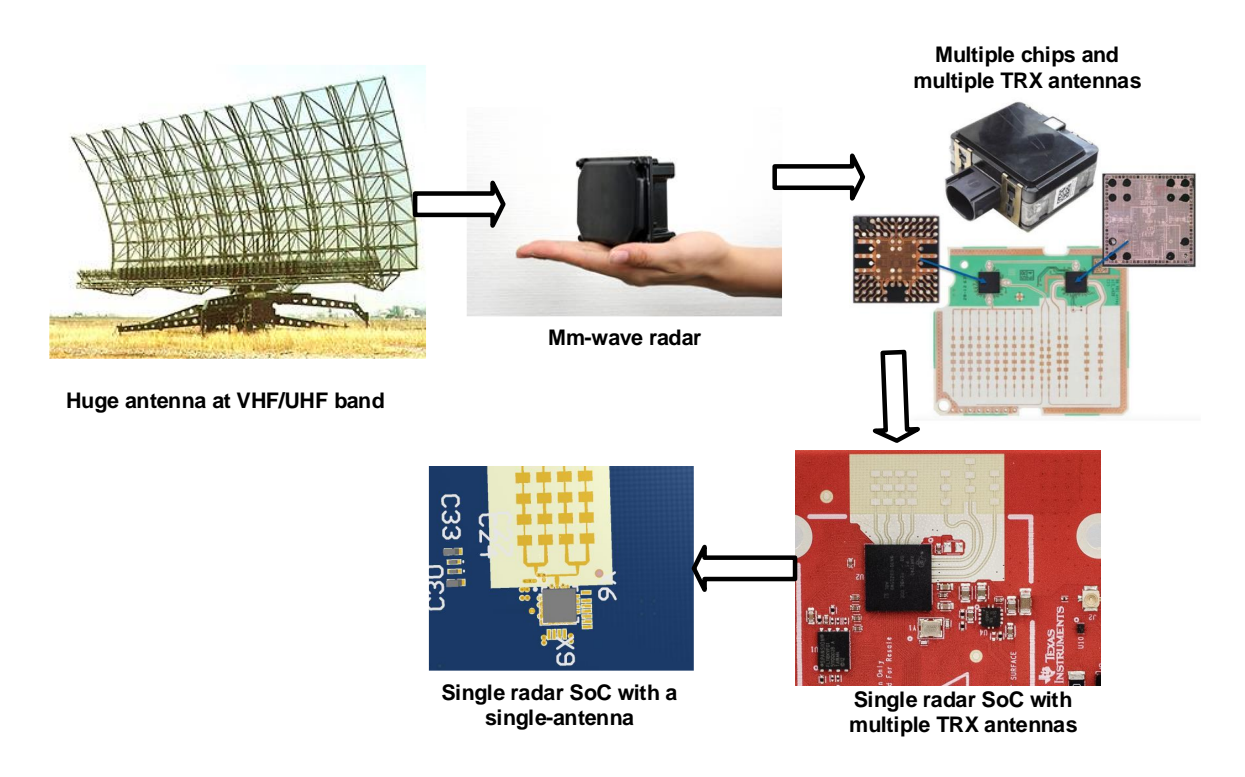


Fig. 1-3. Radar miniaturization trend.

- 1. Power generation issue: Although device scaling brings improvement in terms of frequency response and integration level, the breakdown voltage of the devices is reduced in advanced CMOS technology. The lower breakdown voltage of CMOS compared to compound semiconductors causes lower power generation at the mmwave band, which needs to be addressed [6, 14, 15].
- 2. Lack of accurate model for devices: The high-frequency circuits are generally more vulnerable to the parasitic effects compared to the lower frequency designs. Therefore, having a properly modeled device is an essential rule for designers at higher frequencies. Measurement-based models are usually employed for achieving better accuracy in simulations. However, typically manufacturers can only provide a limited number of devices and components with specific sizes and shapes that are modeled using measurement-based techniques and the frequency of the measurement usually doesn't cover whole the mm-wave band. Therefore, a careful technique for modeling and simulating the circuits is required.
- 3. Component losses: The loss of the passive devices due to additional loss mech-

anisms, such as skin effect, poly gate resistance of the transistors and substrate conductivity, rises significantly at the mm-wave band. The skin effect causes addition resistive loss in the transmission lines and reduces the quality factor of the passive components, which results in higher attenuation, a higher noise figure (NF) and lower power efficiency of the system. Moreover, the poly gate oxide of the transistors turns to a lossy component at mm-wave frequencies, which requires to be driven by the previous stages. All these mechanisms besides the lower capability of power generation make the design very challenging. The lossy substrate of CMOS technology will be added to the above losses, making it even more challenging for this frequency band.

With respect to the attractiveness and challenges, the mm-wave is a potential research interest for circuit and system designers because of:

- 1. From the circuit designer point of view, the mm-wave has not reached its maturity on CMOS technology.
- 2. From the system designers point of view, it is possible to define and design novel ideas and applications with a higher performance, higher data rate and smaller form factor compared to traditional systems.

In the following section, the automotive radar as a specific application at the mm-wave band is briefly described, and the challenges and opportunities are introduced.

1.1 Automotive Radar

Autonomous vehicles are a promising technology, which can enrich people's life by improving the safety and energy efficiency of the vehicles. Today, thanks to the efforts of the different branches of science and technology, fully autonomous driverless cars are becoming more practical than ever before. In addition to the huge data processing required for a car to be fully driverless, a network of sensors is an inevitable part of this system in order to collect the environmental information and send it to a processor unit. An active

safety radar or automotive radar can detect the objects in front of a car and can alert the driver before a collision. This was not easily achievable at a low price and proper size until 1999. To show the importance of the radar systems for the automotive application, first we should answer the question: "why radar?"

Camera-based optical systems, lidars (light detection and ranging), and radars are three main different methods for monitoring objects around a car [16,17]. With the advent of powerful processors and digital cameras, optical vision systems, and image processing have been a very attractive field of research with relatively low cost. While the camerabased systems can capture details such as the shape and color of the surrounding objects, they suffer from direct distance measurement and need to use processing algorithms to estimate the distance of the obstacles, which is vital data for the processor in order to take appropriate reactions. In addition, the performance of the optical vision systems strictly depends on environmental factors such as light (day/night) and weather conditions (fog/dust/rain/snow), which reduce the reliability and safety of the systems for such a critical task [18, 19]. Lidars, as a promising technology can measure distance; however, they can be harmful to the human eye due to the laser beam, and need careful selection of the wavelength. Moreover, similar to the optical vision systems, their operation is prone to degradation in bad weather situations. Radars, on the other hand, can measure distance directly and detect objects with lower sensitivity to environmental factors. Traditionally, due to cost, complexity, and size of the radars, they have been used in limited applications such as military systems, airborne traffic monitoring systems and weather prediction for many years.

Recently, several fully integrated mm-wave radars on CMOS and BiCMOS technologies were reported at the 77 GHz band, which is assigned for the automotive radar application [20–30]. In [21], a fully-integrated frequency modulated continuous wave (FMCW) radar TRX chip is presented at 77 GHz on CMOS. The focus of this work is on the integration of the different building blocks including transmitters (TXs), receivers (RXs) and signal generation parts to build a low-cost high-performance chip. An 8-channel RX and 8-channel TX phased array front-end is implemented in [31] on SiGe BiCMOS technology.

The RF phase shifting technique utilized in this work provides electronically beam steering capability and high linearity at 76-85 GHz. In [5,6] a compact phased-array TRX is demonstrated, which uses on-chip dipole antennas and extra post-processing to the standard CMOS technology to attach a dielectric lens to the chip for further improvement of the antenna performance. While utilizing an antenna on chip brings a high level of integration, functionality, repeatability, and reliability, the efficiency of the on-chip antenna is still a bottleneck to make it useful for the automotive application. Texas Instruments commercialized the first fully integrated radar on a chip [32] in 2018. The chip integrates three TXs, four RXs, signal generation, and baseband ADCs on 40-nm CMOS technology, operating at 80 GHz.

While the feasibility of the integrated phased array, on-chip antenna, and signal generation were proven in the previous works, further size and cost reduction, and performance improvement are achivable by adopting a single-antenna approach. Despite using a higher frequency, the size of the system is yet dominated by the antenna size [33]. Most of the previous reported radar chips at the mm-wave band uses two separate antennas for the TX and RX. This is necessary for continuous-wave (CW) radars, since the TX and RX work simultaneously. In addition, in pulsed-radars, to omit the high insertion loss of the TRX switches, using two separated antennas is preferred. Therefore, it is highly desirable to reduce the number of antennas by sharing the TX and RX antennas. In particular, in the phased array systems with several channels of TRXs, reusing antennas leads to a significant size reduction and higher angular accuracy for electronically beam steerable systems. Additionally, sharing one antenna reduces the number of challenging high frequency interconnects between the chip and antenna, saving manufacturing costs. The main challenge of a single-antenna radar is the leakage signal of the TX at the input of the RX, which can significantly reduce the sensitivity of the RX. In order to have a good sensitivity for the RX, it is critical to have a high level of isolation between the TX and the RX.

The rest of this thesis is organized as follows. In Chapter 2, the system level principle of the radar systems is given. Chapter 3 studies the system level requirements for

the automotive radar and then makes a bridge between the system level requirements to the circuit level specifications. Chapter 4 introduces single-antenna architectures and challenges, and proposes a novel leakage cancellation solution. The circuit level designs and simulations of the building blocks are demonstrated in Chapter 5. The measurement results and conclusion of this project are reported in Chapter 6 and Chapter 7, respectively.

Chapter 2

Radar principle

This chapter briefly describes the basic information required for a circuit designer to be able to translate the radar parameters to the system and circuit level parameters [2].

The chapter starts with the radar equation and continues with the study of the relationship between the signal to noise ratio (SNR) and false alarm rate (FAR). Finally, the concept of pulsed and FMCW radars is illustrated.

2.1 Radar equation

As we know, radars can measure the distance of a target by sending electromagnetic waves and receiving the back-scattered signals. Radar equation shows how the received power is related to the transmitted signal. The simplest transmitting waveform is a burst of a single tone carrier, shown in Fig. 2-1.

Assuming the TX delivers an output power of P_{TX} to the antenna and the transmitted power propagates omnidirectionally, as shown in Fig. 2-2(a), the power density (P) per unit area in a distance R can be calculated by

$$P = \frac{P_{TX}}{4\pi R^2}. (2.1)$$

If a directive antenna with a gain of G_{TX} is utilized, as shown in Fig. 2-2(b), the power

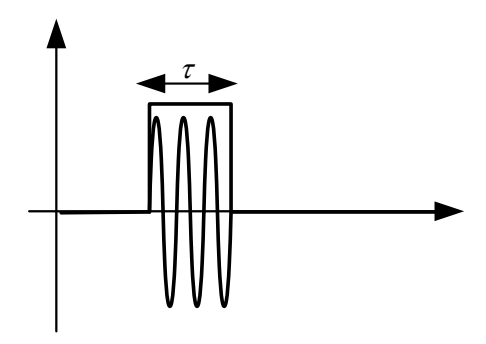


Fig. 2-1. A simple radar waveform.

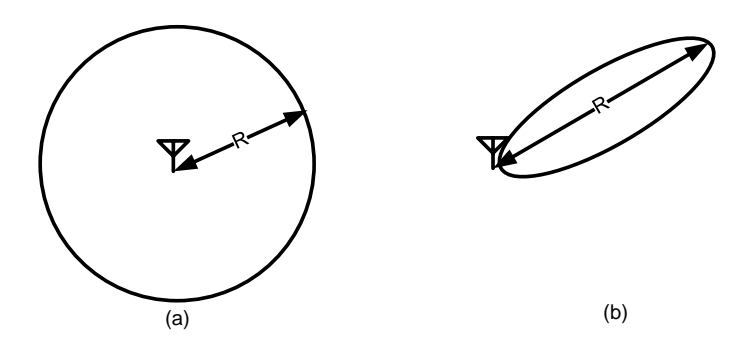


Fig. 2-2. (a) Omnidirectional, and (b) directive wave propagation.

density of the transmitted signal at distance R can be calculated using

$$P = \frac{G_{TX}P_{TX}}{4\pi R^2}. (2.2)$$

When the transmitted power hits a target with a radar cross section (RCS) area of σ square meters, then total incident power to the object is equal to

$$P_{\sigma} = \frac{G_{TX}P_{TX}\sigma}{4\pi R^2}.$$
 (2.3)

Assuming the target reflects the incident power omnidirectionally and assuming the effective area of the RX antenna is A_e , the received power at the input of the RX can be calculated by

$$P_{RX} = \frac{P_{\sigma}}{4\pi R^2} A_e. \tag{2.4}$$

The effective area of an antenna can be calculated as a function of the gain of the antenna gain (G_{RX}) and the wavelength (λ) using

$$A_e = \frac{G_{RX}\lambda^2}{4\pi}. (2.5)$$

Substituting (2.3),(2.5) into (2.4) and assuming $G_{TX} = G_{RX} = G$, the radar equation can be calculated by

$$P_{RX} = \frac{P_{TX}G^2\lambda^2\sigma}{(4\pi)^3 R^4}. (2.6)$$

From (2.6), the maximum detectable range of a radar can be calculated as follows:

$$R_{max}^{4} = \frac{P_{TX}G^{2}\lambda^{2}\sigma}{(4\pi)^{3}P_{min}},$$
(2.7)

where P_{min} is the sensitivity of the RX.

2.2 False alarm rate and probability of detection

In radar systems as well as other electrical systems, noise is the source of uncertainty for detecting the minimum signals. In communication systems, the noise power defines the bit error rate (BER) of a communication link. In the radar systems, also noise defines the probability of detection (PD) and false alarm rate (FAR). Obtaining a lower FAR as well as a higher PD is the goal of a radar designer. These requirements finally determine the acceptable signal to noise ratio (SNR) of the received signal. The noise factor (F) of an RX is defined as the ratio of the input SNR to the output SNR, as follows:

$$F = \frac{SNR_{in}}{SNR_{out}}. (2.8)$$

Substituting $SNR_{in} = P_{RX}/KTB$ in (2.8), the required received power (P_{RX}) as functions of the noise factor and SNR_{out} can be calculated by

$$P_{RX} = FKTBSNR_{out}, (2.9)$$

where K is Boltzman constant, T is temperature in Kelvin and B is the noise bandwidth of the RX.

The relation between required SNR and PD is illustrated in Fig. 2-3. Combining the information of Fig. 2-3 and (2.9), the minimum required received power in order to achieve an acceptable PD and FAR can be obtained. Substituting (2.9) into (2.7), the maximum range of a radar can be rewritten by

$$R_{max}^4 = \frac{P_{TX}G^2\lambda^2\sigma}{(4\pi)^3 FKTBSNR_{out}}.$$
 (2.10)

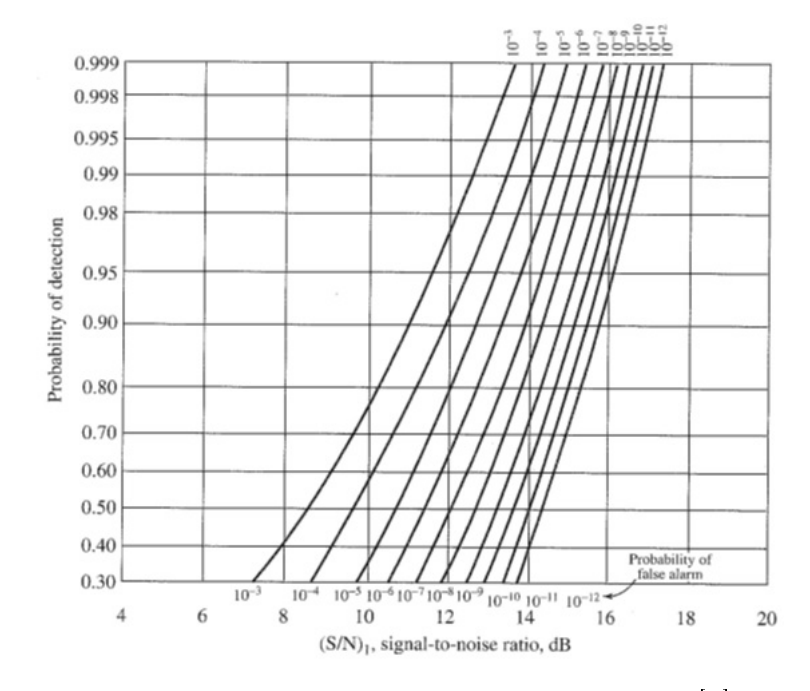


Fig. 2-3. PD versus SNR for different FARs [2].

2.3 Pulse integration

The above calculations are for single pulse processing detection. In practice, it is not necessary to make a decision just by receiving a mono pulse. In fact, radar systems use a train of pulses to detect the targets. Therefore the process of detection can be improved be employing averaging and pulse integration techniques. Assume y_i is the received noisy

voltage of the i-th pulse at the RX as follows:

$$y_1 = x(t) + n_1(t)$$

 $y_2 = x(t) + n_2(t)$
.
 $y_N = x(t) + n_N(t),$ (2.11)

where x(t) is the received pulse reflected from a target and $n_i(t)$ is the additive noise for the i-th pulse. By integrating the N received pulses we have

$$y = y_1 + y_2 + . + y_N = Nx(t) + n_1(t) + n_2(t) + ... + n_N(t).$$
 (2.12)

Therefore, the SNR after pulse integration can be calculated by

$$SNR = \frac{\left(\sum_{i=1}^{N} x(t)\right)^{2}}{\sum_{i=1}^{N} n_{i}^{2}} = NSNR_{sp},$$
 (2.13)

where SNR_{sp} represents the SNR of a single pulse. (2.13) indicates that the SNR will be improved proportionally by increasing the number of pulses. In practice, however, neither all the received pulses are fully correlated nor all the noise terms are fully uncorrelated. As a result, improvement of SNR is lower than the N factor. Accordingly, for accounting for these imperfections, another term should be added to the above equation called the integration improvement factor, defined by $I_N = N.E_N$, where N is the number of pulses and $E_N < 1$ is the integration efficiency. Adding the pulse integration effect to 2.10), the maximum range of the radar can be written as

$$R_{max}^{4} = \frac{P_{TX}G^{2}\lambda^{2}\sigma NE_{N}}{\left(4\pi\right)^{3}FKTBSNR_{out}}.$$
(2.14)

In order to handle the pulse-width of τ (as shown in Fig. 2-1), the RX needs to have a minimum bandwidth of $B \approx 1/\tau$. Therefore, the radar equation can be modified by

$$R_{max}^{4} = \frac{P_{TX}\tau G^{2}\lambda^{2}\sigma N E_{N}}{\left(4\pi\right)^{3} FKTSNR_{out}}.$$
(2.15)

In fact, the term $P_{TX}\tau N$ in the nominator of (2.15) is the total energy that the TX has been emitted (E_{TX}) . Therefore, the radar equation can be written as

$$R_{max}^{4} = \frac{E_{TX}G^{2}\lambda^{2}\sigma E_{N}}{\left(4\pi\right)^{3}FKTSNR_{out}}.$$
(2.16)

It can be inferred from (2.16) that the maximum detectable range of a radar is dependent on the total transmitted energy rather than transmitted power.

2.4 Range resolution

The minimum distance between two targets that a radar can distinct is the range resolution. In Fig. 2-4 a burst of transmitted signal with pulse width of τ is propagating toward two targets T_1 and T_2 at distances R_1 and R_2 . The time of flight for the front edge of the burst to hit to the target T_1 and T_2 and then go back to the RX can be calculated by the following equations:

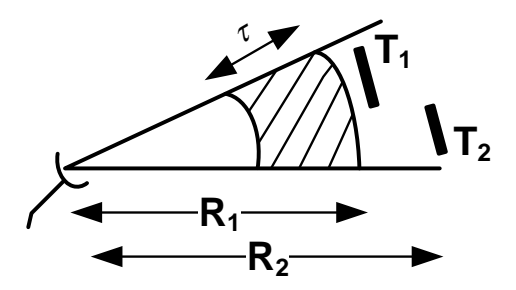


Fig. 2-4. Incident of a burst of electromagnetic wave to the targets.

$$t_{1}^{'} = \frac{2R_{1}}{C}$$

$$t_{2}^{'} = \frac{2R_{2}}{C},$$
(2.17)

where C is the speed of light in the air. The received output signal due to T_1 and T_1 is depicted in Fig. 2-5. In order to receive two separated pulses without any ambiguity $t_2' > t_1' + \tau$, $\frac{2R_2}{C} > \frac{2R_1}{C} + \tau$. As a result, the minimum distinguishable distance between two targets is

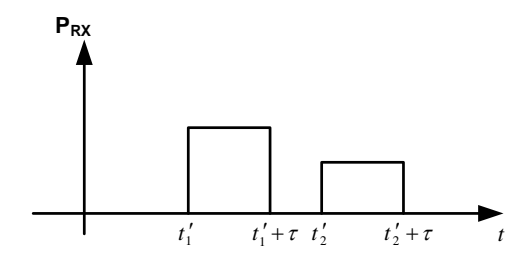


Fig. 2-5. Received signal from two targets.

$$d = R_2 - R_1 > \frac{\tau C}{2} = \frac{C}{2B}. (2.18)$$

It can be inferred from (2.18) that the range resolution depends on the pulse width or in general bandwidth of the transmitted signal. The higher the bandwidth, the finer the range resolution.

2.5 Range ambiguity and minimum detectable range

As mentioned in Section 2.3, pulsed radars typically utilize a train of pulses instead of a mono-pulse. The period and frequency of repetition of the pulses are called pulse repetition interval (PRI) and pulse repetition frequency (PRF), respectively, as shown in Fig. 2-6. To avoid any ambiguity in the distance measurement in a pulsed radar system, we should make sure that the RX is only receiving the pulses corresponding to the latest transmitted pulse. Otherwise, it is possible that the received pulse would be due to a reflection from a target corresponding to several pulses earlier. This can make range ambiguous since there is a misalignment between the received and transmitted pulses.

To resolve the range ambiguity problem, there should be enough time space between the transmitted pulses. This makes sure that all the reflections have enough time to be received by the RX. The time interval will be obtained regarding the maximum range of the radar (R_{max}) . It postulates that

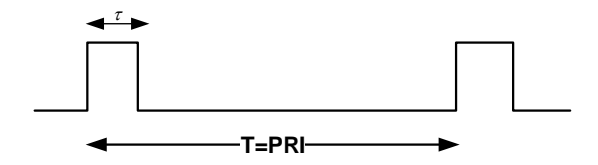


Fig. 2-6. Transmitted pulses with a specified pulse width and PRI.

$$R_{max} < \frac{C}{2}PRI$$

$$R_{max} < \frac{C}{2PRF}.$$
(2.19)

On the other hand, in pulsed radars, the RX is turned off when the TX is sending the pulses to avoid saturation of the RX. Therefore, during sending pulses, there is no information about back-scattered signals from the closer targets. As a result, there is another constraint on the distance measurement, known as the minimum range (R_{min}) for pulsed radars. It can be calculated by

$$R_{min} > \frac{\tau C}{2}. (2.20)$$

2.6 Doppler and velocity resolution

When the velocity of a target has a vector toward/against to the direction of a propagated wave, a frequency shift on the carrier of the signal appears called the Doppler frequency shift. Doppler effect can be calculated by $f_d = \frac{2V_r}{C} f_0$, where C is the speed of light in the air, V_r is the velocity component of the target aligned with the direction of the wave, and f_0 is the carrier frequency of the wave.

Assume the carrier frequency and pulse width of the transmitted signal is f_0 and τ ,

respectively and the backscattered signal has a frequency shift due to the Doppler effect, as shown in Fig. 2-7. In order to find the frequency shift at the receiver, The carrier of the received signal should be compared with a reference frequency. The correlation integral is what a baseband processor uses to find how close the received signal is to the reference signal. Assuming the reference frequency is f_0 (the frequency of the transmitted signal), the correlation integral is calculated as follows:

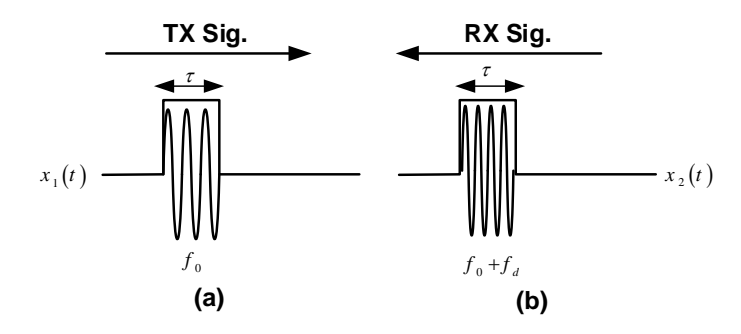


Fig. 2-7. (a) Transmitted signal, (b) Received signal with Doppler frequency shift.

$$Corr(f_d) = \frac{2}{\tau} \int_0^{\tau} x_1(t) x_2(t) dt = \frac{1}{\tau} \int_0^{\tau} \cos(2\pi f_0 t) \cos(2\pi (f_0 + f_d) t) dt.$$
 (2.21)

Simplifying the above equation results in

$$Corr(f_d) = \frac{\sin(2\pi f_d \tau)}{2\pi f_d \tau}.$$
 (2.22)

In fact, the above equation shows that when f_d deviates from 0, the correlation factor goes down from 1 to 0. However, this distinction does happen rapidly. In other words, the accuracy of the correlation is limited to the above Sinc function, as shown in Fig. 2-8. Considering the main-lobe of the Sinc function as the velocity measurement accuracy,

$$-\pi < 2\pi f_d \tau < \pi \Rightarrow -\frac{1}{2\tau} < f_d < \frac{1}{2\tau} \Rightarrow -\frac{C}{4\tau f_0} < V_r < \frac{C}{4\tau f_0}.$$
 (2.23)

The above equation indicates that the measurement accuracy of the velocity depends on the pulse width of the transmitted signal. The longer the pulse width, the narrower the Sinc function and hence a better distinction between the TX and RX carrier frequency.

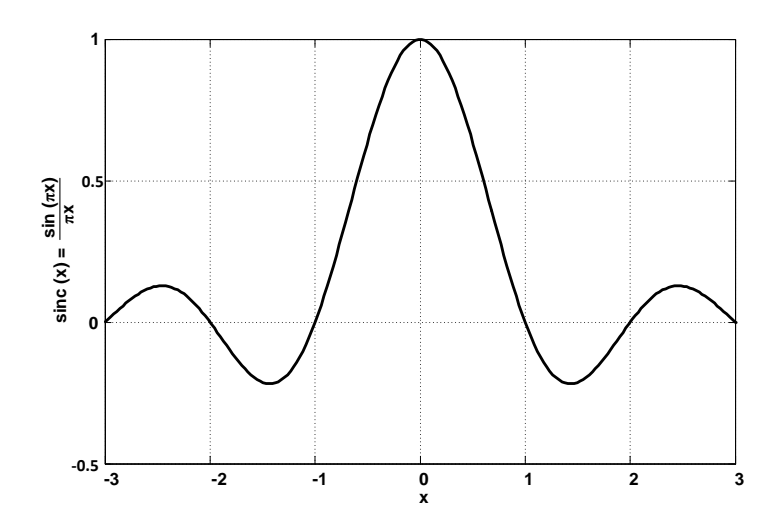


Fig. 2-8. Sinc function.

2.7 Continuous-wave radars

Up to this point, we have discussed the distance and Doppler measurement of pulsed radars. In this section, another type of radars, called continues wave (CW) radars, is introduced.

By increasing the pulse width of a pulsed radar to infinity, a simple CW radar will be produced, which is basically a carrier signal at the RF frequency. As a result of (2.23), an infinity large pulse width is useful for measuring Doppler with very fine accuracy. This, however, suffers from lack of range resolution since the bandwidths of a simple carrier signal is zero, as proven in (2.19).

How can a CW radar measure the distance?

Equation (2.18) indicates that the bandwidth of a radar signal sets the range resolution. Therefore, a modulated CW signal can be used to provide the required bandwidth for the signal and result in range measurement capability. FMCW radars are extensively adopted practically because of their unique features and simplicity.

2.7.1 FMCW radars

FMCW radars are a kind of CW radar, which utilize linear frequency modulation to increase the bandwidth of the transmitted signal and subsequently achieve the range

resolution. A typical signal that is used in FMCW radars is depicted in Fig. 2-9. The signal appears at the input of the RX after flying between the TX and RX with a delay of t_d . In order to extract the delay from the received signal, the frequency of the received signal only needs to be down-converted by the original TX signal. The down-converted baseband signal is called the beat frequency. In fact, the beat frequency is the frequency difference of the transmitted and received signals due to the time delay.

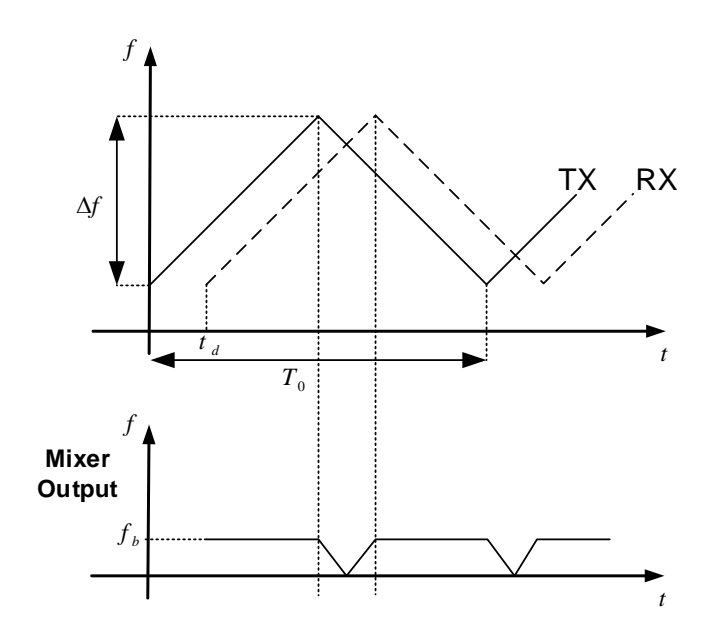


Fig. 2-9. Transmitted and received signals in an FMCW radar.

According to Fig. 2-9, the frequency ramp slope (α) can be defined by

$$\alpha \stackrel{\Delta}{=} \frac{\Delta f}{\frac{T_0}{2}} = \frac{2\Delta f}{T_0},\tag{2.24}$$

where Δf is the difference between the start and stop frequency of the transmitted signal (bandwidth) and T_0 is the period of the waveform. The beat frequency (f_b) can be calculated by

$$f_b = t_d \alpha = \frac{2R}{C} \frac{2\Delta f}{T_0} = \frac{4R\Delta f}{CT_0}.$$
 (2.25)

2.7.2 Doppler frequency shift in FMCW radars

The frequency shift resulting from the Doppler effect directly increases/decreases the carrier frequency of the received signal, as shown in Fig. 2-10. As a result, the beat frequency for the rising and falling ramps is not the same due to the Doppler frequency shift. The beat frequency is $f_{b1} = f_{b0} - f_d$ and $f_{b2} = f_{b0} + f_d$ for the rising and falling ramp, respectively, where f_{b0} is the beat frequency due to distance (without Doppler effect) and f_d is the Doppler frequency shift. By solving these two equations, f_{b0} and f_d can be calculated as follows:

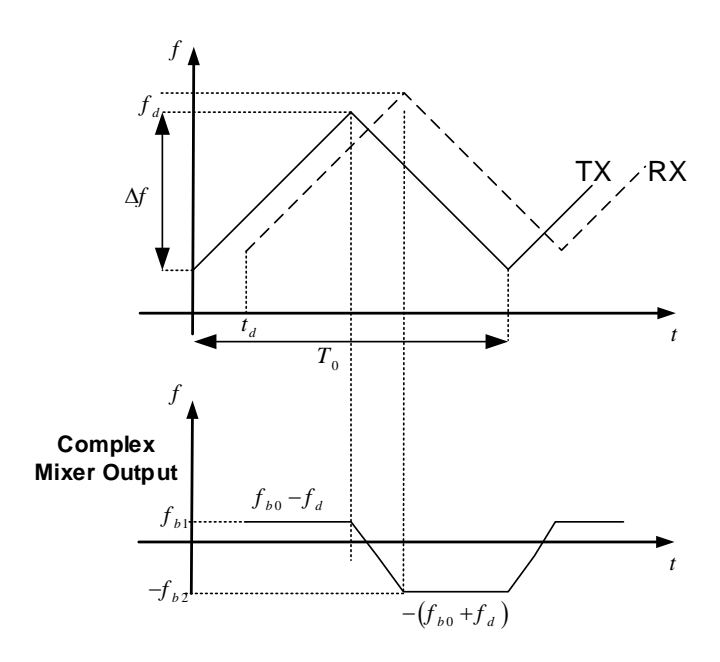


Fig. 2-10. Transmitted and received signals in the presence of the Doppler effect in FMCW radars.

$$\begin{cases} f_{b1} = f_{b0} - f_d \\ f_{b2} = f_{b0} + f_d \end{cases} \Rightarrow \begin{cases} f_{b0} = \frac{f_{b1} + f_{b2}}{2} \\ f_d = \frac{f_{b2} - f_{b1}}{2} \end{cases}$$
 (2.26)

2.7.3 Range and velocity resolution in FMCW radars

From previous discussions, we know that either range or Doppler information produces an IF signal called the beat frequency at the output of the down-converter mixer. Therefore, the resolution of distance or velocity measurement corresponds to the resolution of the

beat frequency measurement at the baseband circuit. Digitizing baseband signals and using a fast Fourier transform (FFT) processor is a way to process FMCW raw data. Substituting the FFT bandwidth of $2/T_0$ (i.e., the frequency difference between two bins of the FFT) for a ramp duration of $T_0/2$ into $\Delta f_b = \frac{4\Delta f}{CT_0}\Delta R$ (obtained from (2.25)), where ΔR is the distance between two resolvable targets, the range resolution of the FMCW radar can be calculated by

$$\Delta R = \frac{C}{2\Delta f}.\tag{2.27}$$

The above equation is in agreement with (2.18) showing the range resolution for pulsed radars.

The velocity resolution can be calculated as a function of the Doppler frequency by $\Delta V_r = \frac{C}{2f_0} \Delta f_d$. Again, the accuracy of the frequency measurement is limited to the bandwidth of the FFT's bin, as discussed earlier. Substituting $\Delta f_d = \frac{2}{T_0}$, the velocity resolution can be obtained as

$$\Delta V_r = \frac{C}{f_0 T_0}. (2.28)$$

2.8 Conclusion

In this chapter, we introduced the basic principle of radar equations. First, we started with the simple principle of pulsed radar and then we extended it to the concept of CW and FMCW radars. The most important results from this chapter are concluded as follows.

- 1. According to the radar equation, the maximum range of a radar depends on the transmitted energy rather than transmitted power. Since CW radars can generate higher energy compared to pulsed radars, they are more attractive in cases of technologies with low peak power output.
- 2. The range resolution of a radar depends on the bandwidth of the transmitted signal regardless of the radar type.
- 3. The velocity resolution depends on the pulse width. Since CW radars inherently

have a longer period, they have a better range resolution performance compared to the pulsed radars.

Chapter 3

System and RF specifications for the automotive radar

In this chapter, we will characterize the TX and RX specs for the automotive radar application.

22 GHz and 77 GHz are two frequency bands allocated for the automotive radar. The 22 GHz band is an ISM band with a highly-restricted power emission. Therefore, the regulations do not permit the TX to generate the high output level required for long-range applications. However, there is more than 4 GHz bandwidth available at the 22 GHz ISM band, which results in a good range resolution performance for the short-range systems. Recently, 77-78 GHz has been assigned for long-range radars, which allows a maximum equivalent isotropically radiated power (EIRP) of 55 dBm, and the 78-84 GHz band is alternative to 22 GHz, which has sufficient bandwidth while permits a higher emission power relative to the 22 GHz band. The 77 GHz band has been adopted since it has a lower attenuation factor in air, as shown in Fig. 1-2. The three times higher frequency of the 77 GHz band compared to the 22 GHz band makes it possible to shrink the size of the antennas to three times smaller.

An automotive radar is traditionally divided into three categories, as follows:

1. Long Range Radar (LRR); utilizes a narrow beam pattern antenna which can see up to 200 meters away and can keep the speed of the hostile car relative to the front vehicle such that it avoids the hostile car colliding with the front vehicle. Therefore, it is used as an automatic cruise control (ACC) system.

- 2. Medium Range Radar (MRR); has a wider beam pattern and lower range (usually less than 100 meters). It might be installed around the car, which monitors the hostile car in the lane change condition.
- 3. Short Range Radar (SRR); is utilized in the parking assistance system as a virtual bumper with a better range resolution performance at shorter range (less than 30 meters).

The system design starts with a specification provided in Table 3.1 from [33]. Initially, the type of radar (i.e., pulsed radar or CW radar) is selected. Then, based on the radar equations studied in Chapter 2, the TX output power and the dynamic range requirements for the RX are extracted. The noise effect is studied and a phase noise (PN) analysis for the automotive radar including the PN correlation effect is performed for an extreme case to find the PN requirement of the system.

Table 3.1: Automotive radar classification and specification

Type	LRR	MRR	SRR
Maximum transmit power (EIRP)	55 dBm	$-9~\mathrm{dBm/MHz}$	$-9~\mathrm{dBm/MHz}$
Frequency band	76-77 GHz	77-81 GHz	77-81 GHz
Bandwidth	600 MHz	600 MHz	4 GHz
Distance range $R_{min}R_{max}$	10-250 m	1-100 m	0.15-30 m
Distance resolution ΔR	0.5 m	0.5 m	0.1 m
Velocity resolution ΔV	$0.6~\mathrm{m/s}$	$0.6~\mathrm{m/s}$	$0.6~\mathrm{m/s}$
3 dB beamwidth in azimuth $\pm \phi_{max}$	±15°	±40°	±80°
3 dB beamwidth in elevation $\pm \theta_{max}$	±5°	±5°	±10°

3.1 Choosing the radar type

To make sense of the differences between mono-pulse radars, pulsed radars, and FMCW radars, in terms of required output peak power, measurement time, and bandwidth, it is instructive to have a design example and then compare the results. Assume we want to design a radar that is able to detect a target with a radar cross section of $\sigma = 1 \text{ m}^2$ at a distance of 200 m with an SNR of better than 10 dB. For simplicity, assume the NF of the RX is 0 dB (any NF increment should be directly added to the TX output power to compensate for the SNR degradation). How much power should the TX generate? In order to use the radar equation, the gain of the antenna should be calculated. The gain of the antenna can be roughly calculated based on spatial radiation as follows [1]:

$$G \approx \frac{32400}{\theta_{azm}\theta_{elv}},\tag{3.1}$$

where θ_{azm} and θ_{elv} is the 3 dB beamwidth of the antenna beam for azimuth and elevation, respectively. Using the LRR specs in Table 3.1, the gain of the antenna approximately is $G = 10 \log \left(\frac{32400}{30 \times 10}\right) = 20.33$ dBi. The bandwidth required for 0.5 m range resolution is B = 300 MHz. Using the radar equation (2.14), the required TX output power for a mono-pulse radar is 53.7 dBm or 231 W at 80 GHz, which is not feasible even in compound semiconductors such as GaN at the mm-wave band.

Pulse integration can be adopted in order to improve the SNR while the TX output peak power is limited to only 10 dBm. This power level is feasible on CMOS technology. Without loss of generality, assume the RX NF is 0 dB and the pulse integration efficiency is 100%. Therefore, the number of pulses for obtaining sufficient SNR is more than 23,000. The maximum PRF for unambiguous range measurement is 750 kHz. Therefore, the measurement time for sending 23,000 pulses is 30 ms.

For an FMCW radar, the required bandwidth is similarly 300 MHz and there is no need to pulse integration. The main difference between FMCW radars and pulsed radars is the noise bandwidth. For pulsed radars, the noise bandwidth equals RF bandwidth. However, the actual noise bandwidth of an FMCW radar is defined by the FFT bin's

bandwidth, which equals $\frac{2}{T_0}$, where T_0 is the period of the sweeping ramp, as shown in Fig. 2-9. With the assumption of 10 dBm peak power, the noise bandwidth of less than 13 kHz is required, which is corresponds to $T_0 > 153$ us. This shows that the FMCW radar can do the measurement 210 times faster than the pulsed radar with the same output power.

To achieve a velocity resolution of 0.6 m/s, in Table 3.1, the pulse width should be greater than 3.246 ms and 6.492 ms for the pulsed radar and FMCW radar, respectively. On the one hand, the required pulse width should be $\tau = \frac{1}{B} = 3.33$ ns for the pulsed radar. On the other hand, it should be greater than 3.246 ms, which is contradictory. This conflict can be tackled by using a coherent process on the train of $\frac{3.246 \text{ ms}}{3.33 \text{ ns}} = 974775$ pulses, resulting in a total measurement time of 1.299 s. Again, the FMCW radar is much faster than the pulsed radar in terms of measuring Doppler.

Another comparison between pulsed radars and FMCW radars is the sampling rate requirement of the baseband circuits and ADCs. The sampling rate of an ADC is determined by the bandwidth of the baseband signal. Considering the Nyquist criterion, it should be more than twice the maximum frequency content of the baseband signal. Since the bandwidth of baseband signals in the pulsed radar system is exactly the same as the RF bandwidth, it needs a high sampling rate ADC to capture narrow pulse widths. For the above example, the required sampling rate should be more than 600 MSample/s for capturing the pulse width of 3 ns without aliasing. If a range resolution of 0.1 m is required (i.e., for short range applications), the sampling rate has to be more than 3.75 GSample/s. Therefore the complexity, power, and cost of the baseband processing are very high for pulsed radars. However, using (2.25) the bandwidth of the baseband can be calculated based on the maximum distance for FMCW radars, as follows:

$$f_{bmax} = \frac{4\Delta f}{CT_0} R_{max} = \frac{4 \times 300 \times 10^6}{3 \times 10^8 \times 6.429 \times 10^{-3}} \times 200 = 124.43 \text{ kHz}.$$
 (3.2)

Therefore, the sampling rate of the ADC for the FMCW radar needs to be only greater than 250 kSample/s, which feasibly can be implemented in the CMOS technology with reasonable power consumption and dynamic range.

So far, the comparison identifies the superiority of the FMCW. The main weakness of FMCW radars is the requirement of a high level of isolation between the TX and RX. In the CW radars, since the TX and RX work simultaneously, a high level of isolation is required to prevent the RX from saturation that is caused by TX leakages. Using two separated antennas is the basic solution to address this issue at the cost of doubling the antenna areas. In this thesis, we address this problem and break the limitation by means of a new architecture, which is capable of canceling leakages from the TX to RX. Table 3.2 summarizes the above discussions.

Table 3.2: Radar types comparison.

Type	Mono-pulse	Pulsed radar	FMCW radar
Maximum range	200 m		
Antenna gain	20.33 dBi		
Range resolution	0.5 m		
Velocity resolution	$0.6~\mathrm{m/s}$		
${f Bandwidth}$	300 MHz		
Sampling rate of ADC	$600~\mathrm{MSample/s}$		$250~\mathrm{kSample/s}$
Peak output power	53.37 dBm (231 W)	10 dBm	
Time of range measurement	3.33 ns	30 ms	153 us
Time of velocity measurement	NA	1.299 s	$6.429~\mathrm{ms}$

3.2 Dynamic range in radars

There is a big gap between the dynamic range required in a wireless communication system and in a radar system. Typically in wireless communication systems, the transmitted wave travels from a TX antenna to another RX. Therefore, the transmitted signal just experiences one-way free space propagation loss, which is inversely proportional to R^2 . In addition, when a connection is established, the signal level variation is controlled over time by means of variable gain amplifiers (VGAs) to make the signal level appropriate for applying to the ADC block. For radar systems, however, the propagation loss of the signal

is inversely proportional to R^4 since the transmitted signal travels from the TX antenna to a target and back-scatters from the target to the RX. Moreover, it is not applicable to use a simple VGA for gain control because a lot of reflecting signals are received from various objects at different distances that the radar should capture at the same time. For example, if the RX gain is adjusted for monitoring a target at a longer distance, powerful back-scattered signals from closer objects can easily saturate the RX in a radar system. Consequently, the dynamic range issue in radar systems is stricter than in communication systems.

Assuming an RX with 0 dB NF, a minimum required SNR of 16 dB for detecting with a good PD and low FAR, radar cross section of $\sigma=1$ m² for the target, and an FFT bandwidth of $B=\frac{2}{T_0}=\frac{2}{6.429~ms}=311.1$ Hz, the minimum output power of the TX can be calculated by

$$P_{TX} = \frac{(4\pi)^3 KTBFSNR_{out}R_{max}^4}{G^2\lambda^2\sigma}.$$
 (3.3)

Using (3.3), from the different radar types in Table 3.1, the minimum TX power for LRR, MRR and SRR is 3.61 dBm, -3.86 dBm and -12.73 dBm, respectively.

The minimum received power versus distance of the target can be calculated using the radar equation (2.6). However, for the maximum received power, it is assumed that a flat object fully covers the beam of the antenna and reflects the incident waves to the RX similar to a flat mirror as shown in Fig. 3-1. As a result, using the geometrical optics, an image will be produced, which is located at twice the distance between the radar and the target. A distance of d between the object and TX is equivalent to a one way transmit and receive within 2d, as shown in Fig. 3-1. As a result of a single path transmission, the propagation loss is inversely proportional to R^2 . The radar equation, in this case, can be modified to

$$P_{RX} = \frac{P_{TX}G^2\lambda^2}{(4\pi)^2R^2}. (3.4)$$

According to the specifications in Table 3.1, the minimum and the maximum, received power for the LRR, MRR, and SRR are plotted in Fig. 3-2 to Fig. 3-4 and the dynamic range requirements are tabulated in Table 3.3.

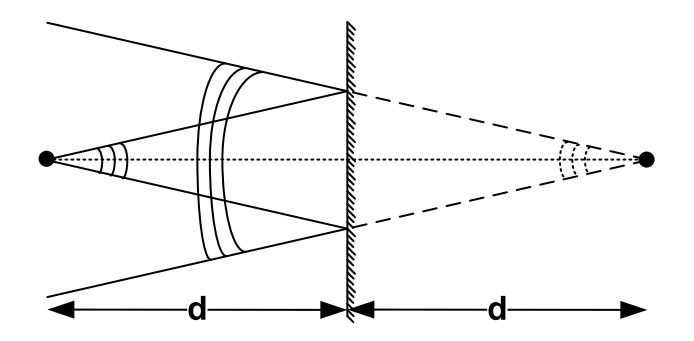


Fig. 3-1. Reflection of a target, covered the whole antenna beam, such as a flat mirror.

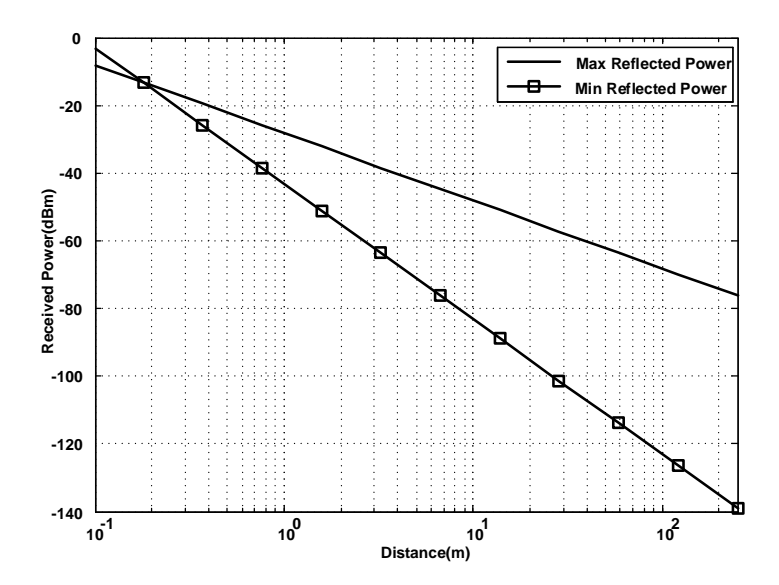


Fig. 3-2. Minimum and maximum received power versus target distance for LRR.

Table 3.3: Dynamic range requirement for LRR, MRR and SRR.

Туре	LRR	MRR	SRR
Distance range	10-250 m	1-100 m	0.15-30 m
Antenna gain	20.33 dBi	16.07 dBi	10.05 dBi
Minimum output power	3.61 dBm	-3.86 dBm	-12.73 dBm
Minimum received power	-139.1 dBm		
Maximum received power	-48 dBm	-44 dBm	-48.5 dBm
Dynamic range	91.1 dB	95.1 dB	90.6 dB

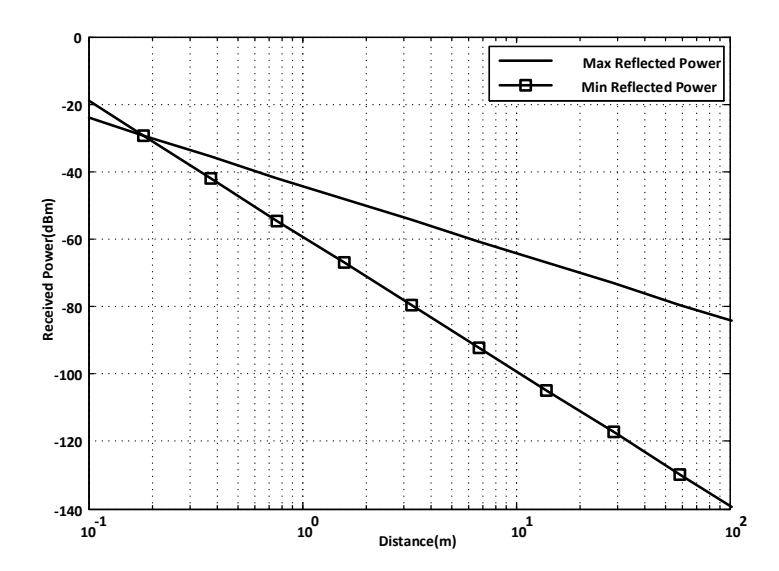


Fig. 3-3. Minimum and maximum received power versus target distance for MRR.

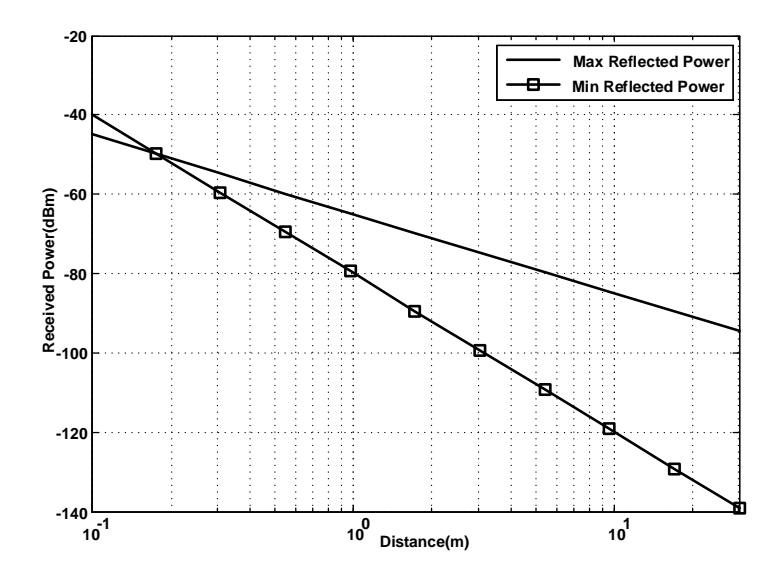


Fig. 3-4. Minimum and maximum received power versus target distance for SRR.

3.3 Noise in FMCW radars

An FMCW radar TRX, consisting of a frequency ramp generator followed by a power amplifier as the TX, and an low noise amplifier (LNA), down-converter mixer, and baseband filter followed by an ADC, as the RX, is shown in Fig. 3-5. The noise sources of the circuits are as follows.

- 1. Thermal noise of the RX (i.e., NF of the RX).
- 2. Flicker noise of the baseband circuits.

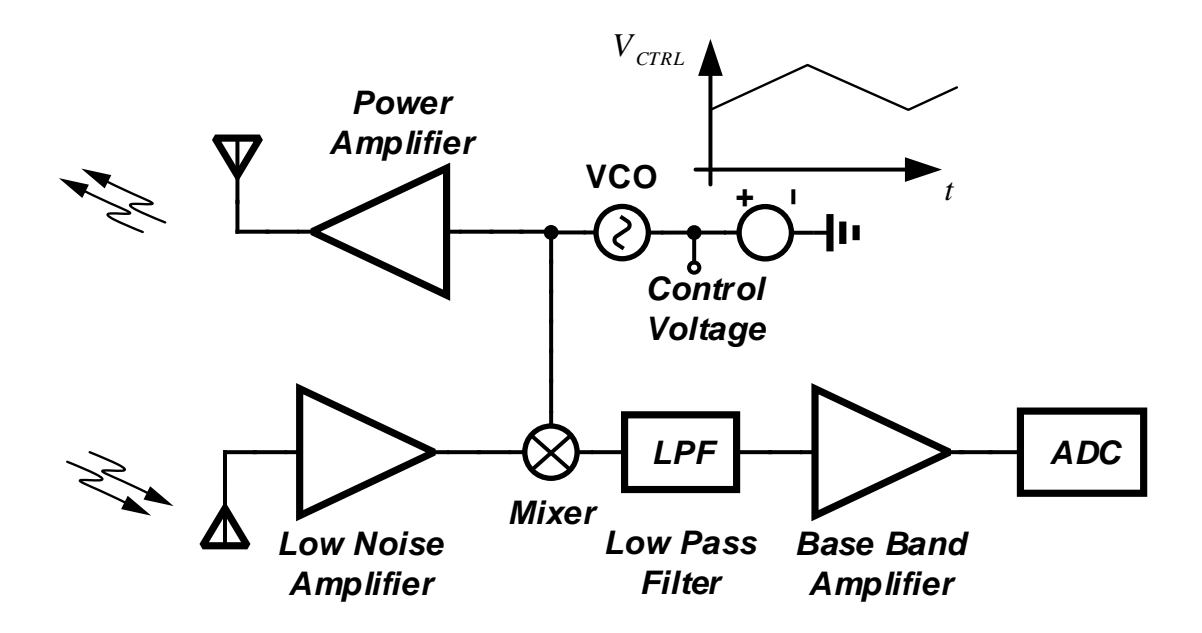


Fig. 3-5. Block diagram of an FMCW radar transceiver.

- 3. Thermal noise of the TX.
- 4. PN of the frequency ramp generator.

In this section, the effect of each noise is studied.

3.3.1 Thermal noise of the RX

Like any communication system, the SNR of the received signal is degraded due to the thermal noise of the RX in a radar. The higher the NF, the lower the SNR. Therefore, a TX with higher output power is required to compensate for the lack of SNR. Increasing the TX output power is challenging in terms of power consumption, die area, and complexity of the TX. Using an LNA helps to reduce the noise contribution of the RX building blocks with fewer overheads.

3.3.2 Flicker noise

Flicker noise is a concern of the direct conversation architecture, specifically in CMOS technology, because of its higher flicker noise corner frequency. For omitting this issue,

there should be enough gain before the baseband circuits, while the baseband circuits should be designed for low flicker noise. In this regard, the flicker noise issue increases the desire for a high gain LNA. As the radar equation predicts, the received power from an object increases with the slope of 40 dB/Dec when the target moves from a far distance toward the radar. In addition, for FMCW radars, the beat frequency starts moving from a higher baseband frequency to a lower frequency. Considering the flicker noise power increment of 10 dB/Dec, it is obvious that the power level of the received signal is increasing 30 dB/Dec more than the power level of the flicker noise. Therefore, as long as the RX has enough SNR for the maximum range, it can strictly receive the closer signals with enhanced SNR even in the presence of the flicker noise. The above description can be formulated as follows:

$$\begin{cases} P_{RX} & \propto \frac{1}{f_b^4} \\ P_{1/f} & \propto \frac{1}{f_b} \end{cases} \Rightarrow SNR = \frac{P_{RX}}{P_{1/f}} \propto f_b^3, \tag{3.5}$$

where P_{RX} is the received power, $P_{1/f}$ is the noise power of the flicker noise and f_b is the beat frequency of the captured target. The above equation indicates the SNR is improved 30 dB/Dec while targets move from a farther distance toward the radar.

3.3.3 Thermal noise of the TX

A ramp generator followed by a power amplifier (PA) generates required output power for an FMCW radar, as shown in Fig. 3-6. Assuming a power gain and noise figure of 20 dB and 4 dB, respectively, for the PA, the output noise power spectral density of the TX equals $P_{N,out} = KTFG = -150 \text{ dBm/Hz}$. This noise can be leaked to the RX antenna because of the limited isolation between the RX and TX circuits. Assuming an isolation level of 20 dB between the TX and RX, the total noise spectral density at the RX equals $P_{N,Ant} = KT + \frac{KTFG}{iso} = -168.5 \text{ dBm/Hz}$, which is equivalent to a 5.5 dB NF for the RX. Therefore, in addition to the danger of saturation for the receiver due to the leakage, the output noise of the TX establishes an important constraint on the required isolation level.

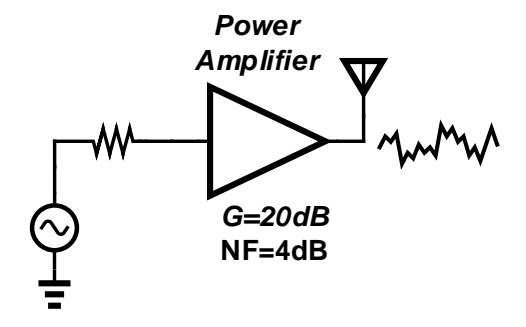


Fig. 3-6. Noise in the TX.

3.3.4 PN of the oscillator

One of the important noise sources in the radar system is the local oscillator PN. In this subsection, the investigation of the PN effect on the FMCW radar systems is studied. For this purpose, a worst-case scenario showing the effect of PN on the performance of the RX will be studied.

Assume a motorbike (small target) and a truck (big object) that covers the whole beam are located in front of the hostile car, as shown in Fig. 3-7. The small object is located close to the hostile car while the big object is farther away. The output spectrum of the received signal in an FMCW radar in the absence and presence of the PN is depicted in Fig. 3-8(a) and (b), respectively. Due to the PN skirt of the stronger signal, the weak signal of the small target will dim, making it difficult to detect the small target. Although the above representation is insightful, it is not accurate enough. To be more precise, the PN range correlation effect [34] should be considered. For further investigation, assume the local oscillator signal (V_{IO}) , TX signal (V_{TX}) and received signal (V_{RX}) are in an FMCW radar as follows:

$$V_{LO} = A_{LO} \cos\left(\frac{1}{2}\alpha t^2 + \omega_0 t + \phi_N(t)\right),$$

$$V_{TX} = A_{TX} \cos\left(\frac{1}{2}\alpha t^2 + \omega_0 t + \phi_N(t)\right),$$

$$V_{RX} = A_{RX} \cos\left(\frac{1}{2}\alpha (t - \tau)^2 + \omega_0 (t - \tau) + \phi_N(t - \tau)\right),$$
(3.6)

where A_x represents the amplitude of the signal x, α is the slope of the frequency ramp, ω_0 is the starting frequency of the ramp, $\phi_N(t)$ is the phase noise of the signal and τ is the

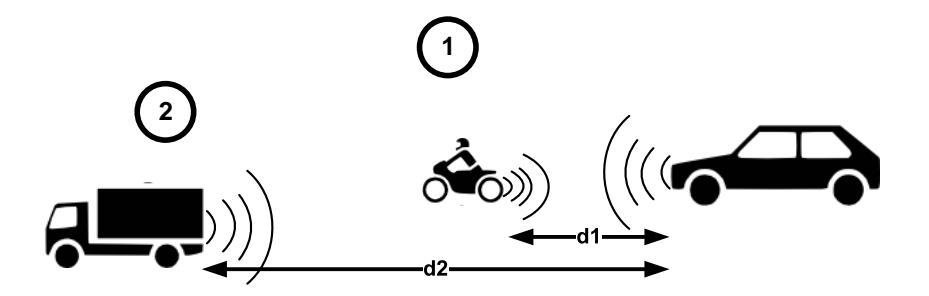


Fig. 3-7. A worst-case scenario for studying the PN effect.

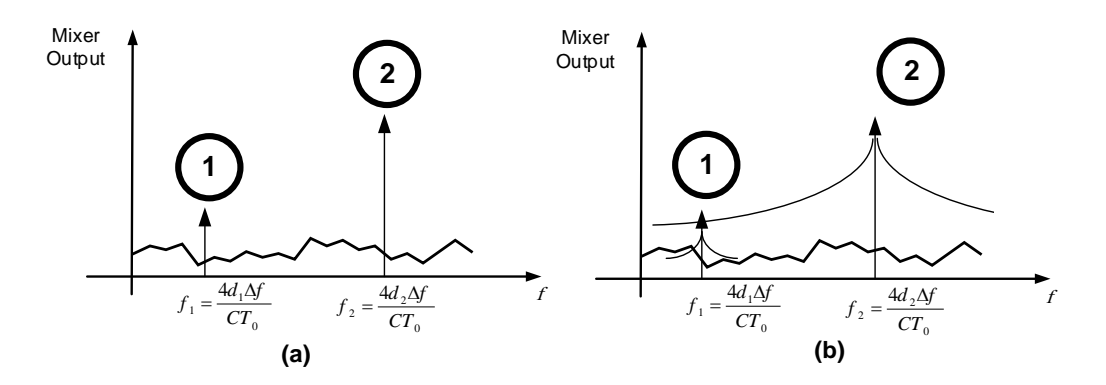


Fig. 3-8. Output spectrum of the baseband signal in the (a) absence, and (b) presence of the PN.

delay between the transmitted signal and received signal due to the time of flight. After down-conversion and filtering in the RX, the baseband signal (V_{BB}) can be calculated by

$$V_{BB} = V_{RX} \times V_{LO} = \frac{1}{2} A_{RX} A_{LO} \cos \left(\alpha \tau t + \omega_0 \tau + \frac{1}{2} \alpha \tau^2 + \phi_N(t - \tau) - \phi_N(t) \right). \tag{3.7}$$

Taking the Fourier transform of the PN signal $\phi_{N,BB}(t) = \phi_N(t-\tau) - \phi_N(t)$ at the baseband, the frequency spectrum will be obtained as follows:

$$\Phi_{N,BB}(j\omega) = F\{\phi_N(t-\tau) - \phi_N(t)\} = (1 - e^{j\omega\tau}) \Phi_N(j\omega), \tag{3.8}$$

where $\Phi_N(j\omega)$ is the PN spectrum of the TX and ω is the frequency offset of the PN from the baseband carrier signal $\alpha\tau$. Simplifying (3.8), the baseband PN amplitude can be calculated by

$$|\Phi_{N,BB}(j\omega)| = 2 \left| \sin \left(\frac{\omega \tau}{2} \right) \right| |\Phi_N(j\omega)|.$$
 (3.9)

The PN amplitude tends to zero when the delay or the frequency offset goes to zero. This cancellation significantly relaxes the PN of the leakage signals inside the chip. For example, if the leakage signal flies a 1.5 mm distance from the TX to the RX inside a chip, considering a wave propagation speed of half of the speed of light in the free space, the delay of the leakage signal is about 10 ps. Using (3.9), the PN attenuation of 84 dB is achievable at the frequency offset of 1 MHz. This cancellation typically is enough to ignore the effect of the PN for the internal leakage signals. In the case of the introduced scenario, the PN power of target#2 at the frequency offset, which falls on target#1, should be calculated:

$$|\Phi_{N,BB}(j\omega)|_{\omega=2\pi(f_2-f_1)}^2 = 4\sin^2\left(\frac{\omega\tau_2}{2}\right)|\Phi_N(j\omega)|_{\omega=2\pi(f_2-f_1)}^2,$$
 (3.10)

where τ_2 is the time of flight of the signal for target#2, and f_i is the beat frequency of the i_{th} target in Fig. 3-7. Substituting $\tau_2 = \frac{2d_2}{C}$, $f_2 = \frac{4d_2\Delta f}{CT_0}$ and $f_1 = \frac{4d_1\Delta f}{CT_0}$ into (3.10), we have

$$|\Phi_{N,BB}(j\omega)|_{\omega=2\pi(f_2-f_1)}^2 = 4\sin^2\left(\pi\frac{4(d_2-d_1)\Delta f}{CT_0}\frac{2d_2}{C}\right)|\Phi_N(j\omega)|_{\omega=2\pi(f_2-f_1)}^2.$$
(3.11)

Multipling (3.11) by the received power due to the truck at d_2 ($P_{RX}|_{Truck} = \frac{P_{TX}G^2\lambda^2}{(4\pi)^2(2d_2)^2}$), the PN power spectral density ($P_{\Phi_{N,BB}}$) is calculated by

$$P_{\Phi_{N,BB}}|_{@f_1} = \frac{4P_{TX}G^2\lambda^2}{(4\pi)^2(2d_2)^2}\sin^2\left(\pi\frac{4(d_2-d_1)\Delta f}{CT_0}\frac{2d_2}{C}\right)|\Phi_N(j\omega)|_{\omega=2\pi(f_2-f_1)}^2.$$
(3.12)

In order to maintain the SNR, the ratio of the received power from the small target (target#1) to the power of the baseband PN over the FFT bandwidth (i.e. $B = \frac{2}{T_0}$) should be larger than the specified SNR. This follows that

$$\frac{P_{TX}G^2\lambda^2\sigma}{(4\pi)^3d_1^4SNR_{out}} > \frac{8P_{TX}G^2\lambda^2}{(4\pi)^2(2d_2)^2T_0}\sin^2\left(\pi\frac{4(d_2-d_1)\Delta f}{CT_0}\frac{2d_2}{C}\right)|\Phi_N(j\omega)|_{\omega=2\pi(f_2-f_1)}^2. \quad (3.13)$$

Rearranging the above equation yields:

$$|\Phi_N(j\omega)|^2_{\omega=2\pi(f_2-f_1)} < \frac{\sigma T_0 d_2^2}{(8\pi)SNR_{\alpha t} d_1^4} \frac{1}{\sin^2\left(\pi \frac{4(d_2-d_1)\Delta f}{CT_0} \frac{2d_2}{C}\right)}.$$
 (3.14)

Though (3.14) is a function of d_1 and d_2 , the toughest PN requirement will be obtained when the big target (target#2) is located at the maximum range of the radar (i.e., $d_2 = R_{max}$), as follows:

$$|\Phi_N(j\omega)|^2_{\omega=2\pi(f_{bmax}-f_1)} < \frac{\sigma T_0 R_{max}^2}{(8\pi)SNR_{\alpha t} d_1^4} \frac{1}{\sin^2\left(\pi \frac{4(R_{max}-d_1)\Delta f}{CT_0} \frac{2R_{max}}{C}\right)}.$$
 (3.15)

The PN specification including the range correlation effect for the LRR, MRR, and SRR are plotted in Fig. 3-9 for the worst case scenario.

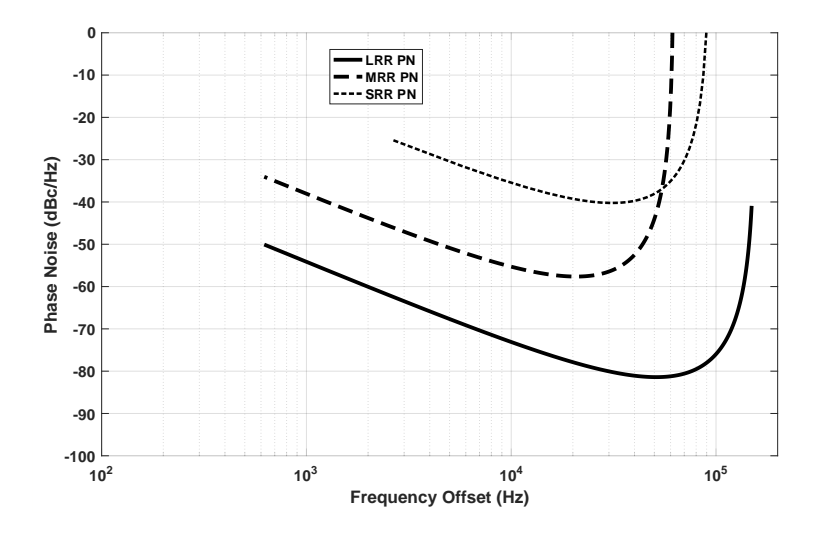


Fig. 3-9. PN requirement for LRR, MRR and SRR in the worst-case scenario.

3.4 Conclusion

In this chapter, we gained insight into the RF specs of the TRX that is required for the different classes of automotive radars. The most important points inferred from this chapter are as follows.

1. With the limitation of the TX output peak power in the CMOS technology, CW radars are the best choice since they can generate the total energy at a faster rate

- than the pulsed radars.
- 2. The measurement time for an FMCW radar is much smaller than that of a pulsed radar with the same output peak power.
- 3. The operation frequency of the baseband circuits and the sampling rate of the ADC for FMCW radars are relaxed regardless of the bandwidth of the signal. This, however, can be high for pulsed radars, causing more complicated and power hungry baseband circuits.
- 4. The required dynamic range for the RX is more than 90 dB in automotive applications, which is considerably higher than that of conventional wireless systems.
- 5. It is critical to have high isolation between the TX and RX in order to avoid the TX noise leakage and the saturation of the RX in CW radars.
- 6. The induced PN of the internal leakage signals inside the chip is significantly reduced thanks to the PN correlation effect. It implies that the best performance can be achieved if the LO signal of the down-converter mixer is directly extracted from the TX output without active buffers.

Chapter 4

Single-antenna architecture

In this chapter, the architecture of single-antenna radars is studied from a system level perspective. The motivations behind the use of a single-antenna is introduced. Then, the system level issues of implementing a single-antenna front-end at the mm-wave band are described, and the TX leakage as the main issue of these systems is demonstrated. In the next subsections, the solutions to the TX leakage by adopting leakage cancellation techniques will be covered.

4.1 Motivations

While FMCW radars are considered to be a low power architecture, suitable for implantation on CMOS technology, the EIRP of the TX needs to be increased for high range radars. Spatial power combining in the phased-array TRXs is a well-accepted solution to increase the range, while enabling electronic beam steering [35–38]. The conventional FMCW radar TRXs require two highly isolated antennas in order to reduce any leakages from the TXs to the RXs, as shown in Fig. 4-1(a). While the higher number of TX and RX channels provides a higher range and better angular resolution, the practical complexities of a large phased-array system usually limit the number of channels in conventional systems. The limitations typically lead phased-array systems to be designed with a lower number of TX channels, wider TX beam widths and higher output power (to obtain the required EIRP), to push the design complexity to the RX arrays with a higher number

of channels [39–41]. The big form-factor, interference the other radar systems, a complex and separate beamforming algorithm for both the TXs array and RXs array, and lower angular resolution are the drawbacks of the conventional phased-array radars with separated antennas. On the other hand, a single-antenna phased-array architecture, shown in Fig. 4-1(b), reduces the form-factor by half while releasing the imbalance of the TX and RX channels, which requires a single beamforming processor for both the TX and RX arrays. Moreover, due to the reciprocity of the single-antenna passive, a perfect beam alignment is achievable.

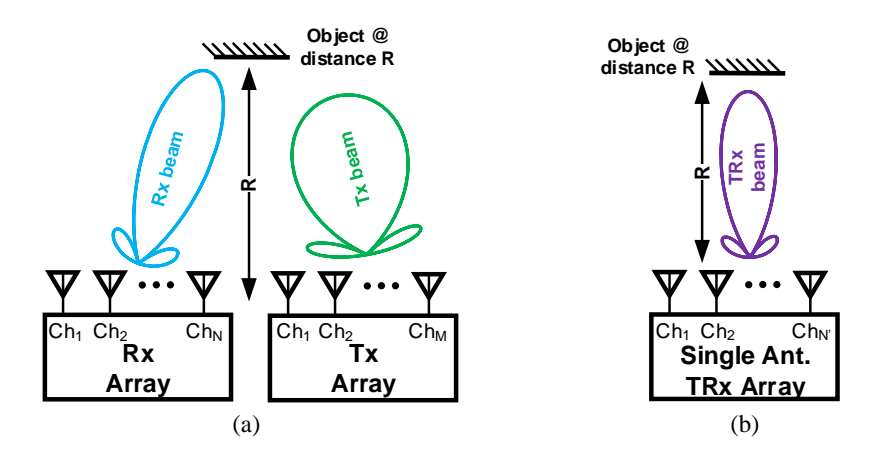


Fig. 4-1. (a) A conventional phased-array radar TRX. (b) A single-antenna-based phased-array radar TRX.

To show the performance improvement of the single-antenna architecture with size of N' compared to the conventional phased-arrays with N RXs and M TXs, we define a range improvement factor (RI). Expanding the radar equation (2.10), the maximum range R_{max} of radars is proportional to (4.1) and (4.2) for the conventional and single-antenna-based phased-array radars shown in Fig. 4-1.

$$R_{\mathrm{max,Conventional}}^4 \propto \frac{P_{TX} M^2 G_{Ant,TX} N G_{Ant,RX}}{F},$$
 (4.1)

$$R_{\mathrm{max,Single\ Antenna}}^4 \propto \frac{P_{TX} N'^3 G_{Ant}^2}{F},$$
 (4.2)

where P_{TX} is the output power per TX channel, G_{Ant} is the antenna gain, and F is the noise factor of each RX. Dividing (4.2) by (4.1) with the assumption of the similar TX

and RX specs for both systems, the range improvement factor (RI) can be calculated by

$$RI = \frac{R_{\text{max,Single Antenna}}}{R_{\text{max,Conventional}}} = \left(\frac{N^{\prime 3}}{M^2 N}\right)^{0.25}.$$
 (4.3)

With the equal array size for the both phased-arrays (i.e., N' = N + Ms), (4.3) simplifies to

$$RI|_{N'=M+N} = \left(\frac{M}{N} + \frac{N^2}{M^2} + \frac{3N}{M} + 3\right)^{0.25}.$$
 (4.4)

The range improvement in (4.4) versus the N/M has been plotted in Fig. 4-2. It can be seen from Fig. 4-2 that even for an equal number of channels for the TX and RX arrays (i.e., N/M = 1, a range improvement of 60% is achievable for the single-antenna architecture.

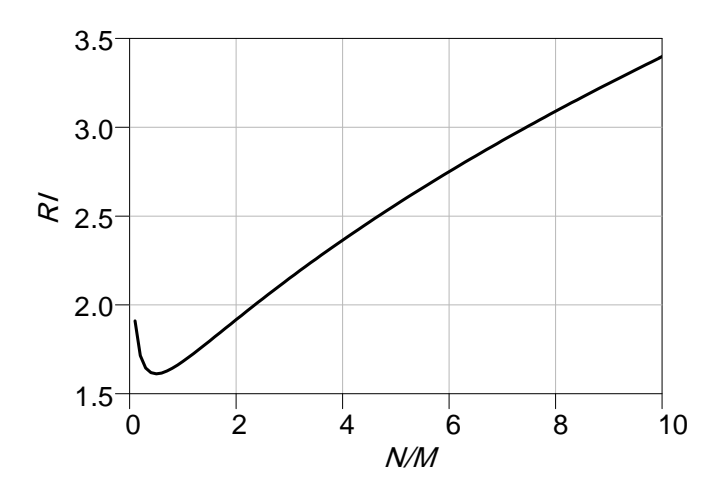


Fig. 4-2. Range improvement ratio of the single-antenna-based phased-arrays to conventional phased-arrays with the same array size and a similar performance of the TXs and RXs.

As mentioned, the large leakage from the TX to RX is the main drawback of the single-antenna TRX, which will be addressed in this thesis in detail.

4.2 Sharing a single antenna and the TX leakage issue

To implement a single-antenna radar front-end, the first issue is separating the transmit and receive signals through a single port, while there is neither frequency nor time

multiplexing available in FMCW radars. The key component is a wave director, which can distinguish the forward transmitting and reverse receiving waves such as circulators or directional couplers, as shown in Fig. 4-3. The circulators and directional couplers are well-known passive microwave components that can distinguish between the forward and reverse signals propagated or received from a port. Although circulators are the best option due to lower insertion loss (ideally no insertion loss) compared to the directional couplers with 3 dB intrinsic loss, however, they are not integratable on a chip since they need ferromagnetic materials [42]. Moreover, discrete commercialized circulators are available only for the lower microwave frequency bands. The mm-wave band circulators typically use waveguide connections, which require waveguide transitions, imposing extra cost, loss, and complexity for the radar sensor.

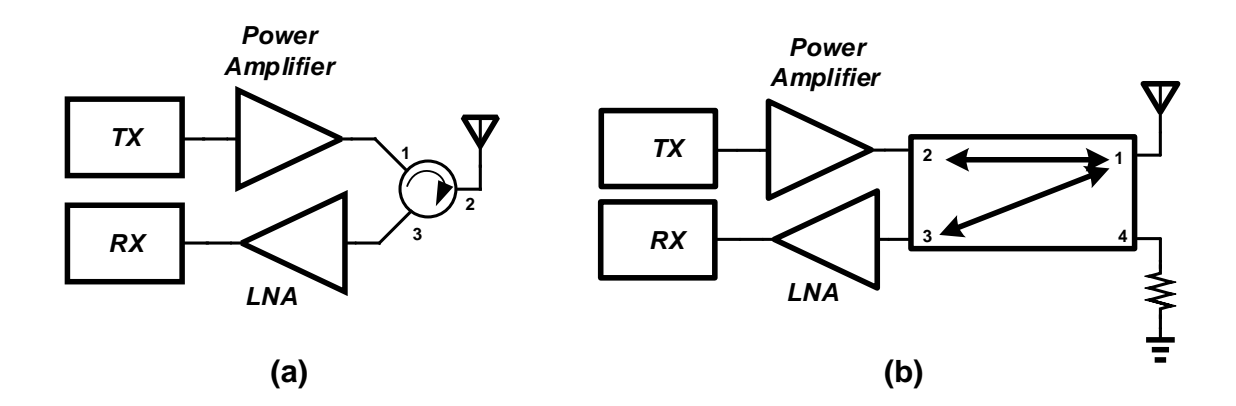


Fig. 4-3. Sharing the antenna port using (a) a circulator and (b) a directional coupler in a single-antenna front-end.

Active quasi-circulators [43–46] utilize active amplifier circuits to break the reciprocity of the passive components and provide separate paths for TX and RX blocks. However, due to the active nature of these structures, their linearity and noise performance are considerably limited. In addition, the performance is process voltage and tempreture PVT dependent, which is degraded with circuit mismatches. The performance will be more degraded due to the lower performance of the active devices at the mm-wave band.

Magnetic-free circulator circuits presented in [47,48], provide a non-reciprocal characteristic by employing an N-path filters architecture. Needing non-overlapping multi-phase clocks, and low resistance switches are the two big issues that make these not applicable

at the mm-wave bands. The implementation of the magnetic-free circulators presented in [49] at a lower mm-wave band shows high insertion loss and low isolation, which is comparable to the performance of passive directional couplers on CMOS chips.

The planar directional couplers, however, are promising alternatives, which can be integrated on-chip. While directional couplers are typically considered as bulky components (the size is proportional to the quarter wavelength) for on-chip integration, their size is feasibly reasonable at the mm-wave bands.

While the introduced circulators and directional couplers can separate the transmit and receive signals, the isolation level from the TX to the RX is typically limited to 20 dB due to intrinsic structural leakages and (or) antenna port mismatch. The following example can give us a sense of the total isolation level that is required for a single-antenna front-end to operate properly. Considering the input referred 1 dB compression point, as the desensitization factor of the RX, is a starting point. The input 1 dB compression point of a front-end in CMOS technology is -30 dBm typically at the mm-wave band [22]. Simulations show that the noise performance will be degraded even before reaching the compression point of the RX. From Table 3.3, the output power of -13 dBm is required for an SRR TRX with 0 dB NF. Assuming an NF of 13 dB for the RX, the required output power increases to 0 dBm. Therefore based on the compression point of the RX, an isolation level of more than 30 dB is required. Allowing for a 10 dB back-off, isolation of more than 40 dB is required. This level of isolation is barely achievable even for the separated TRX on the same CMOS die with the conductive substrate at the mm-wave band. In addition, there should be enough spacing maintained for the off-chip TX and RX antennas to maintain the isolation level, which further increases the insertion loss of the interconnects and increases the size of the sensor. Therefore, commercial designs avoid using high gain front-ends to prevent the RX from saturation for the separated antennas, typically, resulting in higher NF.

Among the literature, a few papers have considered this issue. The problem of shielding between TX and RX arrays is described in [31]. For minimizing the TX to RX leakage in the conductive substrate of CMOS technology, careful layout considerations, including

adding an extra gap between TXs and RXs, and separating power supply lines, have been suggested.

A cancellation technique called spillover cancellation is proposed in [50], which relieves the baseband circuits from saturation, caused by near reflections, in pulse-modulated continuous-wave (PMCW) radar RXs. The presented technique decreases the leakage problem for baseband circuits; however, the RF front-end is still susceptible to saturation. Therefore, this approach is not suitable for single-antenna operation.

The above discussion reveals the essence of a cancellation technique for increasing the isolation in the CW radars. One quick solution for mitigating the leakage issue is to design an antenna interface with higher intrinsic isolation. [51–53] improve the isolation level of the input directional coupler by using so-called balanced structures at microwave frequencies. However, the isolation of these structures is highly dependent on the process variations. In addition, antenna impedance mismatch is another factor that cannot be compensated by these approaches. Therefore, tunable cancellation techniques are required to be calibrated for any mismatches. Generally, impedance tuning and adding a cancellation path are two main approaches in order to provide an effective cancellation for these systems, as shown in Fig. 4-4(a) and (b), respectively.

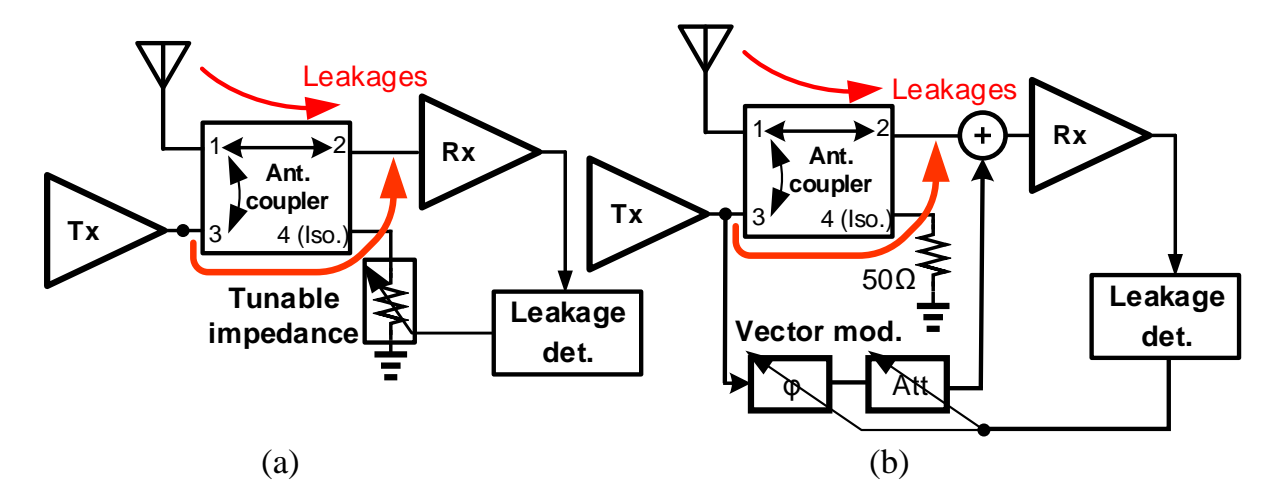


Fig. 4-4. Leakage cancellation schemes using (a) impedance tuning, and (b)cancellation path.

The tunable impedance, shown in Fig. 4-4(a), increases the isolation of the coupler by reflecting back an appropriate power of the TX signal toward the RX port, resulting in a cancellation at the input of the RX. An improved version of the balanced architecture

with impedance tuning capability to further increase the isolation level is reported in [53]. In practice, the proposed technique requires a digital processing algorithm to calibrate the impedance tuner. Since the conventional variable impedance circuits have numerous tuning parameters, complicated blind search digital tuning algorithms are required to find the optimum tuning parameters.

The vector modulator, shown in Fig. 4-4(b), on the hand, cancels the leakage signal by subtracting a controlled leakage replica at the input of the RX. The digitally controlled IQ-modulator-based cancellation feedback loop is introduced in [54, 55] to control the cancellation replica. The concept of the near reflected power canceller (RPC) using IQ-modulator-based analog feedback is presented in [56] for the first time. However, due to the complexity of the proposed architecture, it is not common in the designs.

In the rest of this chapter, the operation of the RPC is described as a preferred feedback-based canceller, and then, a novel cancellation architecture, which has the advantage of both the tunable impedance and the RPC, will be introduced.

4.3 Dynamic range enhancement techniques in FMCW radars

The dynamic range requirement of a radar RX is severely more difficult than a wireless communication RX since the propagation loss of a radar system is inversely proportional to R^4 , and R^2 for a wireless communication link. Besides this, when a wireless connection is established, the RX maintains the signal level constant by adjusting the gain and controlling the dynamic range of the front-end. However, this technique is not applicable to CW radars since the back-scattered signals come from different distances simultaneously. For FMCW radars, substituting the beat frequency (2.25) into the radar equation (2.6), the received power as a function of beat frequency (which corresponds to the distance of the target) can be calculated by

$$P_{RX} = \frac{P_{TX}G^2\lambda^2\sigma}{(4\pi)^3 \left(\frac{CT_0}{4\Delta f}f_b\right)^4}.$$
(4.5)

According to the above equation, if a second-order high-pass filter is added at the base-band, the amplitude variation of the received signal at the output of the baseband due to the distance of the target will be equalized and the dynamic range required for the following ADC will be relaxed. In other words, the high-pass filter with an amplitude increment of 40 dB/Dec can equalize the received power. The block diagram of an FMCW radar TRX, including equalizer, called sensitivity frequency control (SFC), is shown in Fig. 4-5. Since the SFC conceptually should be implemented in the baseband section, it cannot

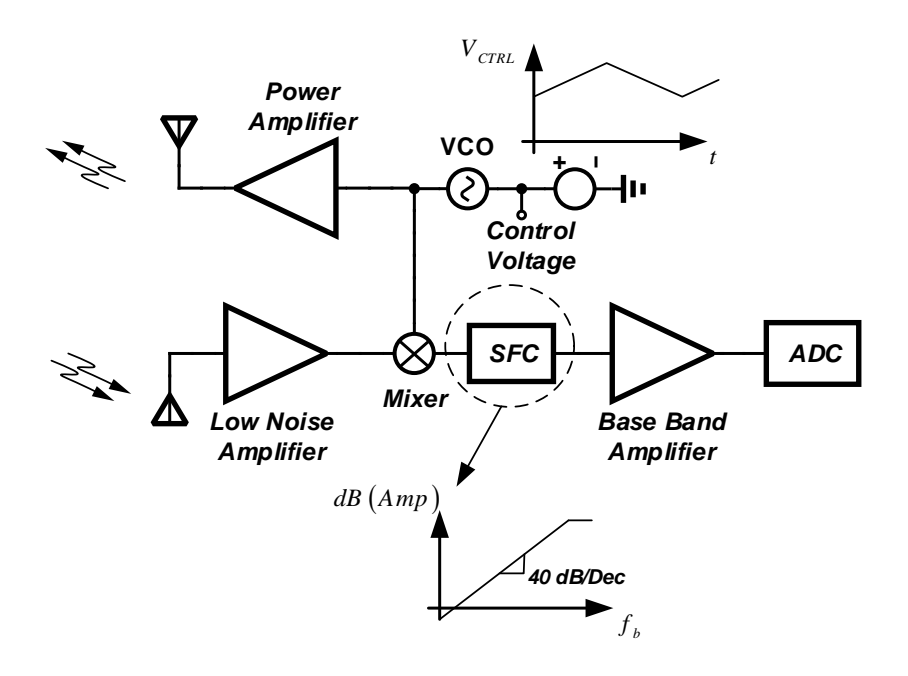


Fig. 4-5. Block diagram of a FMCW radar TRX using an SFC.

improve the dynamic range requirement of the RF circuits. For extending this advantage to the RF circuits, the concept of the SFC is applied to the RF using a feedback circuit, which is already introduced as the RPC, as shown in Fig. 4-6. The RPC with the analog feedback forms a sharp and accurate moving notch filter right at the input of the RX, which traps the leakage signals into the notch and passes the wanted received signal to the input RX for amplification. The feedback is analyzed using the frequency transnational technique [57].

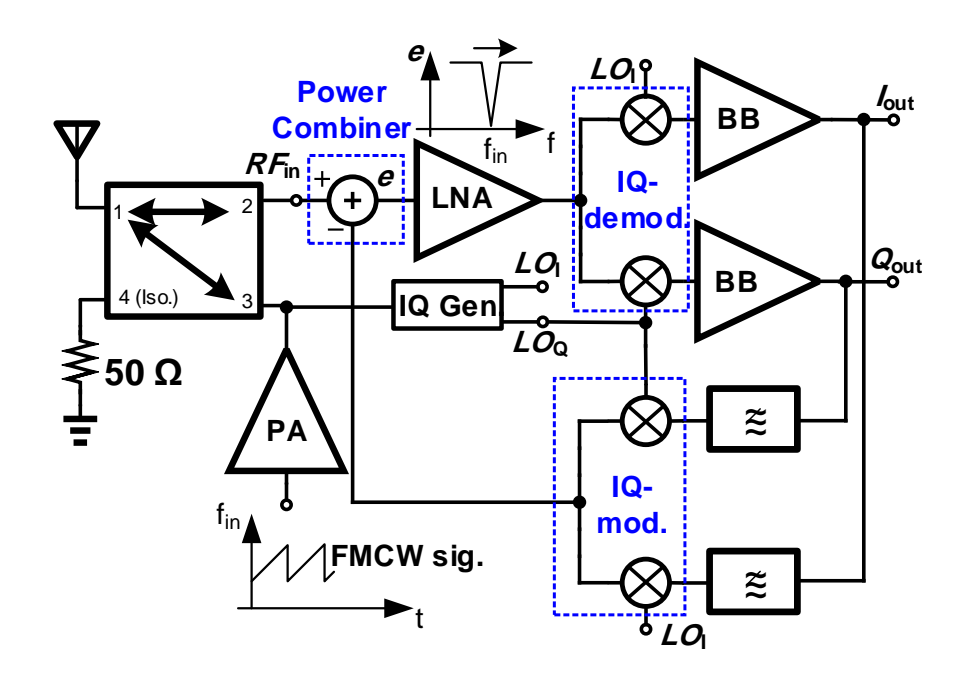


Fig. 4-6. Feedback architecture to the relax RF dynamic range of the receiver in FMCW radars.

4.3.1 Feedback analysis of the RPC

Using the frequency translation technique [57], the high-frequency circuit can be transferred to the baseband frequency or vice-versa. The frequency transfer is defined by the local oscillator (LO) frequency. Applying this method, the simplified block diagram of the feedback loop is illustrated in Fig. 4-7. From the feedback theory, the frequency responses and the cancellation factor (CF) of the closed-loop system is expressed by (4.6(a) and (b)), respectively:

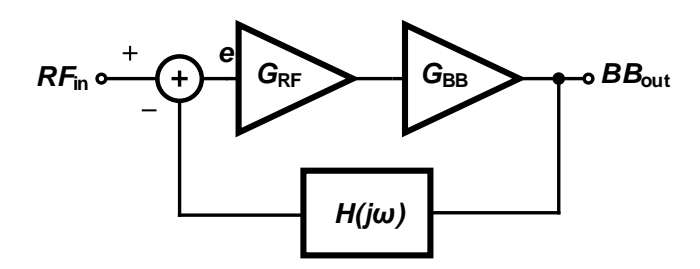


Fig. 4-7. Simplified model of the feedback circuit.

$$\frac{BB_{out}}{RF_{in}} = \frac{G_{RF}G_{BB}}{1 + G_{RF}G_{BB}H(j\omega)}$$
(4.6a)

$$CF = \frac{RF_{in}}{e} = 1 + G_{RF}G_{BB}H(j\omega), \qquad (4.6b)$$

where ω is the difference between the RF and LO frequencies (baseband frequency), G_{RF} and G_{BB} represent RF gain, including LNA, down-converter mixers, and baseband gain, respectively, and $H(j\omega)$ represents the low-pass filter frequency response followed by the IQ-modulator gain in Fig. 4-6.

Assuming the frequency of the input RF is exactly equal to the LO frequency, which is an analogy to the case of the leakage signal in FMCW radars, then $\omega = 0$ in (4.6) yields

$$\frac{BB_{ot}}{RF_{in}} = \frac{G_{RF}G_{BB}}{1 + G_{RF}G_{BB}H(j0)} \approx \frac{1}{H(j0)}$$
(4.7a)

$$CF = \frac{RF_{in}}{e} = 1 + G_{RF}G_{BB}H(j0) \approx G_{RF}G_{BB}H(j0).$$
 (4.7b)

Equation (4.7) shows that the conversion gain and error signal are considerably reduced when the RF and LO frequencies are similar. In other words, the leakage signal in the FMCW will be significantly attenuated at the input of the LNA, resulting in dynamic range relaxation for the RF and baseband circuits simultaneously. On the other hand, when the frequency difference between the RF and LO frequency increases (i.e., for the wanted reflection signals of a target located far away from the radar), the loop will be open because of the low-pass characteristics of $H(j\omega)$, which yields to a conversion gain of $\frac{BB_{\alpha t}}{RF_{in}} \approx G_{RF}G_{BB}$.

Considering these two extremes and applying a linearly modulated LO signal to the circuits in a FMCW radar, it can be imagined that there is a moving notch filter at the RF frequency, which is tracking the LO frequency instantaneously.

In the following sections, noise performance, the effect of IQ-imbalance, and the stability of the loop will be studied in detail.

4.3.2 Noise analysis of the closed-loop receiver

• Noise of RX and the cancellation feedback: The noise sources of the feedback configuration are depicted in Fig. 4-8. The RX NF is expressed by:

$$NF = 1 + \frac{\overline{V_{nFB}^2} + \overline{V_{nRF}^2}}{4KTR_s},\tag{4.8}$$

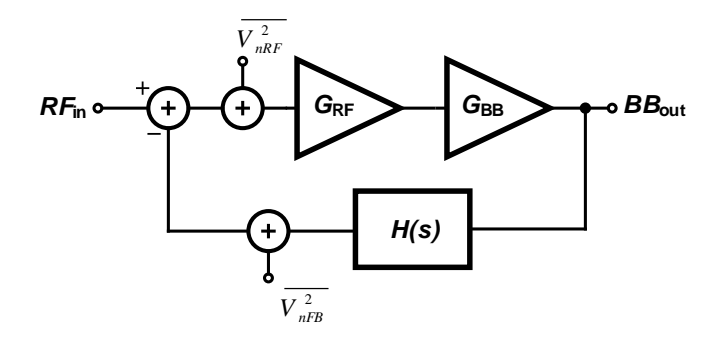


Fig. 4-8. Noise sources in the feedback model.

where $\overline{V_{nFB}^2}$ is the equivalent output-referred noise of the low-pass filter plus IQ-modulator, and $\overline{V_{nRF}^2}$ is the input-referred noise of the LNA, IQ-demodulator and the baseband amplifiers. Minimizing the output noise level of the feedback components is important to reduce the RX NF since it is directly added to the input of the RX. It should be noted that the antenna directional couplers and the power combiner at the input of the RX impose extra passive loss and accordingly increase the NF directly.

• Noise of the TX: Besides the RX noise sources, the PN of the oscillator followed by the output noise of the TX leakage can severely degrade the SNR of the received signal, as described in Section 3.3.4 and Section 3.3.3. It has been shown that due to the NF of the TX amplifiers, it is possible that the noise floor at the input of the RX could be increased. Another noise source that can degrade the performance is the amplitude noise (AN). In fact, the output noise of the TX can be modeled by PN and AN noise sources. While it has been shown that the PN can be significantly attenuated due to the range correlation effect in the IQ-demodulator, there is no such mechanism to attenuate the AN. Assuming an AN noise level of -140 dBc/Hz at 1 MHz offset frequency for a TX with an output power of 0 dBm, the input noise floor at the input of the RX will be -160 dBm/Hz for a given isolation level of 20 dB. This corresponds to 14 dB NF. The problem of the AN arises from the IQ-modulator LO port characteristics. While the mixers are sensitive to the phase of the LO, as shown in Fig. 4-9(a), they are not responsive to the amplitude variations,

as shown in Fig. 4-9(b). As a result, the replica of the leakage signal generated by the IQ-modulator, does not inherit the AN, and after subtraction, the AN noise will remain at the input of the RX, as demonstrated in Fig. 4-10.

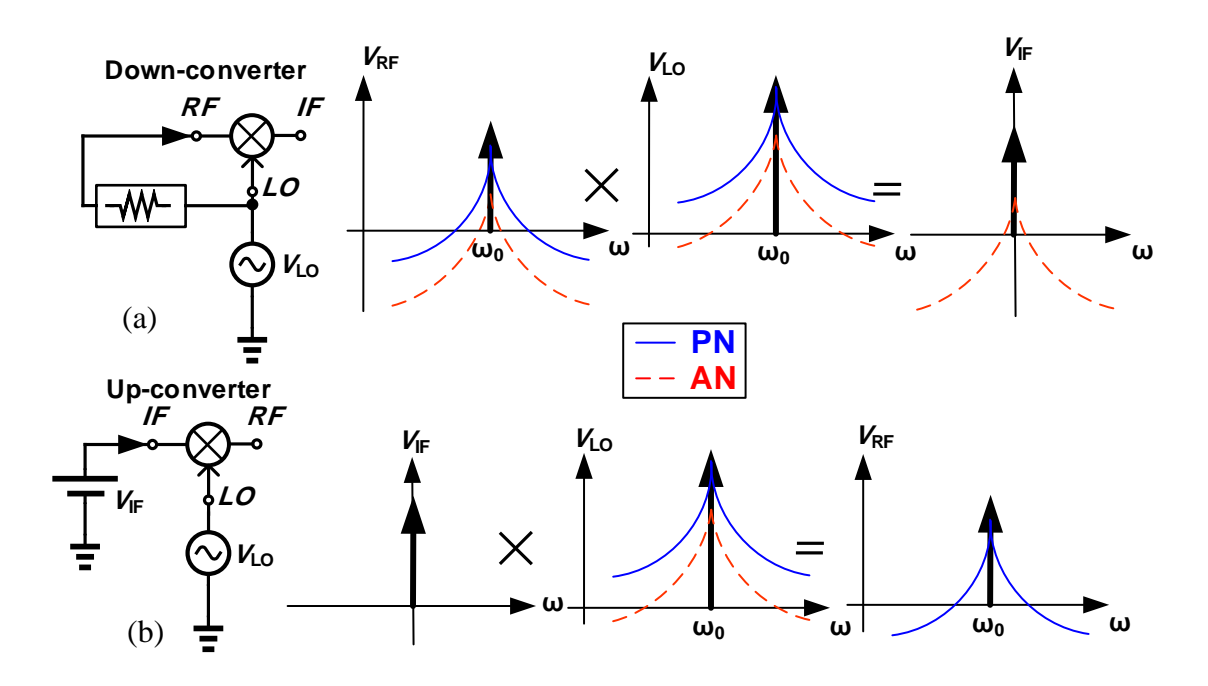


Fig. 4-9. (a) PN cancellation at the IF port in a down-converter due to PN correlation effect. (b) PN modulation in an up-converter.

4.3.3 Effect of IQ-imbalance on the leakage cancellation performance

As depicted in Fig. 4-6, for proper operation of the feedback cancellation circuit, inphase and quadrature LO phases are required. Since practically, the phase and amplitude
mismatches for the I and Q paths are inevitable at the mm-wave band, the IQ-imbalance
effect is considered in this section. When calibration techniques can be employed to reduce
the mismatch effects at low-frequency circuits, they are not quite effective at the mm-wave
band.

For studying the problem, first, assume the loop is open as shown in Fig. 4-11. Due to IQ-mismatches, an undesirable image signal will be generated at the output of the IQ-modulator, making a limited open-loop image-rejection, defined by $IR_{OL} \stackrel{\triangle}{=} \left(\frac{A_{RF}}{A_{IMG}}\right)^2$,

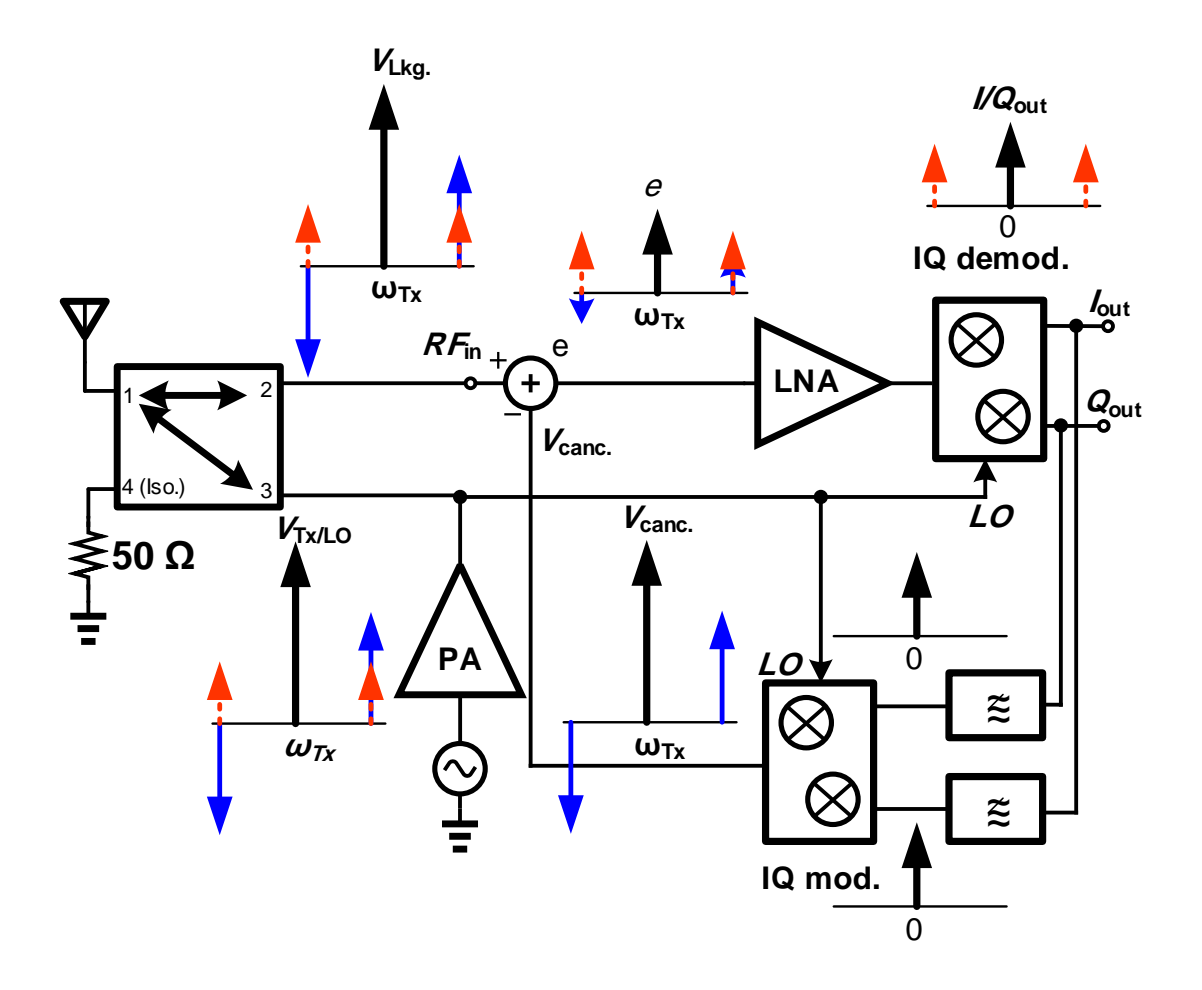


Fig. 4-10. AN and PN of the TX in the RPC.

where A_{RF} and A_{IMG} is the amplitude of the output RF and image signal, respectively.

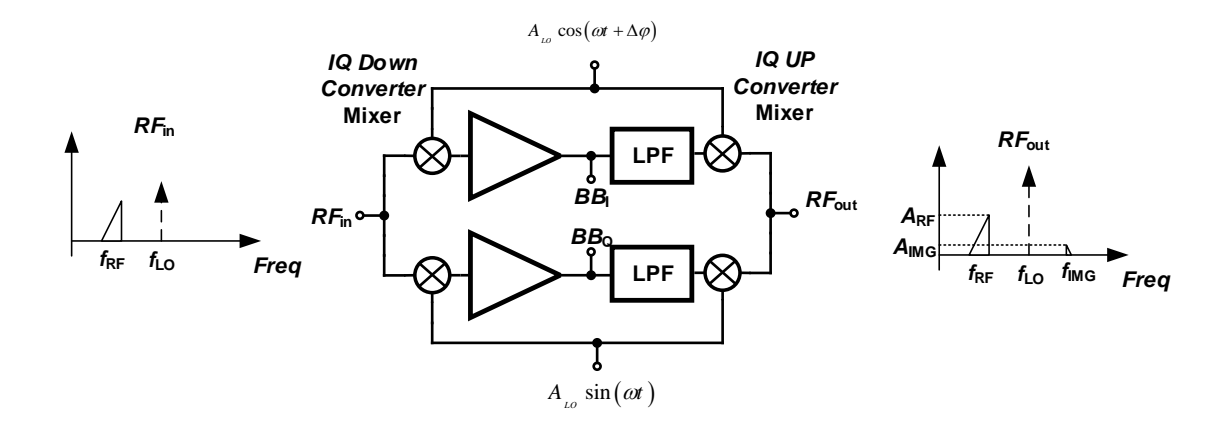


Fig. 4-11. Limited open-loop image-rejection due to IQ-imbalance.

Now let us close the loop as shown in Fig. 4-12. The unwanted image signal acts as

another source of interference for the RX since there is no image content at the input leakage signal to be canceled by. Assume the input RF signal is expressed by

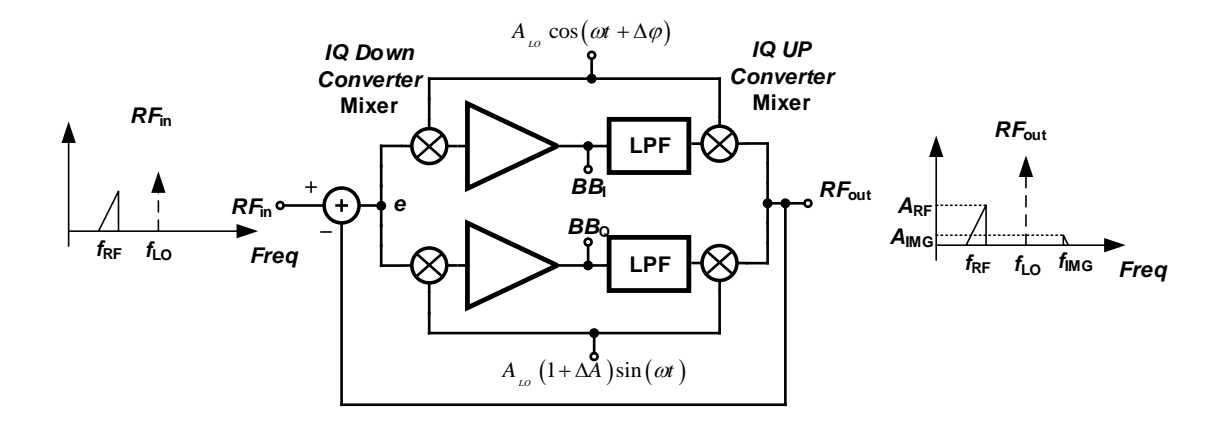


Fig. 4-12. Image-rejection in the closed-loop operation.

$$RF_{in} = A_{RF,in}\cos(\omega_{RF}t), \tag{4.9}$$

and the output signal is expressed by

$$RF_{\alpha t} = A_{RF,\alpha t} \cos(\omega_{RF}t) + A_{IMG,\alpha t} \cos(\omega_{IMG}t), \tag{4.10}$$

where ω_{RF} and ω_{IMG} is the RF and image frequency, respectively. The error signal (e) in Fig. 4-12 is equal to

$$e = RF_{in} - RF_{\alpha t} = (A_{RF,in} - A_{RF,\alpha t})\cos(\omega_{RF}t) - A_{IMG,\alpha t}\cos(\omega_{IMG}t). \tag{4.11}$$

Passing the error signal through the IQ-demodulator, baseband amplifiers and IQ-modulator with a limited IR_{OL} yields the following output signal:

$$RF_{\alpha t} = G\left(A_{RF,in} - A_{RF,\alpha t} - \frac{A_{IMG,\alpha t}}{\sqrt{IR_{OL}}}\right)\cos(\omega_{RF}t) + G\left(\frac{A_{RF,in} - A_{RF,\alpha t}}{\sqrt{IR_{OL}}} - A_{IMG,\alpha t}\right)\cos(\omega_{IMG}t),$$

$$(4.12)$$

where G is the total gain of the chain. Equating (4.12) and (4.10) results in

$$A_{RF,at} = \frac{G + \left(1 - \frac{1}{IR_{OL}}\right)G^2}{1 + 2G + \left(1 - \frac{1}{IR_{OL}}\right)G^2} A_{RF,in}$$
(4.13a)

$$A_{IMG,\alpha t} = \frac{\frac{G}{\sqrt{IR_{OL}}}}{1 + 2G + \left(1 - \frac{1}{IR_{OL}}\right)G^2} A_{RF,in}$$
(4.13b)

Dividing (4.13a) by (4.13b), the closed-loop image-rejection ratio (IR_{CL}) can be calculated by

$$IR_{CL} = \left(\frac{A_{RF,at}}{A_{IMG,at}}\right)^{2} = \left(\frac{\frac{G + \left(1 - \frac{1}{IR_{OL}^{2}}\right)G^{2}}{1 + 2G + \left(1 - \frac{1}{IR_{OL}^{2}}\right)G^{2}}A_{RF,in}}{\frac{G}{IR_{OL}}}\right)^{2} = \left(1 + \left(1 - \frac{1}{IR_{OL}}\right)G\right)^{2}IR_{OL}.$$

$$(4.14)$$

More importantly, the cancellation factor (CF) is defined by the ratio of the power of the input leakage at the input to the total power of the image and the RF signals at the error node (i.e., e) after the cancellation. The error signal can be calculated by

$$e = \frac{(1+G)\cos(\omega_{RF}t) - \frac{G}{\sqrt{R_{OL}}}\cos(\omega_{IMG}t)}{1 + 2G + \left(1 - \frac{1}{R_{OL}}\right)G^2} A_{RF,in}.$$
 (4.15)

The total power of the error is equal to

$$|e|^2 = \frac{(1+G)^2 + \frac{G^2}{R_{OL}}}{\left((1+G)^2 - \frac{G^2}{IR_{OL}}\right)^2} |A_{RF,in}|^2.$$
(4.16)

Therefore, CF equals

$$CF = \frac{\left((1+G)^2 - \frac{G^2}{IR_{OL}} \right)^2}{(1+G)^2 + \frac{G^2}{IR_{OL}}}.$$
(4.17)

The closed-loop image-rejection ratio and the cancellation factor versus open-loop image-rejection ratio is plotted for different loop gains (G) in Fig. 4-13 and Fig. 4-14, respectively. It can be seen that even with only an open-loop image-rejection of 3 dB, corresponding

to an IQ phase imbalance of 50° or amplitude imbalances of 15 dB, a cancellation level of better than 30 dB is achievable for a loop gain of greater than 40 dB. This ensures robust operation for the IQ-modulator-based feedback architecture without the need for IQ correction circuits.

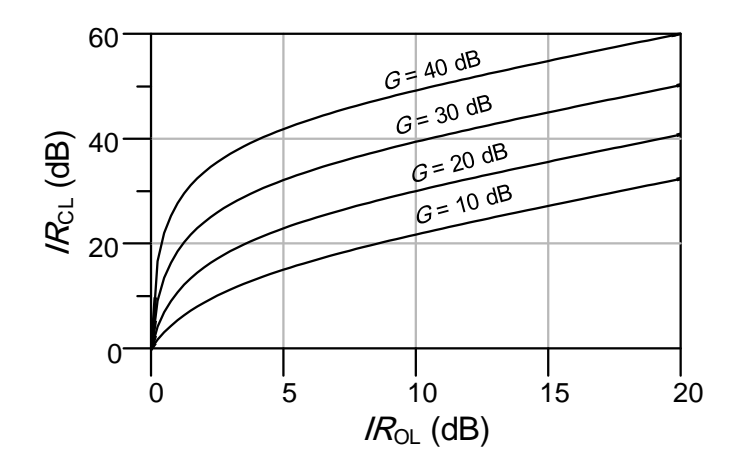


Fig. 4-13. Closed-loop versus open-loop image-rejection ratio for the different loop gains.

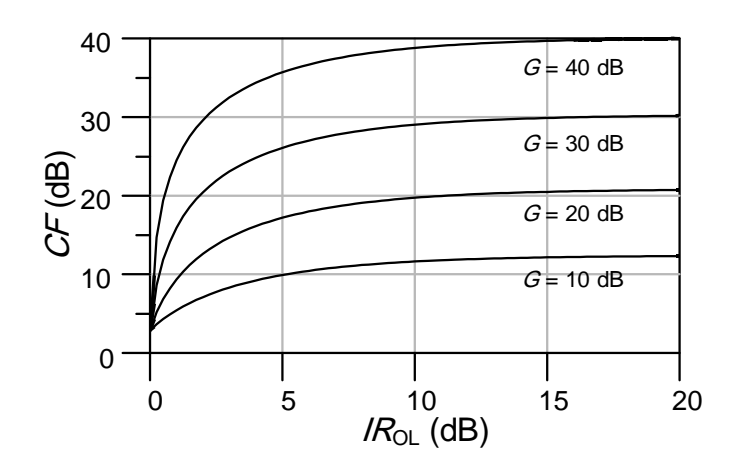


Fig. 4-14. Cancellation factor versus open-loop image-rejection ratio for the different loop gains.

4.3.4 Stability of the feedback loop in the cancellation architecture

Similar to any feedback system, the introduced architecture is prone to the instability issue. For studying the stability of the loop, we can use the simplified model, shown in Fig. 4-7. The phase response of the loop is determined by the loop filter $(H(j\omega))$. Although RF and baseband circuits produce extra phase shifts, compared to the loop filter they are quite wideband. In other words, the poles of the RF circuits are quite far away when their transfer-functions are shifted-down to the baseband domain, as performed in the simplified model in Fig. 4-7. As a result, the dominant pole of the circuit is defined by the loop filter $(H(j\omega))$.

As discussed in Section 4.3, the optimum SFC characteristic is a second-order high-pass filter. From the feedback theory, in order to implement the high-pass characteristic, $H(j\omega)$ should have a low-pass characteristic. Therefore, to make a second order high-pass filter, the loop filter should be implemented by a second-order integrator $(H(j\omega) = \frac{1}{s^2})$. This implies that the loop gain of the feedback system has two poles at the origin resulting in a zero degree phase margin. The above discussion reveals that it is not possible to implement this system by a second-order loop filter. In practice, to avoid the instability issue, the order of the loop filter should be reduced to one. Though a first-order loop filter is not the optimum equalizer, it can relax the dynamic range requirements of the RF and baseband circuits. Moreover, it is possible to add one more first-order high-pass filter at the output of the baseband in order to completely relax the dynamic range requirement of the following ADC.

While it is supposed that the poles of RF circuits are far away, they produce unknown phase shifts due to the RF routing and delays in the LNA and mixers, which can cause instability. Therefore, it is necessary to implement a phase offset compensation circuit called a phase compensator (PC), which can be implemented using a baseband phase interpolator circuit with minimum overheads on the power consumption, area, and complexity.

4.3.5 System level implementation of the RPC

The full block diagram of the introduced closed-loop dynamic range enhancement technique for FMCW radars, including antenna coupler, summing node combiner, IQ-modulator and -demodulator, LNA, TX amplifier, baseband amplifiers, LO paths, and the PC to compensate for the phase offset of the loop, is depicted in Fig 4-15. A frequency tripler is adopted in order to feed the lower frequency signal from an off-chip source for generating the radar signals. The introduced RPC, though makes a moving notch filter and is robust against IQ-mismatches, suffers from the following items:

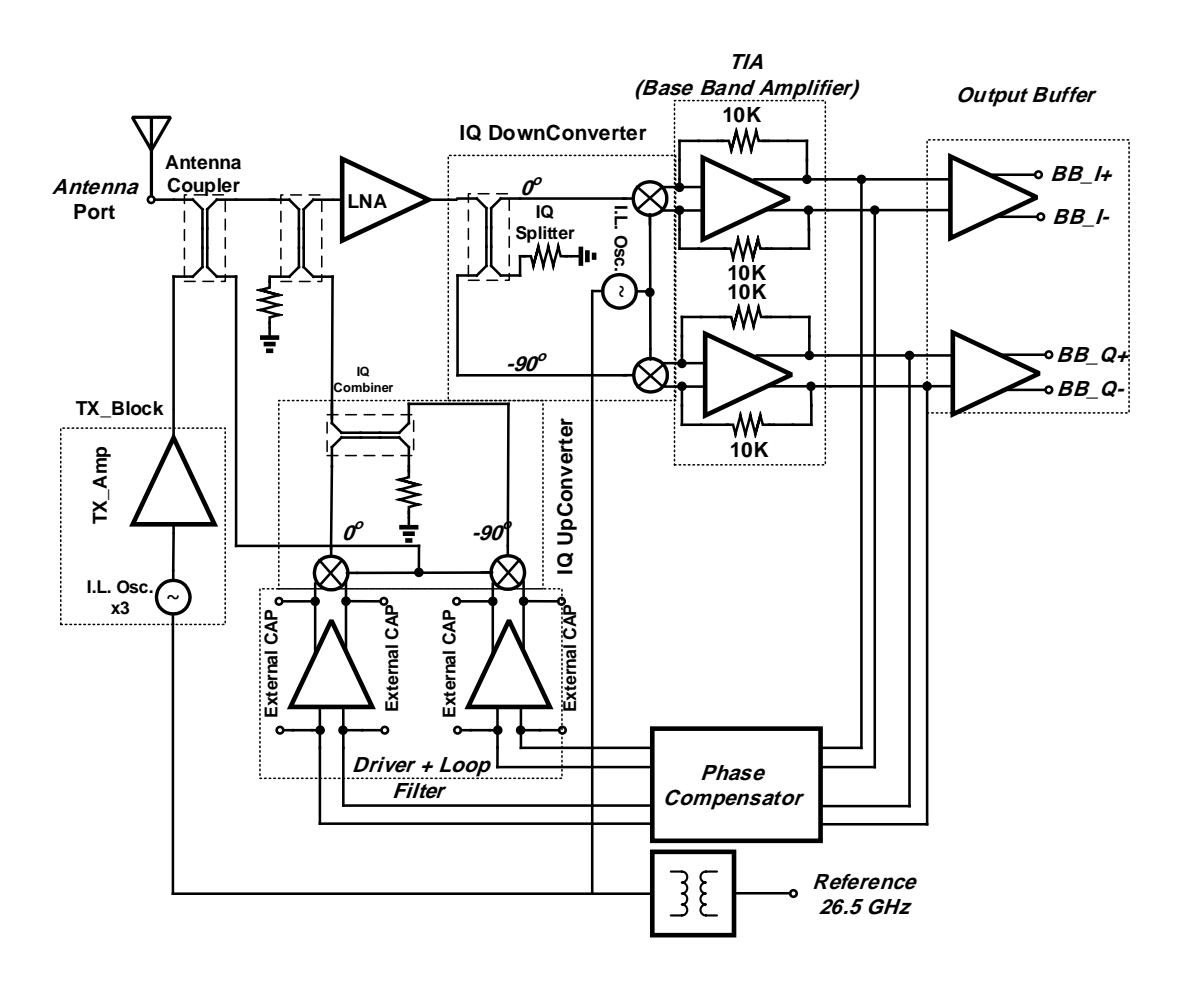


Fig. 4-15. Full block diagram of the closed-loop single-antenna architecture.

1. The IQ-modulator needs extra LO signals, and has to be directly coupled from TX signal to maximize the PN attenuation.

2. One realization of the antenna coupler, the IQ-modulator, and the summing node combiner is shown in Fig. 4-16. It is not possible to use a conventional current or voltage combiner, which normally is utilized at low-frequency circuits, at the mm-wave band since the parasitic components do not permit having very high or very low impedance nodes. Therefore, any summing node should be implemented by the passive power combiners or couplers. This not only occupies extra area on the chip but also increases the insertion loss of the RF path right at the input of the RX, directly increasing the NF.

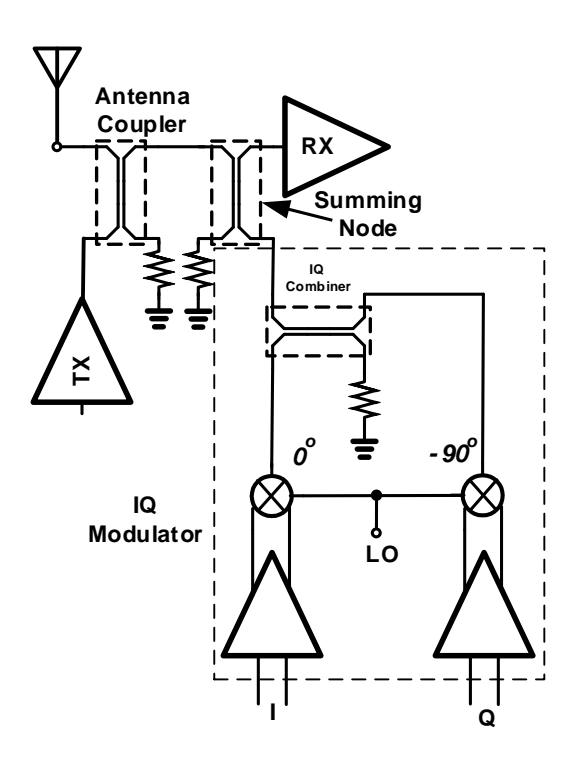


Fig. 4-16. Schematic diagram of IQ-modulator, summing node and antenna coupler.

3. As discussed, the AN issue is a potential degradation factor.

In order to address the above issues, a novel cancellation technique is proposed, which has the same functionality as the IQ-modulator in terms of forming a moving notch filter at the input of the RX, while the AN issue is solved and there is no need for the summing node combiner.

4.4 Proposed cancellation technique

In the previous sections, we showed that the IQ-modulator-based cancellation provides a moving notch filter at the input of the RX by taking advantage of an analog feedback loop. The IQ-mismatch robustness and not being sensitive to PVT variations are other benefits of using the feedback circuit. However, it has several drawbacks as mentioned in Section 4.3.5. The impedance tuning technique, on the other hand, does not have the disadvantages of the IQ-modulator-based canceller in terms of AN, extra insertion loss of the combiner, and the complexity of the IQ-modulator circuit. However, it requires a tunable impedance, which typically has numerous parameters [58–60] for tuning and needs a digital processor. Moreover, the moving notch filter characteristic is only achievable by real-time digital processing. In this thesis, we propose a novel cancellation technique that has the benefits of both the feedback and tunable impedance architectures.

The block diagram of the proposed idea is demonstrated in Fig. 4-17. The idea is based on a variable reflector (VR), in which the real and imaginary parts of its reflection coefficient are controllable independently using the I&Q signals of the IQ-demodulator as in the RPC. In order to understand the operation principle of the proposed architecture, the VR should be introduced. The VR with the orthogonal real and imaginary parts can be modeled as follows:

$$\Gamma_{VR} = f(I_{ctrl}) + jf(Q_{ctrl}), \tag{4.18}$$

where $I_{\tt ctrl}$ and $Q_{\tt ctrl}$ are the two controlling signals of the VR, as shown in Fig. 4-17, and -1 < f(x) < 1 is a monotonic function for ensuring the stability of the feedback loop. The cancellation signal $(V_{\tt cncl})$ reflected by the VR through the antenna coupler can be calculated by

$$V_{\text{cncl}} = V_{\text{TX}}^{+} S_{43} S_{24} \bigg(f(I') + j f(Q') \bigg), \tag{4.19}$$

where S_{ij} are the scattering parameters of the antenna coupler, V_{TX}^+ is the incident voltage to the coupler generated by the TX, and I' and Q' are the two controlling signals of the

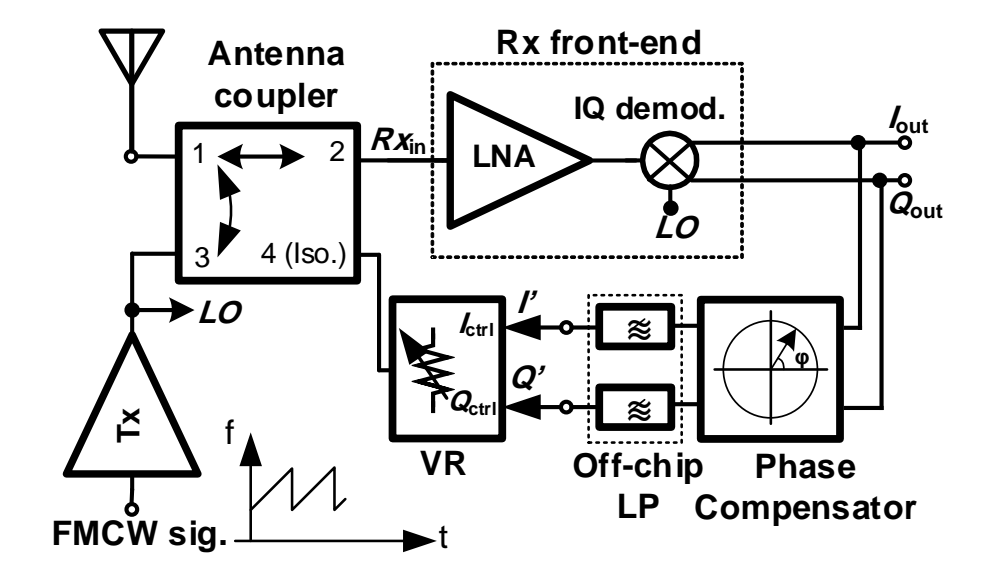


Fig. 4-17. Block diagram of the proposed leakage cancellation architecture.

VR as shown in Fig. 4-17. I' and Q' are related to $I_{\tt out}$ and $Q_{\tt out}$ as follows:

$$I' + jQ' = H(j\omega)e^{j\phi}(I_{\text{out}} + jQ_{\text{out}}), \tag{4.20}$$

where $H(j\omega)$ is the frequency response of the low pass filters at the baseband domain (ω) , and ϕ is a phase offset provided by the PC, discussed earlier for the stability issue in Section 4.3.4.

The RX input signal (RX_{in}) is the superposition of the cancellation signal (V_{cncl}) and the other RF signals (RF_{in}) , including the leakage and wanted back-scattered signals of targets, that enter to the RX. The output IQ signals can be calculated using

$$G(RF_{in} + V_{cncl}) = I_{out} \tag{4.21a}$$

$$-jG(RF_{in} + V_{cncl}) = Q_{out}, \qquad (4.21b)$$

where G is the RX conversion gain. Assuming $f(x) = \alpha x$, a linear function for simplicity, and substituting (4.19) and (4.20) in (4.21), the conversion gain and the cancellation

factor can be calculated by the following equations:

$$\frac{I_{\text{out}}}{RF_{\text{in}}} = \frac{G}{1 - 2GV_{\text{TX}}^{+} S_{43} S_{24} \alpha H(j\omega) e^{j\phi}}$$
(4.22a)

$$\frac{Q_{\text{out}}}{RF_{\text{in}}} = \frac{-jG}{1 - 2GV_{\text{Tx}}^{+}S_{43}S_{24}\alpha H(j\omega)e^{j\phi}}$$
(4.22b)

$$CF = \frac{RF_{\text{in}} + V_{\text{cncl}}}{RF_{\text{in}}} = 1 - 2GV_{\text{TX}}^{+} S_{43} S_{24} \alpha H(j\omega) e^{j\phi}. \tag{4.23}$$

Equations (4.22) and (4.23) for the proposed cancellation are analogous to (4.6) in the IQ-modulator-based feedback architecture. Similarly, for the low baseband offset (i.e., dc offset), which corresponds to the leakage signal, the cancellation factor is maximized to $1+2GV_{\text{TX}}^+S_{43}S_{24}\alpha H(0)$ if the PC has been properly adjusted for negative feedback. On the other hand, for the higher baseband frequency offsets, which correspond to the reflected signals from objects, the cancellation factor is minimized to 1. The analog feedback loop again forms a moving notch filter at the input of the RX. To complete the discussion, it is worth noting the following items.

• Stability of the Loop: It can be observed from (4.22) and (4.23) that the loop will create positive feedback if $\phi = 0$ and all the parameters have positive signs. The PC circuit is required to ensure the stability of the feedback, as mentioned in Section 4.3.4. The PC does not require to track the phase variations of the RF circuits to maintain the stability since the dominant pole of the circuit is determined by the low pass filters and the phase of the RF circuits does not vary significantly in the operating frequency.

The next ambiguity is the phase of the transmit signal (i.e., $\angle V_{\text{TX}}^+$), which is unknown and may change after each start-up of the circuits. The uncertainty is because of the fact that the phase of the IQ-demodulator also depends directly on the phase of the LO signal, which is acquired from the TX. As a result,

$$\angle G = \angle \phi_0 - \angle V_{\mathtt{TX}}^+, \tag{4.24}$$

where $\angle \phi_0$ is the structural phase shifts due to delays in the LO and RF paths. The

negative sign in (4.24) is because of the down-conversion operation. Therefore, in total, the effect of the phase of the transmit signal will be canceled out in (4.21) and (4.22).

- TX AN Cancellation Property: The AN cancellation property of the proposed architecture can be seen from (4.19). The generation of term V_{TX}^+ in the cancellation signal implies that the cancellation signal is inheriting all the noise characteristics from the TX, which is also the source of leakages.
- Loop Gain of the Architecture: While it can be inferred from (4.23) that the higher TX output power results in a better cancellation factor, it should be noted that increasing the output power directly results in an increment of the leakage power as well. Therefore, roughly speaking, the total power of the leakage remains constant after the cancellation regardless of the TX output power. From (4.22) and with the given parameters of G = 100 = 40 dB, V_{TX} = 0.45V = 3 dBm, S₄₃ = S₂₄ = 0.7 = -3 dB (ideal directional couplers), α = 0.5V⁻¹ and H(jω) = 300 × 2 × π/jω (the frequency response of an integrator as the loop filter implemented by a Gm cell and an off-chip capacitor of 100 nF), the calculated -3 dB corner frequency of the moving notch filter approximately equals 6.75 kHz. The above parameters are the approximated values that are obtained from simulations.

A new circuit for the VR with the orthogonal real and imaginary part controls, as the key building block of the proposed architecture, will be proposed in the next chapter.

Chapter 5

Design and simulation of building

blocks

In this chapter, the circuit level implementation and simulation of our proposed single-antenna front-end is studied. As shown in Fig. 4-17, the proposed single-antenna architecture comprises the antenna coupler, TX amplifier, LNA, IQ-demodulator, phase compensator (PC), and the variable reflector (VR), which will be shown in this chapter in details. At the end of the chapter, the system level simulations of the proposed architecture will be demonstrated.

Before starting to design, the technology process should be introduced. TSMC 65-nm GP CMOS technology is chosen for this design because of the following reasons: 1) the cut-off frequency (f_t) of the active devices is up to 250 GHz, which has enough margin to be used for our design at W-band; 2) the supply voltage of 1.2 V of this technology node is more suitable for generating higher power amplifiers; 3) the back-end metalization of 65-nm process provides an option with an ultra thick copper metal layer, which is very important to minimize the loss of the passive circuits; 4) the cost of this technology is considerably lower than the more advanced process such as 40-nm.

The technology consists of nine metal layers with an ultra-thick top copper layer of 3.4 um. The bulk conductivity of 10 Ω .cm is used in the electromagnetic (EM) simulation parameters to model the substrate conductivity and loss of the CMOS process. Since

the designs are very sensitive to the parasitic components at the mm-wave band, all the passive structures have been designed and simulated using ADS Momentum, HFSS, and EMX EM-simulators. Fig. 5-1 illustrates the simplified back-end metal stack-up including M1, M8, and M9, which are widely used in the passive structures.

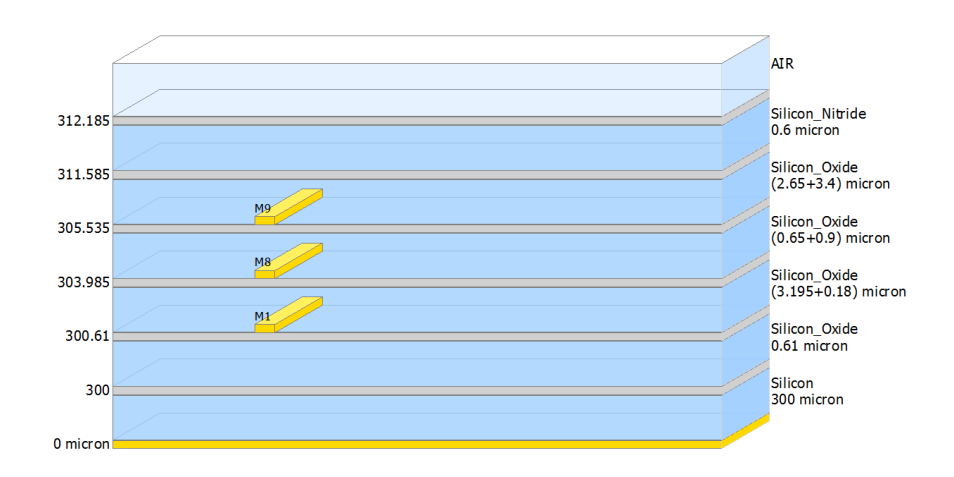


Fig. 5-1. Simplified cross section of 65-nm process used in the EM-simulations.

5.1 Transmission line structure

One of the essential components at the mm-wave is the transmission line (t-line). T-lines are widely used to carry the high-frequency signals inside the chip, and to do impedance transformations. Among different possibilities for the T-lines, the co-planar waveguide (CPW) structure is used in this design because of its lower insertion loss and design flexibility compared to the microstrip structures. The simulated insertion loss and matching for two 50 Ω CPWs with a length of 1-mm are depicted in Fig. 5-2. Though the insertion loss of the line is less for the wider metal width, the narrower structure is used to reduce the area overhead of the t-line. It should be noted that the insertion loss is only increased by 0.3 dB/mm, which is acceptable for short lines.

5.2 Antenna coupler

As described in Chapter 4, the single-antenna requires a signal separator. Planar directional couplers are good candidates for this purpose. Planar on-chip 90° hybrid couplers

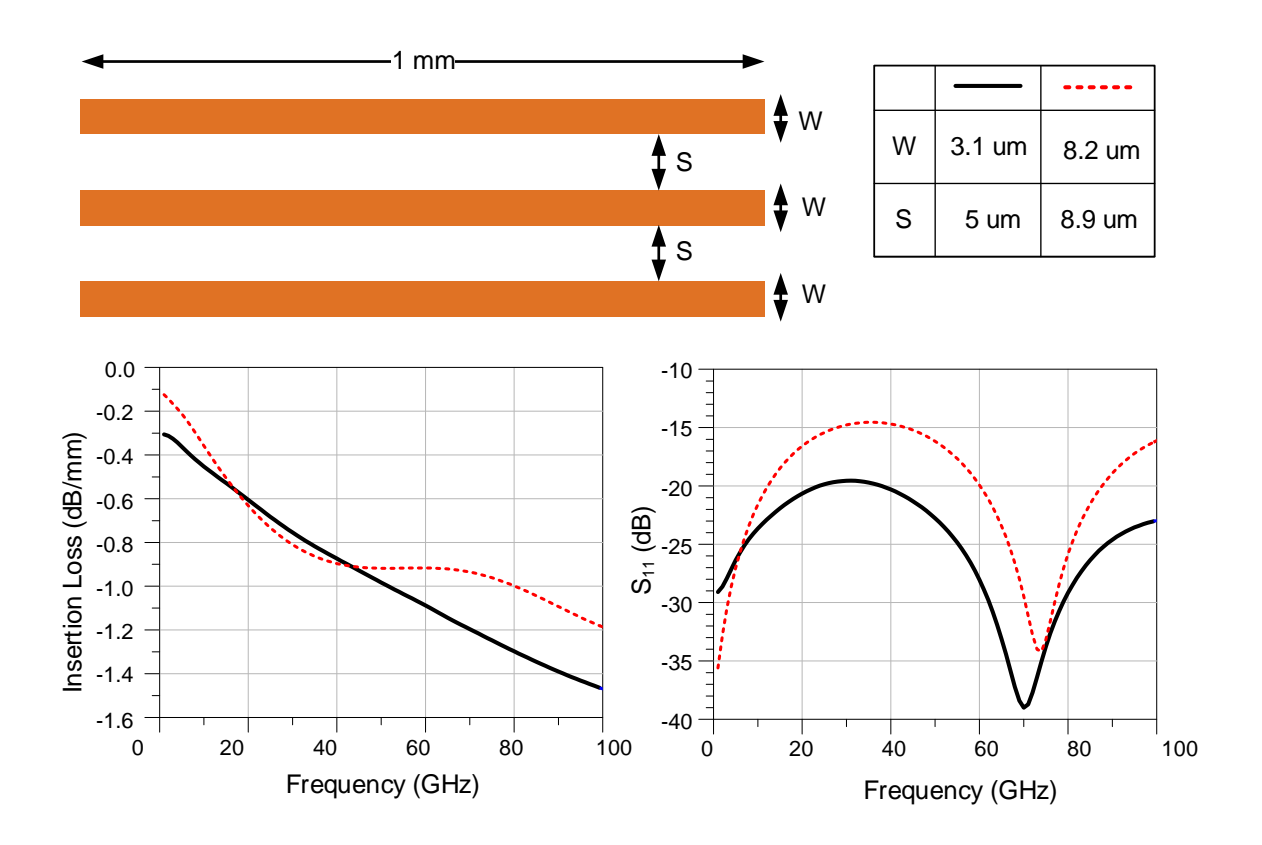


Fig. 5-2. Simulated insertion loss and matching of CPW t-line.

are extensively used in the reflective type phase shifters [61–63]. A quarter wavelength coupled line structure is used in this design for its wideband operation. In order to realize the required even- and odd-mode characteristic impedances, the CPW structure is used, which is also compatible with the t-lines. The schematic, layout, and the simulation result of the 90° hybrid directional coupler used in this design are depicted in Fig. 5-3.

5.3 LNA

As described in Chapter 3 and 4, it is necessary to use an LNA for suppressing the noise of the following stages in the RX. Particularly, the flicker noise of the baseband circuits is a dominant source of the noise up to 1 MHz in CMOS technology, which is within the spectrum of the received signals in the FMCW radars. In addition, due to extra loss at the mm-wave band, the role of the LNA is more critical.

In order to design the LNA, it is necessary to characterize the active devices. Since the NMOS transistors have a better performance in terms of speed and parasitics, the

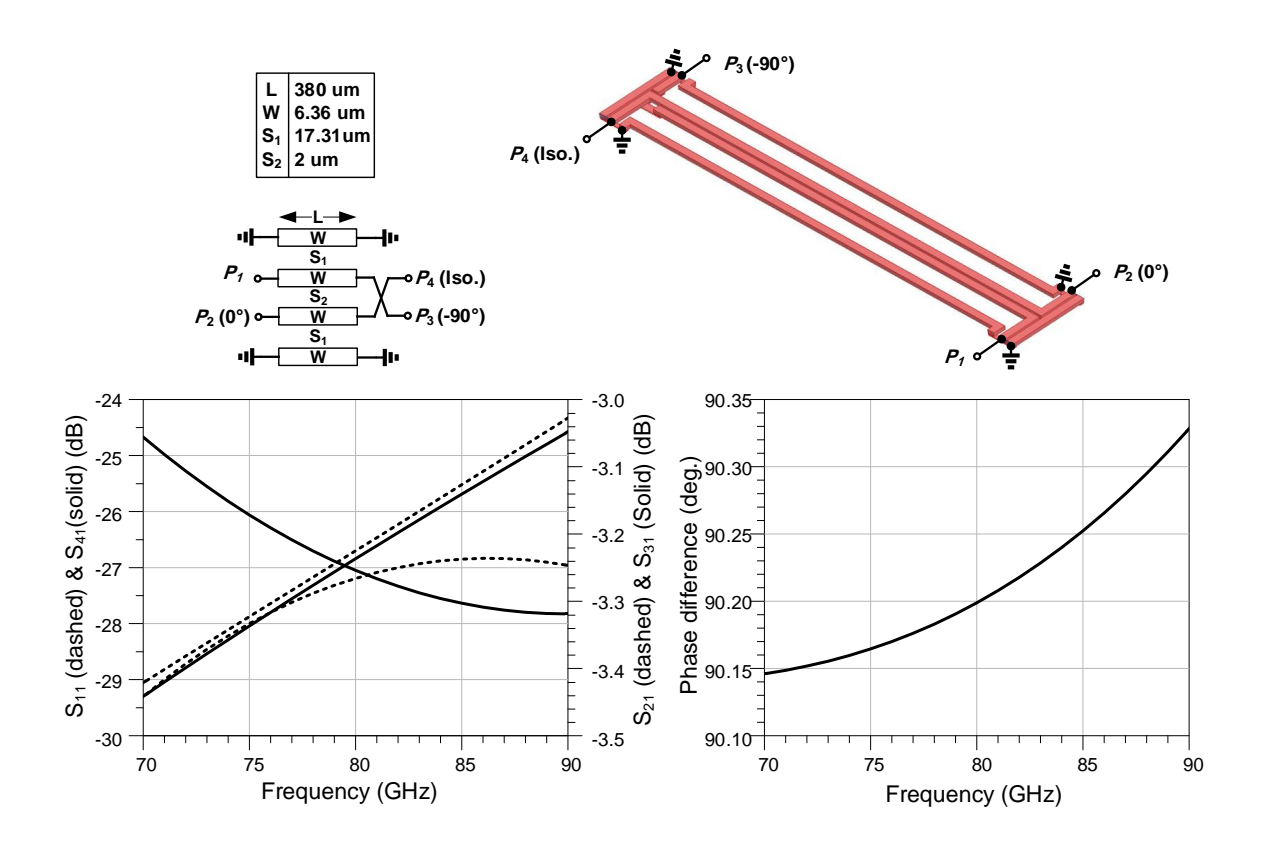


Fig. 5-3. Schematic, layout, and simulation results of the 90° hybrid coupler.

characterization is done for the NMOS transistors. The two important factors, cutoff frequency and transconductance, of the active NMOS are demonstrated separately in Fig. 5-4 and Fig. 5-5. Although the optimum bias for the noise is the main concern of the LNA design at lower frequency bands, its gain is more important at the mm-wave band to suppress the noise contributions of the following lossy passive circuits. Therefore, the optimum bias for the transconductance and cutoff frequency is selected. Based on the simulation curves, the current bias density of 0.35 mA/um is a point that the curves are saturating. This means that burning more current does not effectively improve the performance of the device.

In the next step, the circuit topology should be selected. Single-ended and differential are the two main configurations that should be firstly addressed. While the single-ended topology has the advantages of lower power consumption and smaller layout size, it suffers from the lack of a well-modeled return current path and ground. Specifically, at the mm-wave frequencies, any parasitic resistance and inductance in the ground lines severely

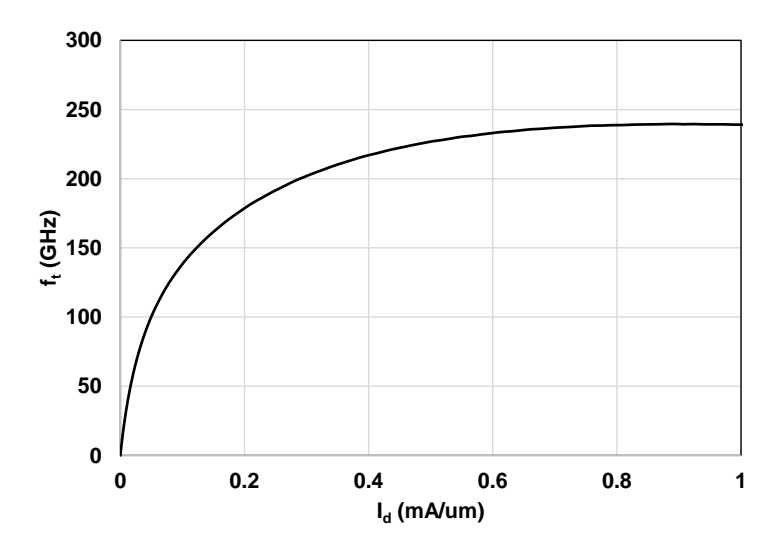


Fig. 5-4. Cutoff frequency (f_t) versus current density of a 10 μ m NMOS transistor.

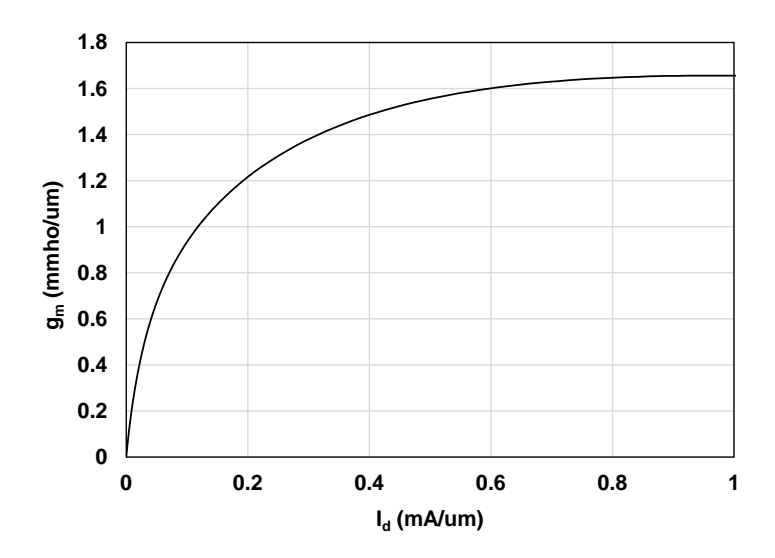


Fig. 5-5. Transconductance (g_m) versus current density of a 10 μ m NMOS transistor.

affect the gain, matching, and stability of the amplifier. In the compound semiconductor technologies such as GaAs, GaN, and InP, the back via connection provides a perfect ground path, which can be easily modeled. However, in bulk CMOS technology, this option is not available. The condition is more complicated when the amplifier is surrounded by other circuits in a big system, affecting the routing of the ground of the amplifier. Moreover, the bonding wires and printed circuit board's (PCB) routing, as external circuits, increase the uncertainty of the high-frequency ground. Therefore, for reducing the risk of the uncertain ground, symmetrical differential topology is more suitable and robust for the high-frequency applications. In addition, the differential circuits bring extra

advantages such as higher dynamic range, immunity to common-mode noises and signals, and making it possible to use cross capacitors to neutralize the unwanted gate-drain capacitors. This improves the stability and frequency response of the circuit, as shown in Fig. 5-6(c). Common-source, cascode, and common-source with neutralization capacitors are the three configurations that are suitable for low noise amplifiers, as shown in Fig. 5-6. The first important factor is the stability of the amplifiers. Fig. 5-7 and Fig. 5-8 show the stability criteria and the minimum NF of the different topologies, respectively, versus frequency. The common-source has the worst stability performance due to the gate-drain feedback capacitor but with the lowest NF because of the simplicity. The cascode, though is unconditionally stable at the band of interest, suffers from additional NF due to the cascode transistor. Moreover, the frequency response of the cascode will be degraded because of the parasitic capacitor at the middle point. A shunt or series inductor is usually required to resonate with the parasitic capacitors in the cascode node at the mm-wave band. As a result, more area is required. In addition, the parasitic capacitor modeling of the standard RF-layouts is more likely valid for the common-source topology. Since the cascode device is a common-gate device, the measurement-based modeling obtained from common-source is not accurate to model the parasitic capacitor of the source. In this work, we have adopted the common-source with the neutralization cross-capacitors, since it has the best performance in terms of the stability and the minimum NF in the entire mm-wave bandwidth.

For designing an LNA with a gain of 20 dB, a minimum of two-stage amplification is required since the maximum stable gain of the active devices at 80 GHz is around 10 dB, as shown in Fig. 5-9. Including the insertion loss of the input, inter-stage, and output matching networks, three stages of gain are required to provide a sufficient gain. The schematic and 3D layout view of a fully differential three-stage LNA with transformer-based coupling is shown in Fig. 5-10(a) and (b), respectively. In this design, the non-symmetrical transformer techniques are employed to increase the degrees of freedom for the matching networks, obtaining a wider frequency response. The simulation results for the LNA in the different corners (TT:50 FF:-40 SS:100) are shown in Fig. 5-11. The LNA is designed

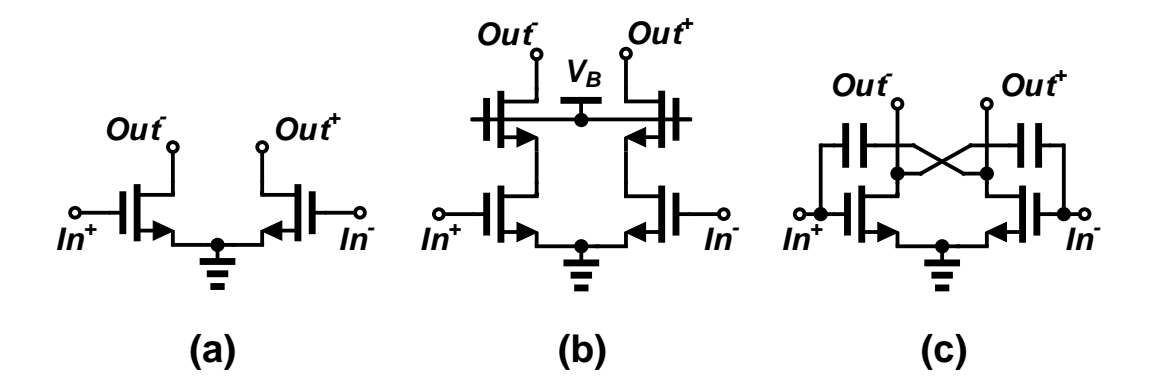


Fig. 5-6. Differential transistor configurations suitable for a high frequency, low noise amplifier design: (a) common source, (b) cascode and (c) common source with neutralization capacitors.

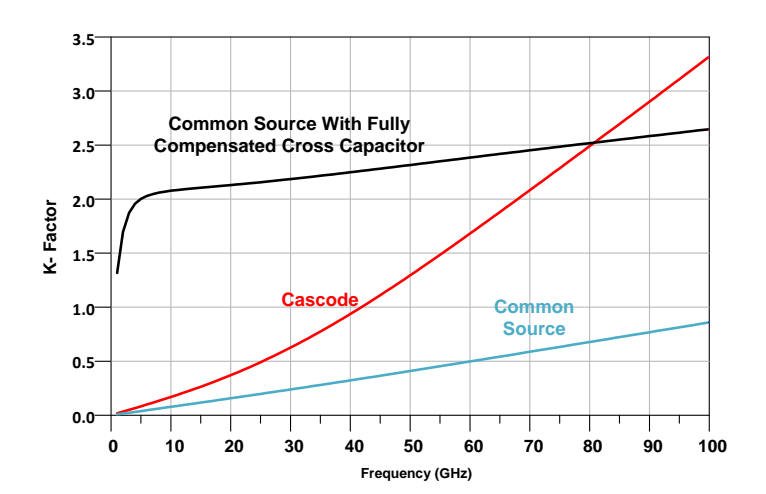


Fig. 5-7. Stability criteria (k-factor) of the standard RF-NMOS transistors versus frequency for different transistor topologies.

to have typically a 20 dB gain in the frequency range of 75-90 GHz. The bandwidth is considerably wide to ensure the frequency response of the LNA can cover any frequency drift after fabrication due to modeling errors and (or) process variations. It is also possible to partially compensate the gain reduction of the SS corner by burning more power. The designed LNA including the surrounding bypass capacitors occupies 730 \times 230 μ m² while draws 20 mA from a 1.2 V supply voltage. The width of the transistors in the first stage is chosen to be wider to obtain the optimum noise impedance closer to 50 Ω , relaxing the matching network design. The cross-capacitors are implemented by metal-oxide-metal

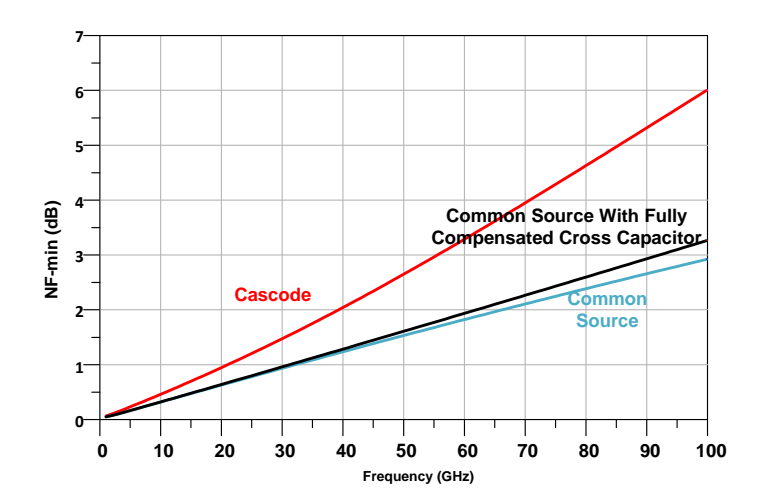


Fig. 5-8. Minimum noise figure versus frequency for a common source, cascode and common source with neutralized gate-drain capacitor configurations.

(MOM) capacitors between metal-6 and metal-7, as shown on the 3D layout view of the input differential pair in Fig. 5-10(c).

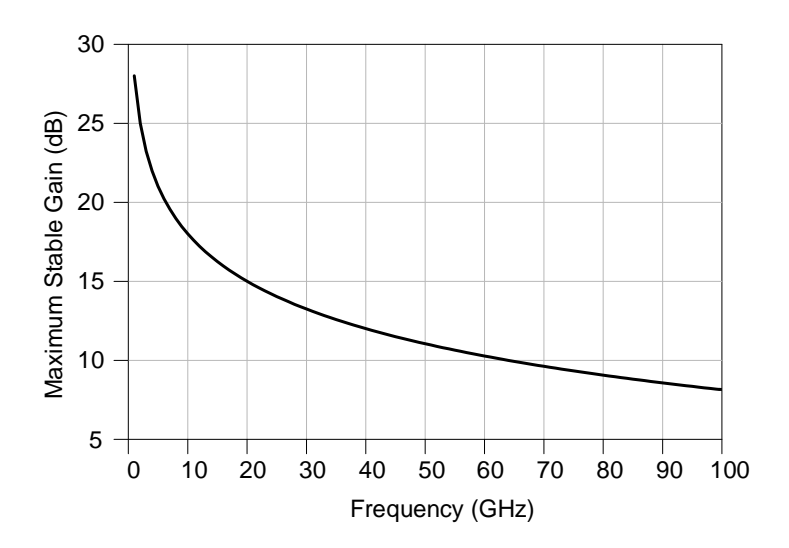


Fig. 5-9. Maximum stable power gain of a minimum length (60-nm) RF NMOS transistor with a width of 10- μ m.

5.4 IQ-demodulator

As discussed in Chapter 4, the IQ-demodulator is the essential part for extracting the radar information and for generating the cancellation signal from the dc offset of the I and Q. Although in general there is no need for the quadrature demodulation for the

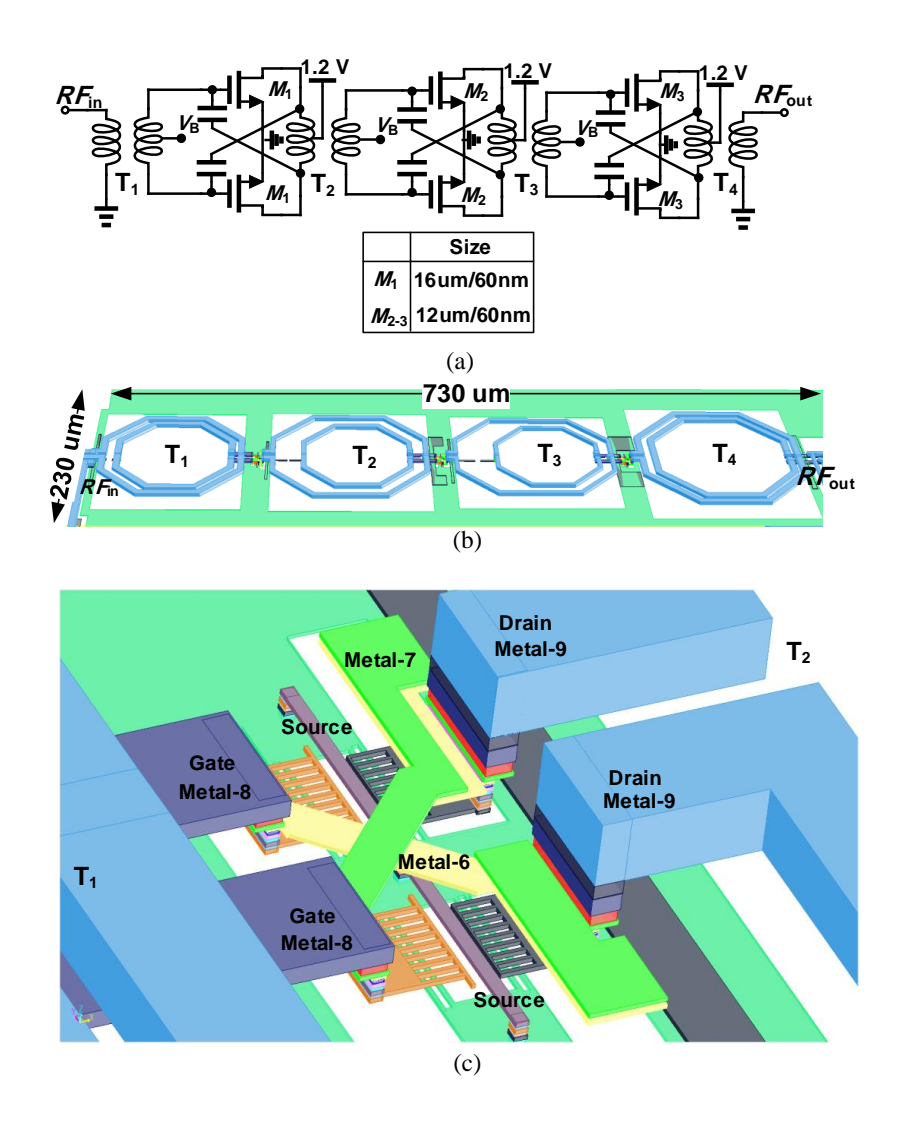


Fig. 5-10. (a) Schematic, and (b) 3D-layout view of a three-stage fully differential transformer-based LNA. (c) 3D layout of the differential pair, including the cross-capacitors

FMCW radars, the quadrature processing reduces the single-sideband (SSB) NF of the down-converter by 3 dB. Therefore, using the IQ-demodulator should not be considered as extra overhead for the single-antenna architecture.

The RF and LO path quadrature generation are the two main approaches to build the IQ-downconvert mixer, as shown in Fig. 5-12. Polyphase filters (PPFs) using R-C C-R ladders are commonly used in the lower frequencies to generate the LO path quadrature signals within a small area. Since the LO signal has a big amplitude, using the lossy passive PPF is not a concern for the low-frequency applications. However, this approach is not appropriate for the RF path quadrature generation due to extra loss and NF

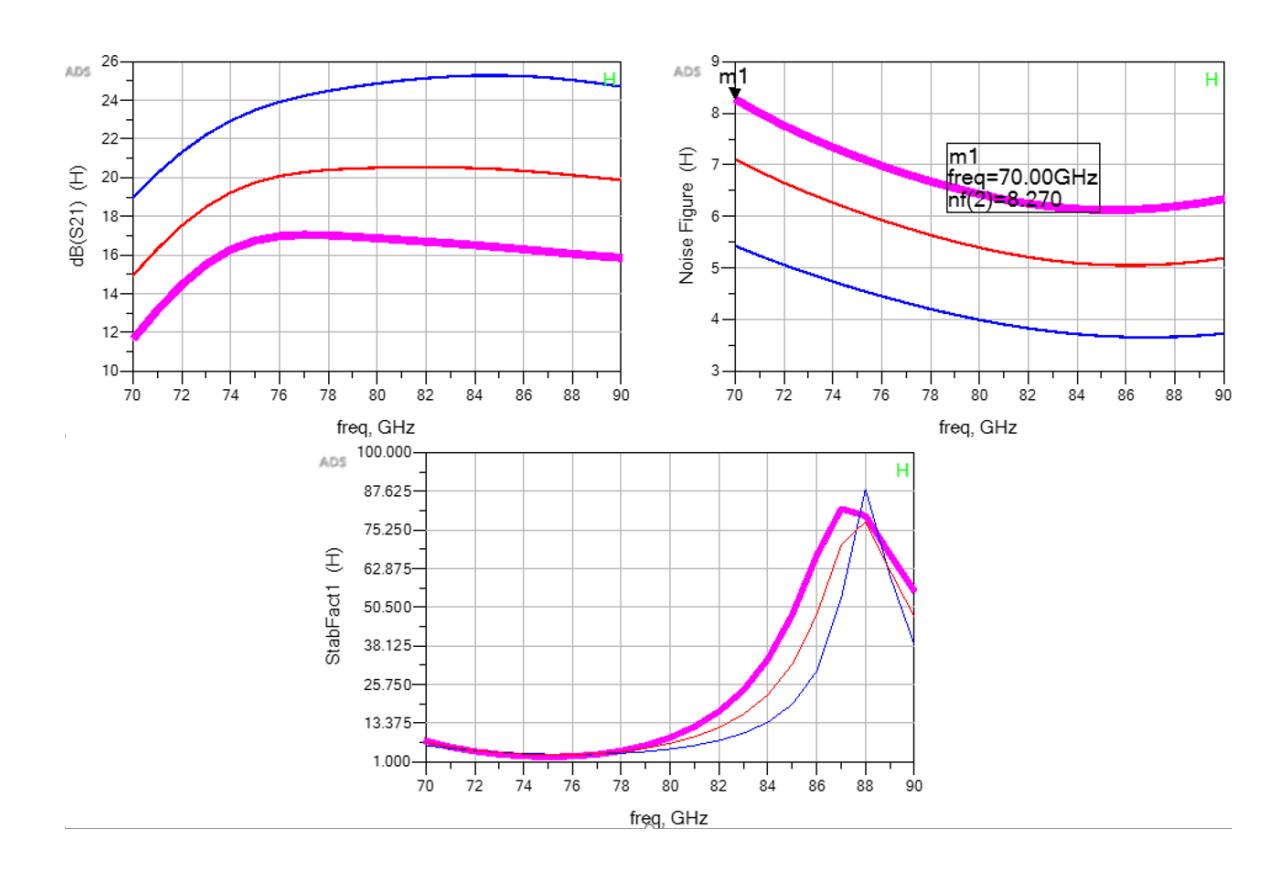


Fig. 5-11. Simulated Gain, NF and Stability factor for the LNA in different corners.

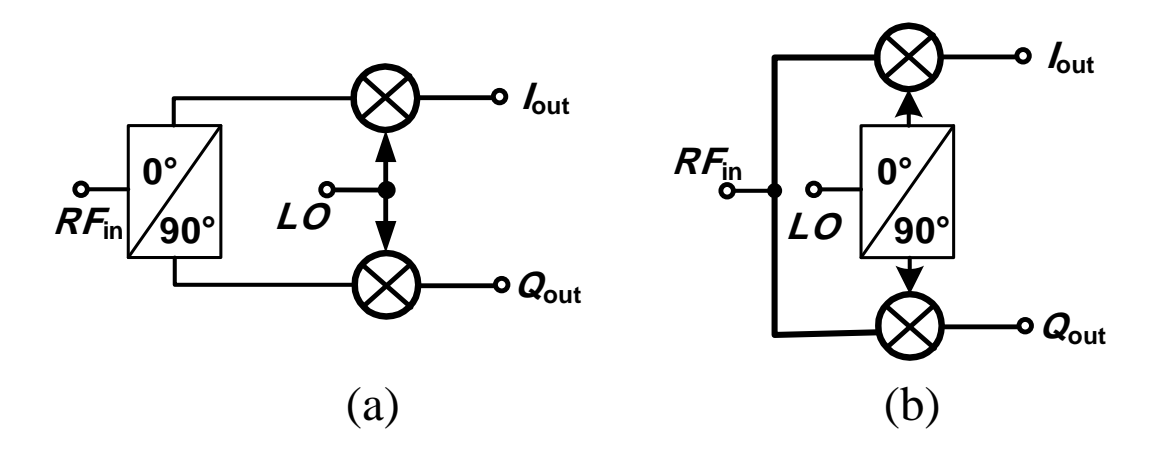


Fig. 5-12. IQ-demodulation using (a) RF path quadrature generation, and (b) LO path quadrature generation.

degradation. On the other hand, PPF is not an optimum solution at the mm-wave band because of the loss. The amplification cost and extra passive loss at the mm-wave band do not allow for any extra systematic loss. Therefore, passive loss-less solutions, such as quadrature couplers, are the optimum solution at the mm-wave band. Among different

quadrature techniques, the RF path quadrature generation using a 90° hybrid coupler is adopted in this work, as shown in Fig. 5-13. Using the 90° hybrid in the RF path has three benefits. First, it splits the RF power between the two mixers. Second, it creates isolation between I and Q paths, avoiding noise coupling between I and Q mixers, which improves the sensitivity. And third, the RF input impedance of the IQ-demodulator is matched to 50 Ω regardless of the impedance of the mixers thanks to the balance structure [64]. Having a 50 Ω matching between the LNA and mixer though is not essential inside a chip at lower RF frequencies, helps to reuse the LNA and mixer blocks separately and also reduces the design complexity and co-optimization overheads at the mm-wave band. Moreover, the frequency response and stability of the LNA will be well-defined when the well-known load impedance is connected to the circuit.

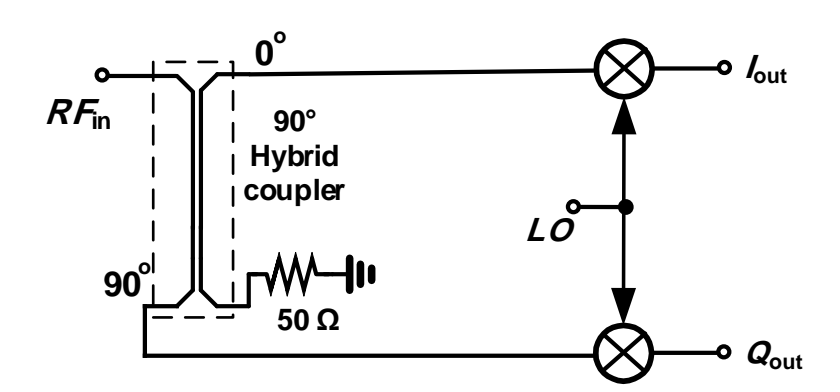


Fig. 5-13. RF path quadrature generation using a 90° hybrid coupler for the IQ-demodulator.

The schematic of the IQ demodulator is shown in Fig. 5-14. The single-balanced passive mixers followed by transimpedance amplifiers (TIAs) are employed for the down-converter mixers due to better linearity and noise performance. The upper side mixing products are filtered out using C_{LP} and the input capacitance of the TIA. The LO port is coupled through a matching transformer to the gates of the switches. The gates (V_g) are biased at the edge of the threshold voltage of the transistors to reduce the required LO amplitude for a good switching. Two-stage fully-differential operational amplifiers with resistive feedbacks are used for the TIAs. The TIAs draw 2 mA from a 1.2 V supply

voltage.

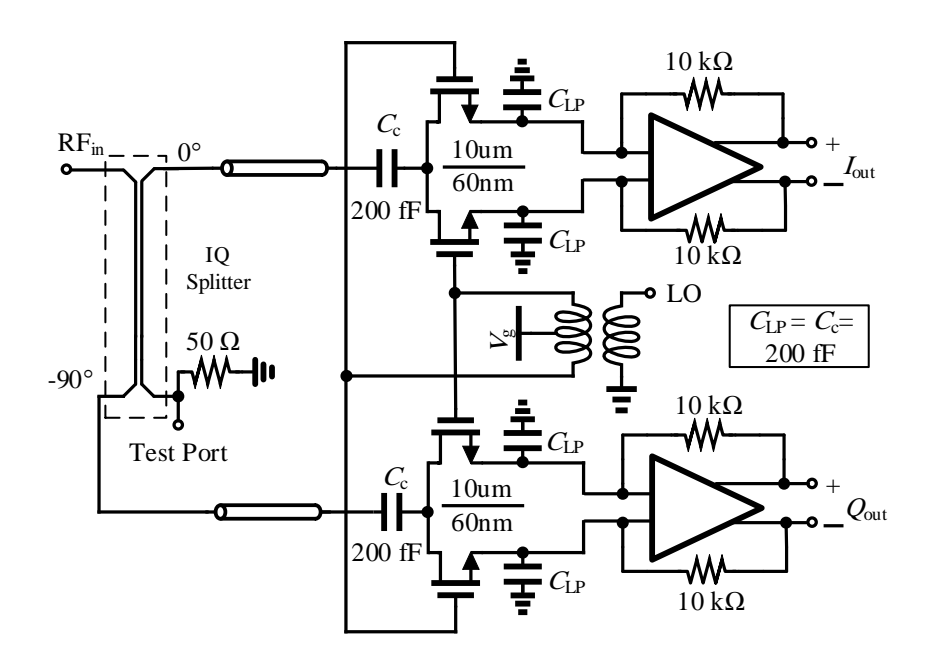


Fig. 5-14. Schematic of the IQ demodulator.

The simulated conversion gain and SSB NF, and IQ-imbalance of the IQ-demodulator, including 90° coupler and TIAs, are shown in Fig. 5-15(a) and (b), respectively. The simulation shows a gain of 24 dB with an SSB NF of 20 dB at the baseband frequency of 100 kHz.

5.5 Phase compensator

The phase compensator (PC) is implemented using a current-mode vector weighting circuit, as shown in Fig. 5-16. The variable Gm cells convert the differential input I and Q signals to the single-ended output currents, which are integrated using the shunt off-chip capacitors, forming the loop filter of the architecture. Using the circuit, the IQ-plan maps to the new I'Q'-plan, where shown in Fig. 4-17. The high gain characteristic of the integrator at dc (ideally infinity), increases the loop gain, thereby improving the CF in (4.23).

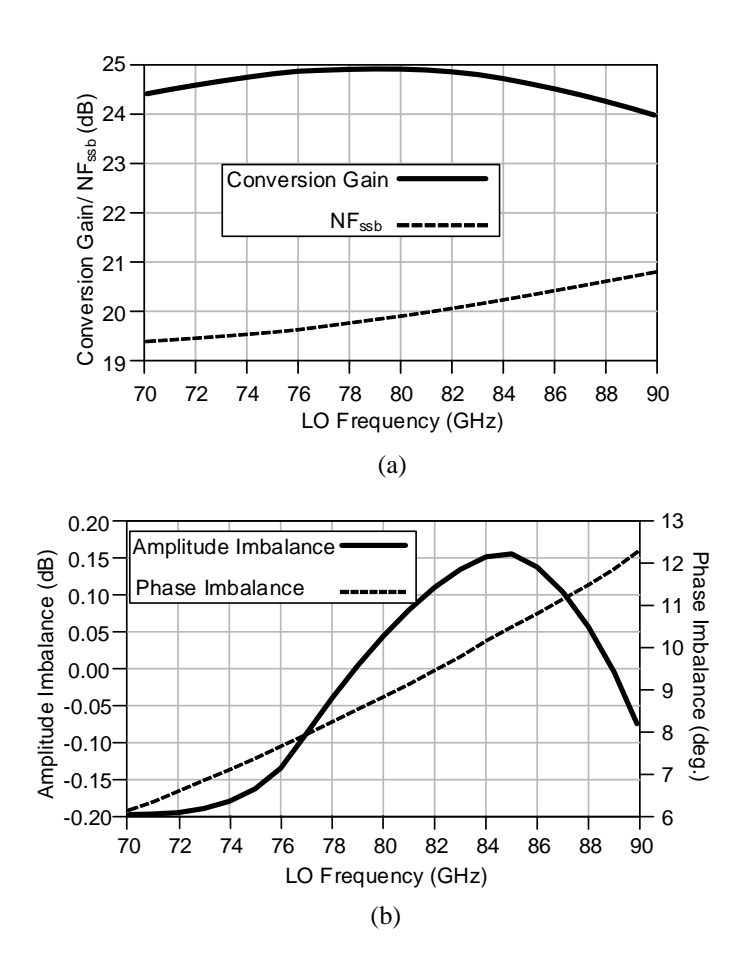


Fig. 5-15. Simulated (a) conversion gain and NF, and (b) IQ-imbalance of the IQ-demodulator.

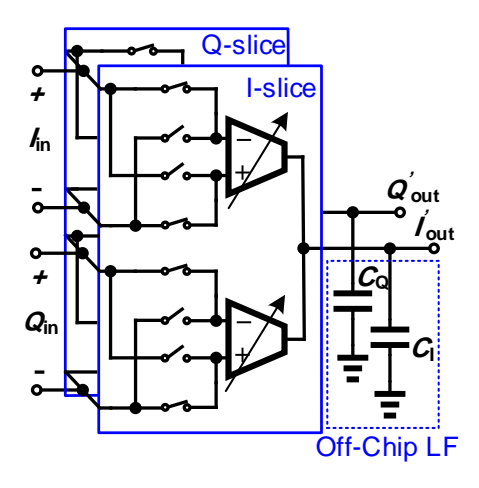


Fig. 5-16. Block diagram of the phase compensator.

5.6 Variable reflector (VR)

In Chapter 4, a new cancellation scheme was proposed to solve the issues associated with the IQ-modulator-based leakage canceller. The key building block for the proposed idea is

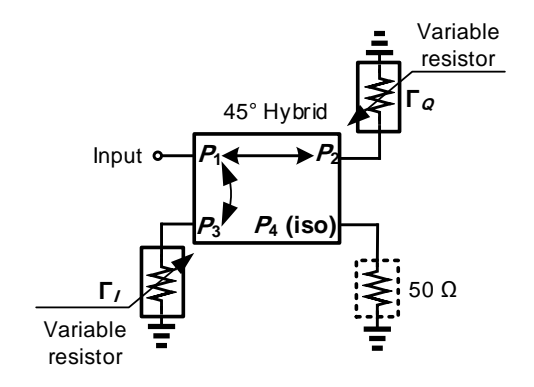


Fig. 5-17. Schematic of the proposed VR.

a controllable reflection coefficient that reflects the power of the TX with an appropriate amplitude and phase. It has been shown that a VR with two orthogonal parameters is required for controlling the real and imaginary parts of its reflection coefficient separately. Our proposed circuit shown in Fig. 5-17 can provide the unique characteristic [65]. The introduced VR consists of a 45° coupler and two variable resistors (Γ_I and Γ_Q). The S-parameter of the 45° hybrid coupler is

$$[S] = \frac{\sqrt{2}}{2} \begin{pmatrix} 0 & 1\angle - 45^{\circ} & 1\angle - 90^{\circ} & 0\\ 1\angle - 45^{\circ} & 0 & 0 & 1\angle - 90^{\circ}\\ 1\angle - 90^{\circ} & 0 & 0 & 1\angle 45^{\circ}\\ 0 & 1\angle - 90^{\circ} & 1\angle 45^{\circ} & 0 \end{pmatrix}.$$
 (5.1)

The input reflection coefficient of the proposed circuit can be calculated by the following equations.

$$V_{1}^{-} = S_{12}V_{2}^{+} + S_{13}V_{3}^{+}$$

$$V_{2}^{-} = S_{21}V_{1}^{+} + S_{24}V_{4}^{+}$$

$$V_{3}^{-} = S_{31}V_{1}^{+} + S_{34}V_{4}^{+}$$

$$V_{4}^{-} = S_{42}V_{2}^{+} + S_{43}V_{3}^{+}$$

$$V_{2}^{+} = \Gamma_{Q}V_{2}^{-}$$

$$V_{3}^{+} = \Gamma_{I}V_{3}^{-}$$

$$V_{4}^{+} = 0$$

$$(5.2)$$

where V_i^+ and V_i^- is the incident and reflected voltage, respectively, of the i_{th} port, and S_{ij} is the i_{th} and j_{th} element of the scatter matrix in (5.2). Solving the above equations yields

$$\Gamma_{in} = \frac{V_1^-}{V_1^+} = -\frac{1}{2}\Gamma_I - j\frac{1}{2}\Gamma_Q. \tag{5.3}$$

It can be seen from (5.3) that the real and imaginary parts of the input reflection coefficient can be controlled independently using only two variable resistors. The coverage area of the input reflection coefficient of the VR on the Smith chart is shown in Fig. 5-18 when Γ_I and Γ_Q vary from -1 to 1, corresponding to the resistance variation from 0 Ω to ∞ Ω . The proposed VR ideally can cover a reflection coefficient circle centered at the origin of the Smith chart with a radius of 0.5 using the two variable resistors.

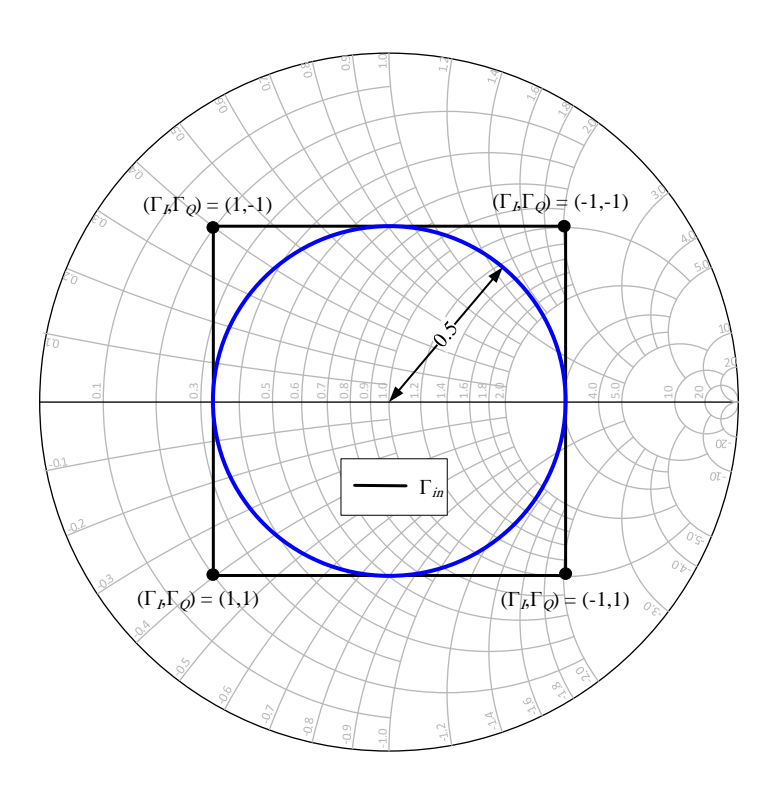


Fig. 5-18. Coverage area of the input reflection coefficient of the VR on the Smith chart.

In [65], we also proposed a wideband circuit topology for implementing the VR and hybrid 45° circuit. While 90° and 180° planar hybrid couplers are well-developed microwave circuits [66–72], the other types of hybrids are not studied very well because of the limited number of applications. To implement the 45° hybrid coupler, we introduce a new wideband hybrid coupler topology with arbitrary phase and amplitude, as a partial

achievement of this thesis.

5.6.1 Proposed arbitrary phase and amplitude hybrid coupler

In this subsection, we propose a single section planar hybrid coupler with arbitrary phase and amplitude based on a coupled-line topology. The schematic of the proposed hybrid circuit is illustrated in Fig. 5-19. The proposed topology can achieve a fractional bandwidth of 50% for an equal power splitting 45° hybrid thanks to using the combination of the coupled-line structures with lumped components.

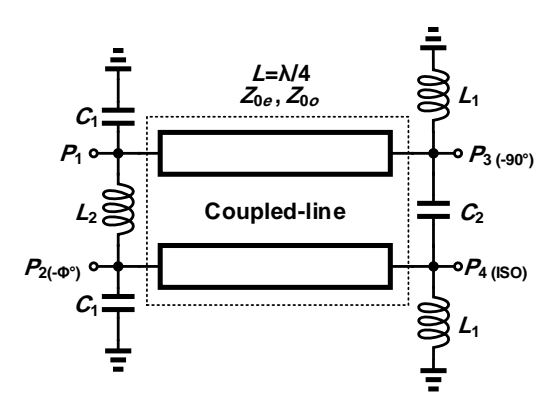


Fig. 5-19. Proposed schematic of a hybrid coupler with arbitrary phase and amplitude.

The equivalent circuit model for even-odd mode analysis [73] is shown in Fig. 5-20. The first critical equations are the equations referring to the input matching and isolation between P_1 and P_4 in Fig. 5-19. From even-odd mode theory, S_{11} and S_{41} can be calculated by

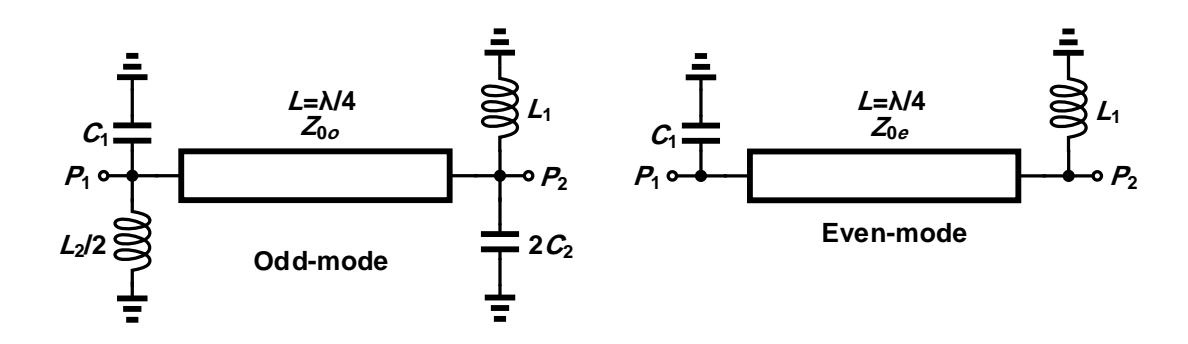


Fig. 5-20. Equivalent circuit model for even-odd mode analysis.

$$S_{11} = \frac{1}{2}(S_{11,even} + S_{11,odd}) = 0$$
 (5.4a)

$$S_{41} = \frac{1}{2}(S_{21,even} - S_{21,odd}) = 0, \tag{5.4b}$$

where $S_{ij,even}$ and $S_{ij,odd}$ is the S-parameter of the equivalent even- and odd-mode circuits, respectively, shown in Fig. 5-20. Expanding the real and imaginary parts of (5.4) results in

$$\frac{1}{\Re\{S_{11,even}\}} = -\frac{1}{\Re\{S_{11,odd}\}}$$
 (5.5a)

$$\frac{1}{\Im\{S_{11,even}\}} = -\frac{1}{\Im\{S_{11,odd}\}} \tag{5.5b}$$

$$\Re\{\frac{1}{S_{21,even}}\} = \Re\{\frac{1}{S_{21,odd}}\}\tag{5.5c}$$

$$\Im\{\frac{1}{S_{21,even}}\} = \Im\{\frac{1}{S_{21,odd}}\},\tag{5.5d}$$

where \Re and \Im stands for real and imaginary, respectively. The toggling between the \Re/\Im operators and inversion adopted in (5.5) simplify the equations for the next calculations. Analyzing the circuit for (5.5c) yields

$$\frac{1 - C_1 L_1 \omega_0^2}{2Z_{0o} L_1 \omega_0} = \frac{L_2 (1 - C_1 L_1 \omega_0^2) + 2L_1 (1 - C_2 L_2 \omega_0^2)}{2Z_{0e} L_1 L_2 \omega_0},$$
(5.6)

where $L_{1,2}$ and $C_{1,2}$ are the values of the inductors and capacitors, respectively, in Fig. 5-20, Z_{0e} and Z_{0o} represents the characteristic impedance of the coupled-line in even- and odd-mode excitation, respectively, and ω_0 is the center frequency. Resonating L_1 with C_1 and L_2 with C_2 at ω_0 is the solution of (5.6):

$$L_1C_1 = L_2C_2 = \frac{1}{\omega_0^2}. (5.7)$$

Substituting L_1 and L_2 from (5.7) into (5.5d) and (5.5b) results in

$$\frac{C_1^2 Z_0^2 Z_{0e}^2 \omega_0^2 + Z_0^2 + Z_{0e}^2}{(C_1 - 2C_2)^2 Z_0^2 Z_{0o}^2 \omega_0^2 + Z_0^2 + Z_{0o}^2} = \frac{Z_{0e}^2 C_1}{Z_{0o}^2 (2C_2 - C_1)}$$
(5.8)

$$\frac{C_1^2 Z_0^2 Z_{0e}^2 \omega_0^2 + Z_0^2 + Z_{0e}^2}{(C_1 - 2C_2)^2 Z_0^2 Z_{0e}^2 \omega_0^2 + Z_0^2 + Z_{0e}^2} = \frac{Z_{0e}}{Z_{0o}},$$
(5.9)

where $Z_0 = 50 \ \Omega$ is the reference impedance. Equating the right sides of (5.8) and (5.9) gives

$$\frac{Z_{0o}}{Z_{0e}} = \frac{C_1}{2C_2 - C_1}. (5.10)$$

Using C_2 from (5.10), even- and odd-mode S-parameters can be calculated by the following equations:

$$S_{21,even} = -j \frac{2Z_0 Z_{0e}}{C_1^2 Z_0^2 Z_{0e}^2 \omega_0^2 + Z_{0e}^2 + Z_0^2}$$

$$S_{21,odd} = -j \frac{2Z_0 Z_{0o}}{C_1^2 Z_0^2 Z_{0e}^2 \omega_0^2 + Z_{0o}^2 + Z_0^2}$$

$$(5.11a)$$

$$S_{21,odd} = -j \frac{2Z_0 Z_{0o}}{C_1^2 Z_0^2 Z_{0e}^2 \omega_0^2 + Z_{0o}^2 + Z_0^2}$$
(5.11b)

$$S_{11,even} = -1 + jS_{21,even} \frac{Z_{0e}}{Z_0} + C_1 Z_{0e} \omega_0 S_{21,even}$$
(5.11c)

$$S_{11,odd} = -1 + jS_{21,odd} \frac{Z_{0o}}{Z_0} - C_1 Z_{0e} \omega_0 S_{21,odd}.$$
 (5.11d)

The next important equations are related to the amplitude and phase response of the coupler. S_{21} and S_{31} of the hybrid circuit with arbitrary amplitude and phase can be calculated as functions of even-odd mode S-parameters by the following equations:

$$S_{21} = \frac{1}{2} (S_{11,even} - S_{11,odd}) = Ke^{-j(\pi/2 - \Delta\Phi)}$$
 (5.12a)

$$S_{31} = \frac{1}{2}(S_{21,even} + S_{21,odd}) = -j\sqrt{1 - K^2},$$
(5.12b)

where 0 < K < 1 is the desired coupling coefficient $(K = \sqrt{2}/2 \text{ for equal power splitting})$ and $\Delta\Phi$ is the desired output phase difference between P_2 and P_3 . Substituting (5.11c) and (5.11d) into (5.12a) and noting that $S_{21,even}$ and $S_{21,odd}$ are purely imaginary, the real and imaginary parts of S_{21} can be rewritten as functions of $S_{21,even}$ and $S_{21,odd}$, as (5.13a) and (5.13b), respectively:

$$j\frac{1}{2}\left(S_{21,even}\frac{Z_{0e}}{Z_0} - S_{21,odd}\frac{Z_{0o}}{Z_0}\right) = K\sin\Delta\Phi \tag{5.13a}$$

$$-j\frac{1}{2}C_1Z_{0e}\omega_0(S_{21,even} + S_{21,odd}) = -K\cos\Delta\Phi.$$
 (5.13b)

Dividing (5.12b) by (5.13b) yields

$$C_1 = \frac{K\cos\Delta\Phi}{\sqrt{1 - K^2}Z_{0e}\omega_0}. (5.14)$$

Substituting (5.14), (5.11a) and (5.11b) into (5.4b) yields

$$(Z_{0o}Z_{0e}(1-K^2) - (1-K^2 + K^2\cos^2\Delta\Phi) Z_0^2) \times$$

$$(Z_{0o} - Z_{0e})(1-K^2) = 0. \quad (5.15)$$

The acceptable solution to the above equation is

$$Z_{0o}Z_{0e} = \left(1 + \frac{K^2}{1 - K^2}\cos^2 \Delta\Phi\right)Z_0^2.$$
 (5.16)

Substituting (5.16), (5.14), (5.11a) and (5.11b) into (5.13a), Z_{0o} can be calculated by

$$\frac{Z_0^2 \left(1 + \frac{K^2}{1 - K^2} \cos^2 \Delta \Phi\right) - Z_{0o}^2}{Z_0^2 \left(1 + \frac{K^2}{1 - K^2} \cos^2 \Delta \Phi\right) + Z_{0o}^2} = K \sin \Delta \Phi \Rightarrow
Z_{0o} = Z_0 \sqrt{\left(1 + \frac{K^2}{1 - K^2} \cos^2 \Delta \Phi\right) \frac{1 - K \sin \Delta \Phi}{1 + K \sin \Delta \Phi}}. (5.17)$$

Table 5.1 summarizes the closed-form equations required to design an arbitrary phase and coupling coefficient hybrid coupler using the proposed circuit topology. The output phase difference ($\Delta\Phi$), coupling coefficient (K), center frequency (ω_0) and reference impedance (Z_0) are the inputs of the equations, and parameters of the components can be obtained one by one by calculating the equations in the same order as arranged in the table. The calculated values of the components for an equal power splitting hybrid coupler ($K = \sqrt{2}/2$) with a 45° phase difference ($\Delta\Phi = 45$ °) at 80 GHz, as the core component of the proposed VR, is also included in Table 5.1. The S-parameter simulation results of the proposed circuit are plotted in Fig. 5-21. Within a phase and amplitude error of less than ± 5 ° and 1 dB, a fractional bandwidth of 60% is achieved for the 45° hybrid coupler.

Table 5.1: List of equations and values of the components for the proposed hybrid coupler with arbitrary phase and amplitude.

Eq. No. Pa	Parameter	Equation	45° Hybrid	
	1 arameter		$K = \sqrt{2}/2 \& \Delta \Phi = 45^{\circ} @ 80 \text{ GHz}$	
(5.17)	Z_{0o}	$Z_0\sqrt{\left(1+\frac{K^2}{1-K^2}\cos^2\Delta\Phi\right)\frac{1-K\sin\Delta\Phi}{1+K\sin\Delta\Phi}}$	$35.35~\Omega$	
(5.16)	Z_{0e}	$\left(1 + \frac{K^2}{1 - K^2} \cos^2 \Delta \Phi\right) \frac{Z_0^2}{Z_{0o}}$	106.06 Ω	
(5.14)	C_1	$\frac{K\cos\Delta\Phi}{\sqrt{1-K^2}Z_{0e}\omega_0}$	13.3 fF	
(5.10)	C_2	$\left(\frac{Z_{0e}}{Z_{0o}}+1\right)\frac{C_1}{2}$	26.6 fF	
(5.7)	L_1	$rac{1}{\omega_0^2 C_1}$	298 pH	
(5.7)	L_2	$rac{1}{\omega_0^2 C_2}$	149 pH	

5.6.2 Proposed VR

Based on the introduced circuit, a VR is optimized with the CPW-based coupled line structure, on-chip spiral inductors, and MOM-capacitors at 80 GHz, as shown in Fig. 5-22. M_1 and M_2 are biased in the triode region and are employed as the variable resistors. The parasitic capacitors of M_1 are absorbed by the intrinsic capacitor of the 45° hybrid coupler (i.e., C_1 in Fig. 5-19). The inductance of L_1 is also reduced to compensate for the parasitic capacitors of M_2 . The layout only occupies $283 \times 158 \ \mu\text{m}^2$ at W-band.

The simulated input impedance coverage of the proposed VR is plotted on the Smith chart in Fig. 5-22 when the two control voltages (I_{ctrl} and Q_{ctrl}) are swept from 0 to 1.2 V. It can be seen that the circuit level simulation of the coverage area deviates from the ideal simulations in two ways. First, the coverage area is shrunken due to the higher insertion loss of the 45° hybrid coupler. Γ_I and Γ_Q implemented by triode transistors M_1 and M_2 cannot provide a full range variation from -1 to +1, which further reduces the coverage of the input reflection coefficient. Second, the shape of the square is deformed and rotated. The rotation is equivalent to a phase offset in the loop, which can be compensated by the PC circuit. The deformation of the shape of the square can be modeled as IQ-imbalance in the loop. As was proven in Chapter 4.3.3, the proposed feedback canceller is robust

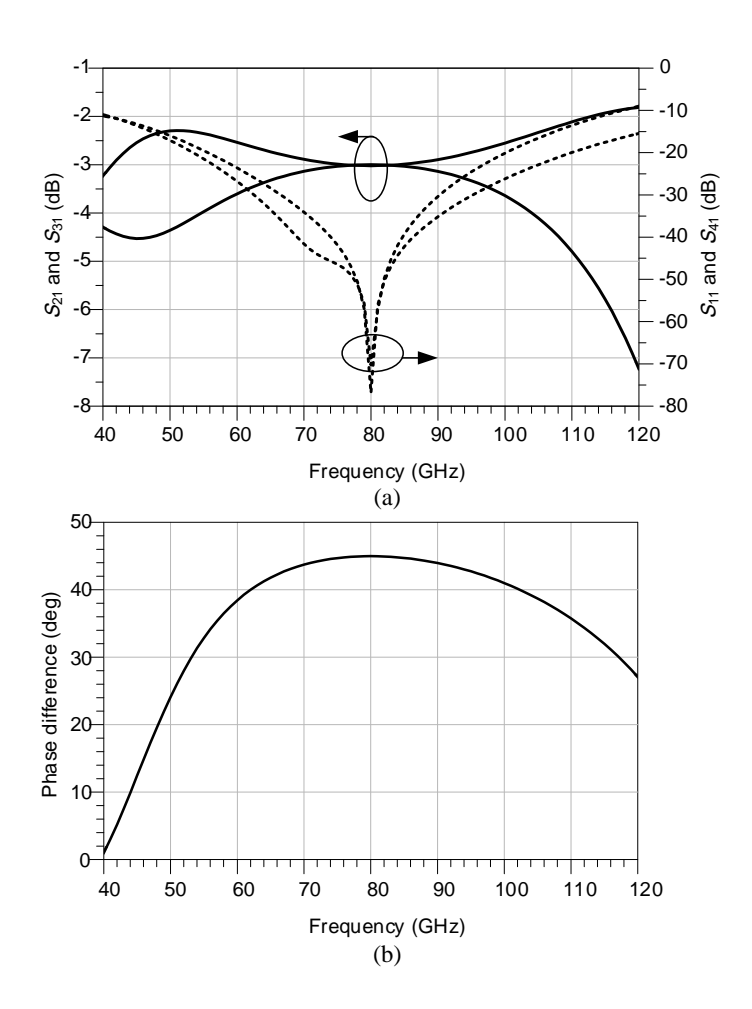


Fig. 5-21. (a) Simulated S-parameters of the proposed 45° hybrid coupler. (a) Amplitude response. (b) Phase response.

against the IQ-imbalances.

5.7 TX block

The schematic of the TX block, including TX amplifiers, LO distribution path for the IQ-demodulator, and the antenna coupler, is shown in Fig. 5-23. The main TX block consists of an injection locked frequency tripler (ILFT) followed by a two-stage differential amplifier to generate an output power of 9 dBm at 80 GHz. The ILFT has 4 bits to control the free-running oscillation frequency from 78-82 GHz. M_1 and M'_1 are the injection transistors, biased in class-C to generate a third harmonic. Based on the simulation results, the locking range is 700 MHz around the free-running oscillation frequency. The frequency step of 500 MHz is designed to provide a 200 MHz overlap. The simulation

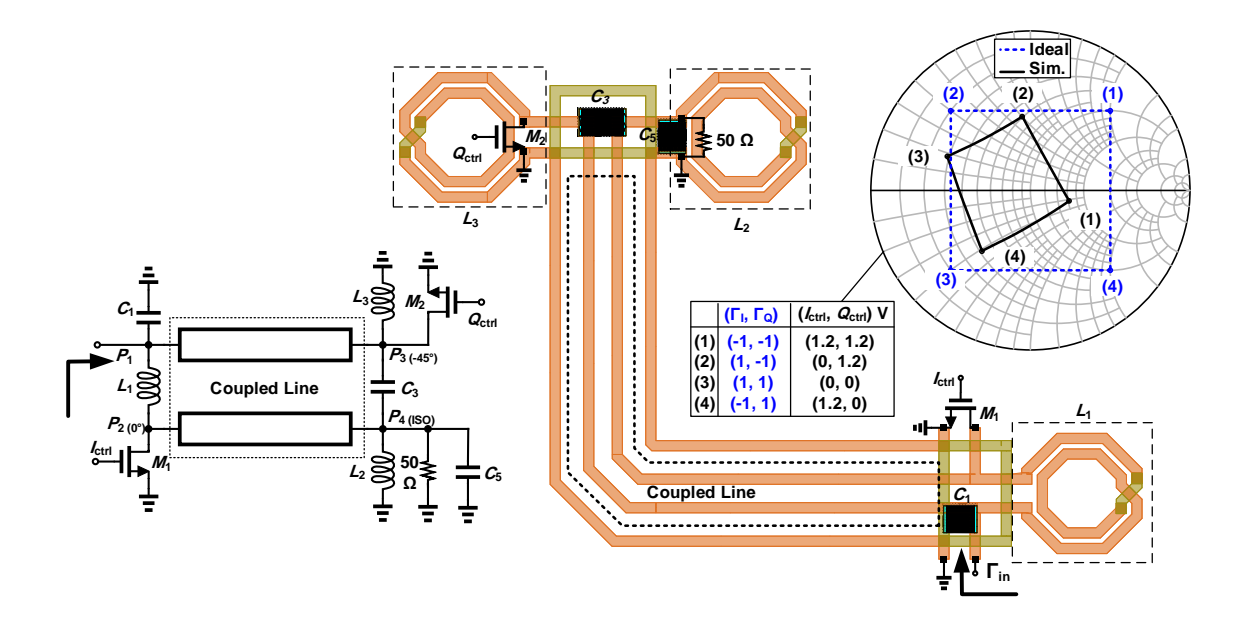


Fig. 5-22. Schematic and layout of the proposed VR circuit at 80 GHz.

result of the frequency coverage of the TX versus digital code of the controlling bits is illustrated in Fig. 5-24. Using the ILFT facilitates applying an external signal source at a frequency of one-third (26.6 GHz) using conventional PCBs and bonding wire interface. The output power of the amplifier then drives the IQ-modulator LO port through a 6 dB coupler and then goes to the antenna port through the antenna coupler. The chip output power of 2 dBm is achieved in the simulation after subtracting the loss of the couplers. The power assigned for the IQ-demodulator is enough to derive the LO port without needing an active buffer, which maximizes the PN correlation and the PN attenuation in the down-conversion process.

5.8 TRX simulations

In this section, the complete front-end simulation results are demonstrated. The layout floor plan of the chip is shown in Fig. 5-25. The die area of the chip, including the IO pads, is 1 mm² (1 mm×1 mm) and in total the chip draws 94 mA from a 1.2 V supply voltage (113 mW). The supply voltages and their current consumption, number of analog pads and digital I/O pads are listed in Table 5.2, Table 5.3 and Table 5.4, respectively.

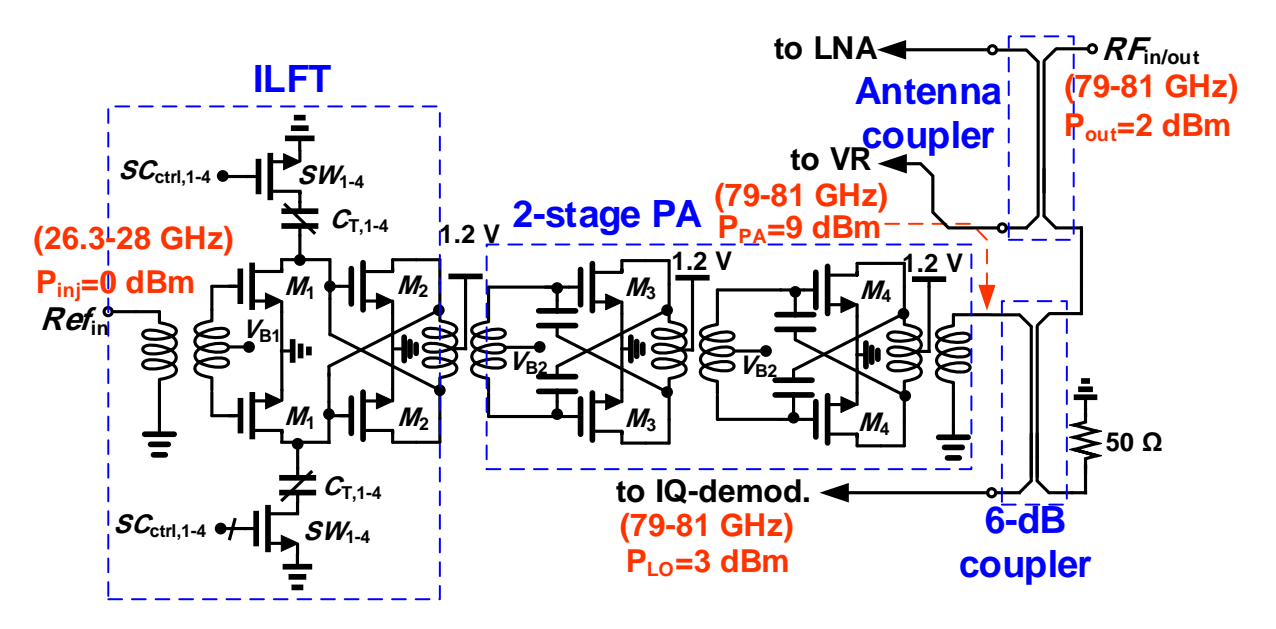


Fig. 5-23. Schematic of the transmitter.

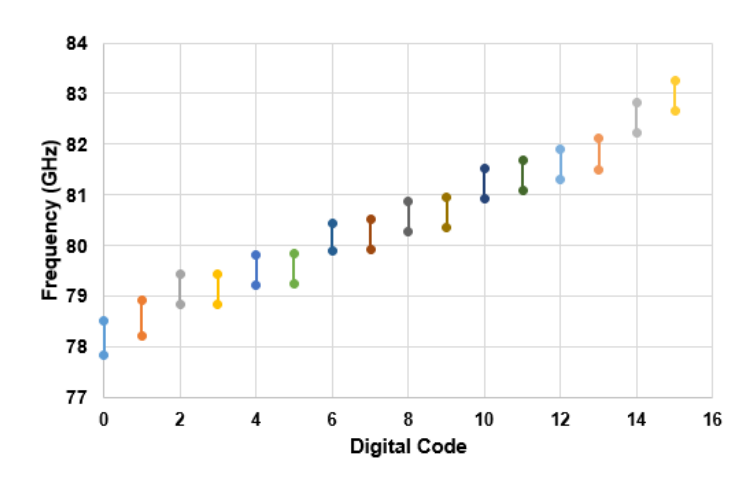


Fig. 5-24. Simulated locking range of the ILFT versus controlling digital bits.

Table 5.2: Supply voltages and current consumption of the chip

Supply						
Name	Voltage (V)	Current (mA)	Power (mW)	Description		
VDD_TX		70	84			
VDD_LNA	1.2	20	24	$ brace 60 ext{x}60 ext{ w/ESD}$		
VDD_BB		4	4.8			
Total Power=112.8 mW						

In the all of simulations, both the TX and RX are working simultaneously and the PN of the input reference signal is also included. The whole passive structures of the

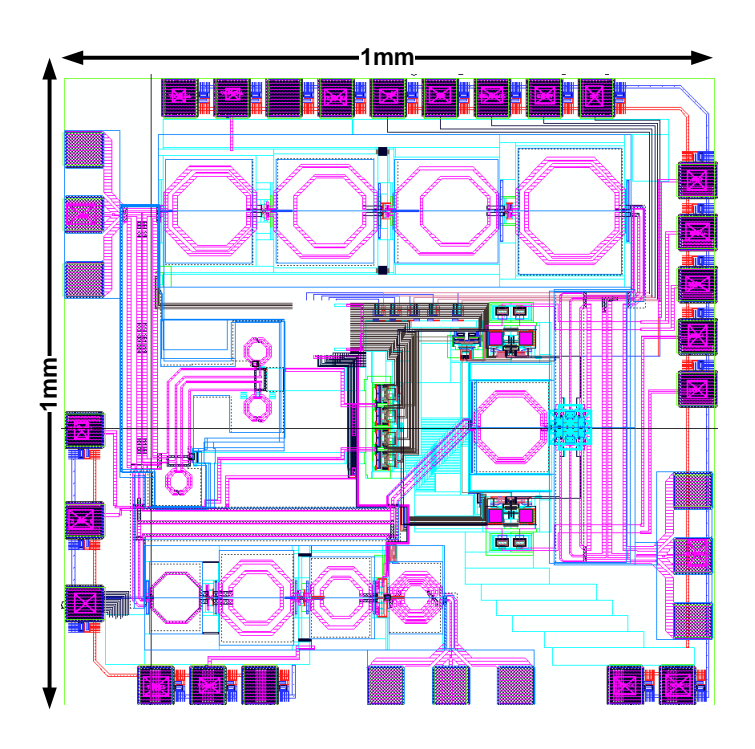


Fig. 5-25. The layout of the chip.

Table 5.3: Number of pads and types

Type	Name	# of Pads	Description	Summary	
	Antenna		60x60 wo/ESD	Type	# of Pads
GSG	TF-Test	3		RF	9
	Reference			Baseband	9
Baseband	CapFB1:2	2		Digital	5
	I & Q Output 4		$60\mathrm{x}60~\mathrm{w/ESD}$	Supply	3
	Gate Voltage	2		VSS	5
	Ref Current	1		Total	29

TRX are EM-simulated to model all of the TX to RX leakages, including the substrate leakages. Unlike normal communication RXs, which should meet nonlinearity specs (IP3 and 1dB CP), in this work, the RX should maintain acceptable NF and gain performance in the presence of a huge TX leakage signal. The simulated conversion gain and SSB NF of the RX versus the baseband frequency offset at an LO frequency of 80 GHz are plotted in Fig. 5-26. A simulated NF of 13.5 dB is obtained for a frequency offset of greater

Table 5.4: Digital pads

Digital					
Pin name	Voltage (V)	Current (mA)	Description		
clk					
din					
dout	1.2	-	60x60 w/ESD		
set					
reset					

than 100 kHz. As predicted by (4.22), the closed-loop operation provides a cancellation characteristic at the input of the LNA, which adaptively rejects the leakage signals with lower frequency offsets, as shown in the simulated RX conversion gain in Fig. 5-26. From the curve, the loop rejects the leakage signals by 40 dB at the input of the LNA. Adding 15 dB of the intrinsic isolation of the antenna coupler, a total isolation of 55 dB has been obtained between the TX and RX thanks to the proposed leakage cancellation scheme. The first-order high-pass characteristic of the conversion gain equalizes the received signal power versus the range, resulting in a dynamic range enhancement for the FMCW radars.

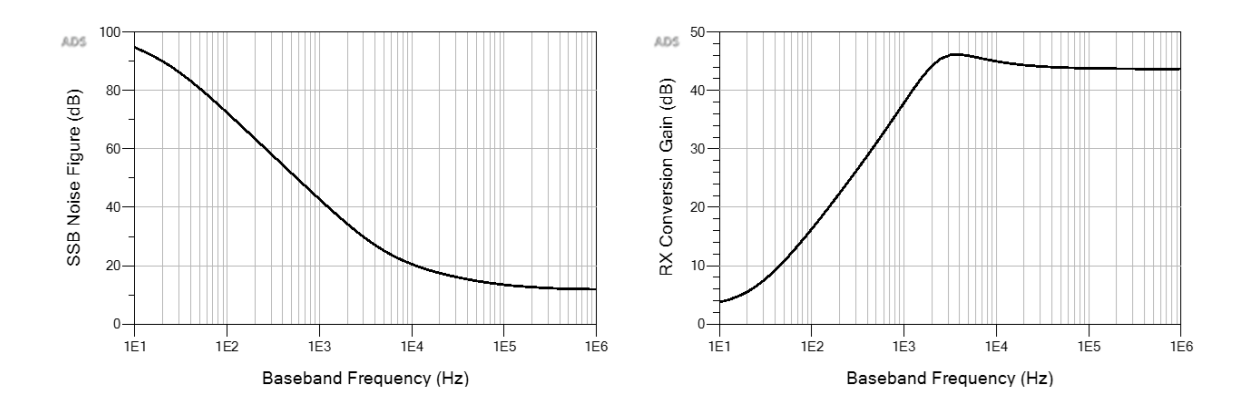


Fig. 5-26. Simulated conversion gain and SSB NF of the single-antenna TRX with the closed-loop leakage cancellation.

Fig. 5-27 shows the simulation results of the chip output power, RX conversion gain, and SSB NF versus LO frequency. Within the operation bandwidth of the chip (i.e., 78-

82 GHz), the chip generates an output power of larger than 1 dBm. The SSB NF at the flicker corner is less than 14 dB and a conversion gain of greater than 43 dB is obtained for the RX.

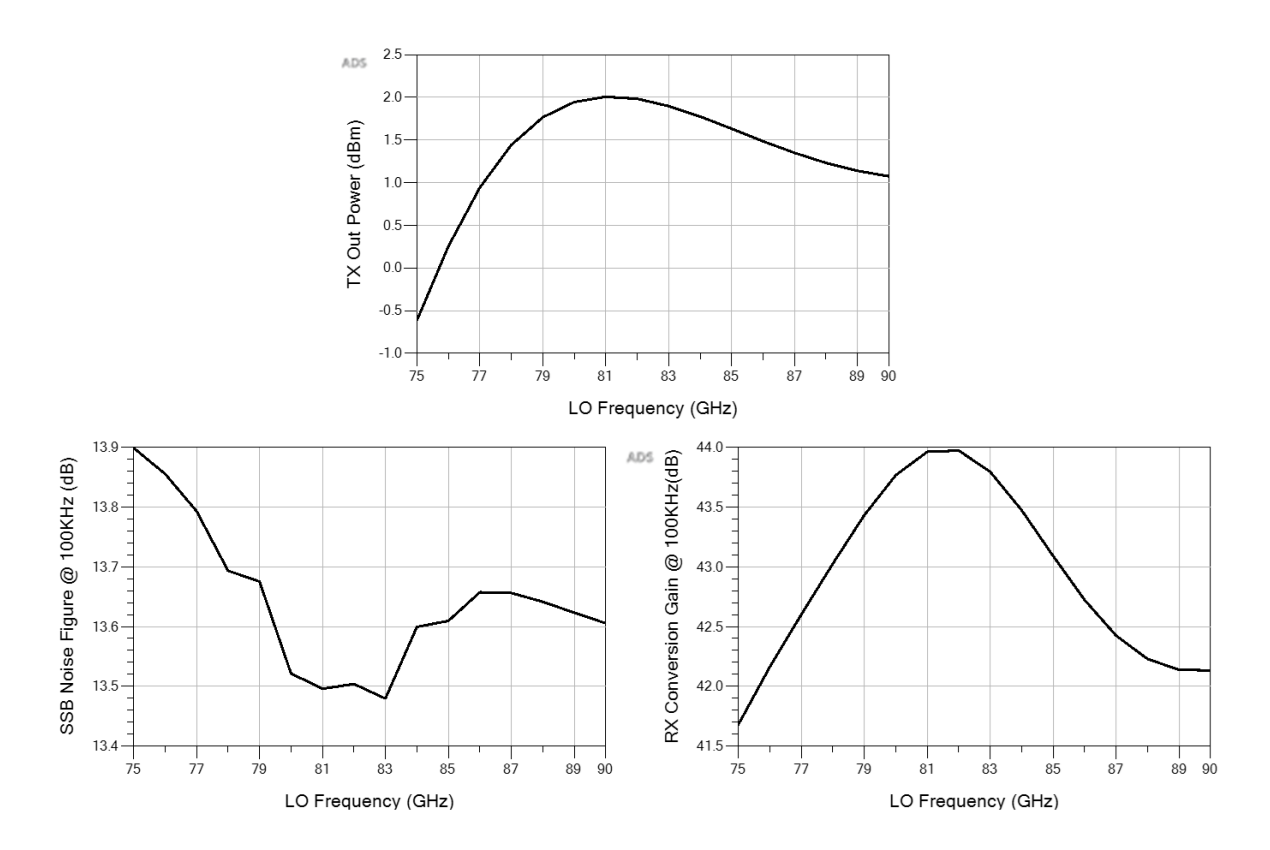


Fig. 5-27. Simulated chip output power, SSB NF, and conversion gain of the RX versus LO frequency.

To show that the proposed architecture is able to tolerate antenna port mismatches, the antenna port is terminated with a load with a return loss of 15 dB. The simulation shows that the proposed single-antenna TRX with leakage cancellation can tolerate an antenna return loss of higher than 15 dB with any phase. Fig. 5-28 shows the simulation results of the output power, SSB NF, and the RX conversion gain versus the phase of the return loss of a load with a return loss of 15 dB, showing a robust result.

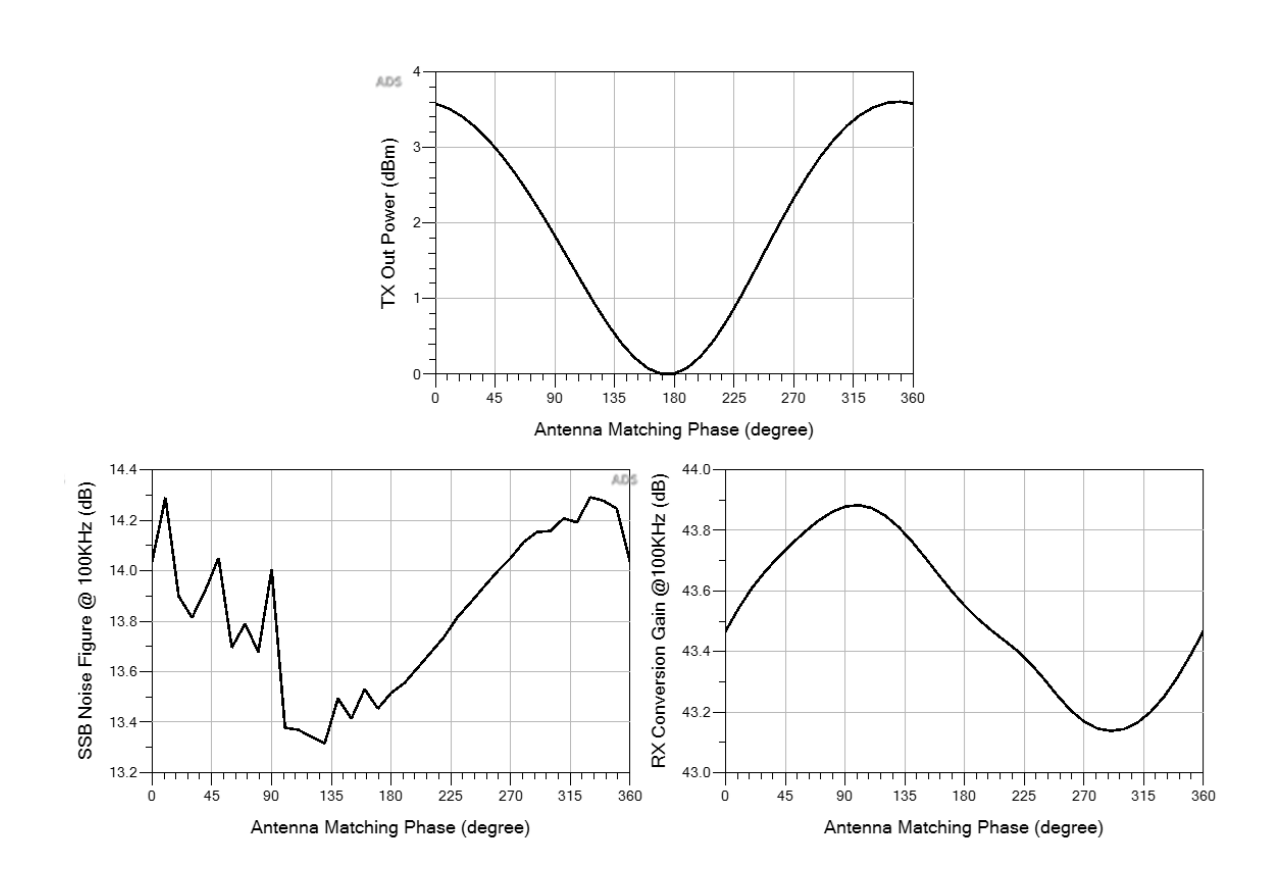


Fig. 5-28. Simulated chip output power, RX conversion gain and receiver noise figure versus antenna port's matching for the 360° phase sweep.

Chapter 6

Measurement

In this chapter, the measurement results of the fabricated chip on TSMC65GP will be demonstrated. This includes the probe measurements to characterize the TX and RX at the pads of the chip, and the field tests of the radar operation, attaching the chip to a PCB with an antenna on-PCB. The chapter ends with a performance comparison between the results of the proposed single-antenna and measurements of the previously published works.

In order to measure the chip, a testing module is designed. The testing PCB contains two low-frequency and RF boards. The chip is bonded to an RF board, manufactured on a 5 mil low loss Rogers material (RO3003), including the RF paths for delivering the reference signals to the chip and an antenna on-PCB for the radar operation testing. The low-frequency board, built on an FR-4, contains the supply regulators for powering up the chip and differential to single-ended operational amplifiers to buffer the I and Q differential signals with an external gain of 40 dB. The schematics of the supply regulators and the baseband amplifiers on the low-frequency board are shown in Fig. 6-1 and Fig. 6-2, respectively. The module requires three voltage to operate: 1) a +2.8 V supply to produce the +1.2 V, 90 mA that powers up the chip, 2) a +15 V, 10 mA supply for the positive biasing of the opamps, and 3) a -15 V, 10 mA supply for the negative biasing of the opamps. The complete module is shown in Fig. 6-3.

In order to control the biasing voltages and currents of the circuit blocks, and also to adjust the PC and gain settings, a digital shift register is employed to program the

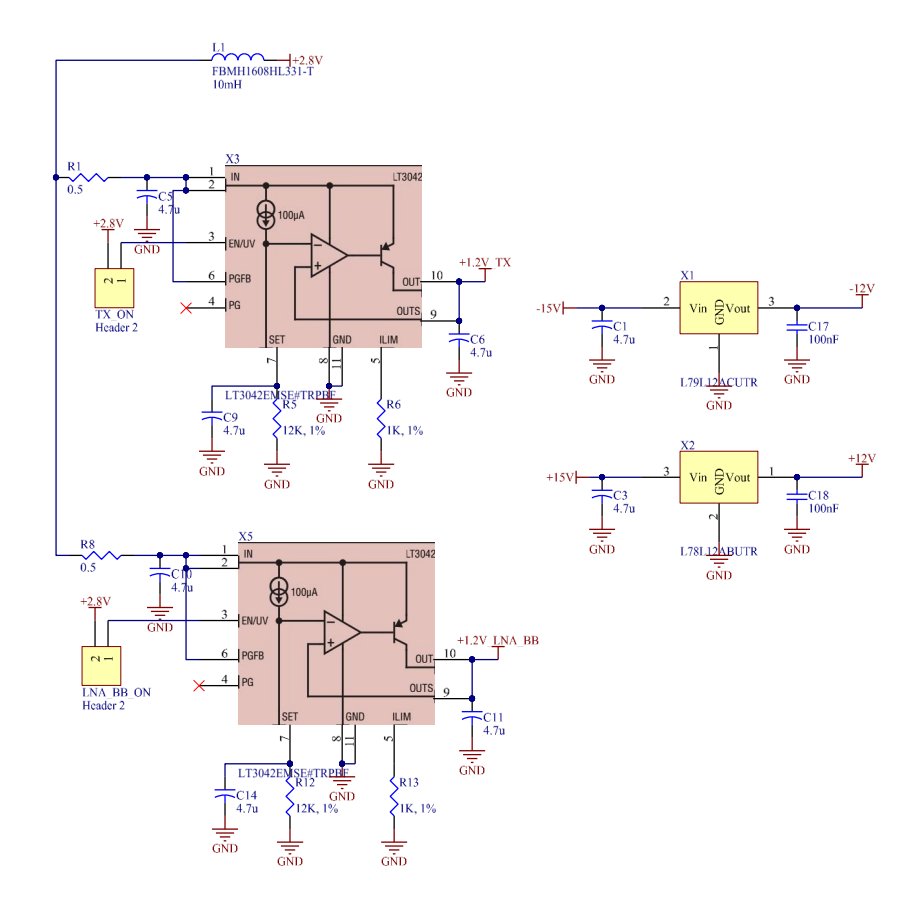


Fig. 6-1. Schematic of the supply regulators on the FR-4 low frequency PCB.

settings serially, avoiding to use many IO pads. A graphical interface program is designed to easily program the chip through a Labjack USB programmer and only four digital serial connection as shown in Fig. 6-4.

6.1 Probe measurements

The chip microphotograph and the equipment used for measuring the chip including microprobe, signal sources and the SMZ mixer are shown in Fig. 6-5 and Fig. 6-6, respectively.

6.1.1 TX block

The measurement setup for measuring the output power signal, locking range, and the PN of the TX is shown in Fig. 6-7. In this setup, the output signals are picked up using

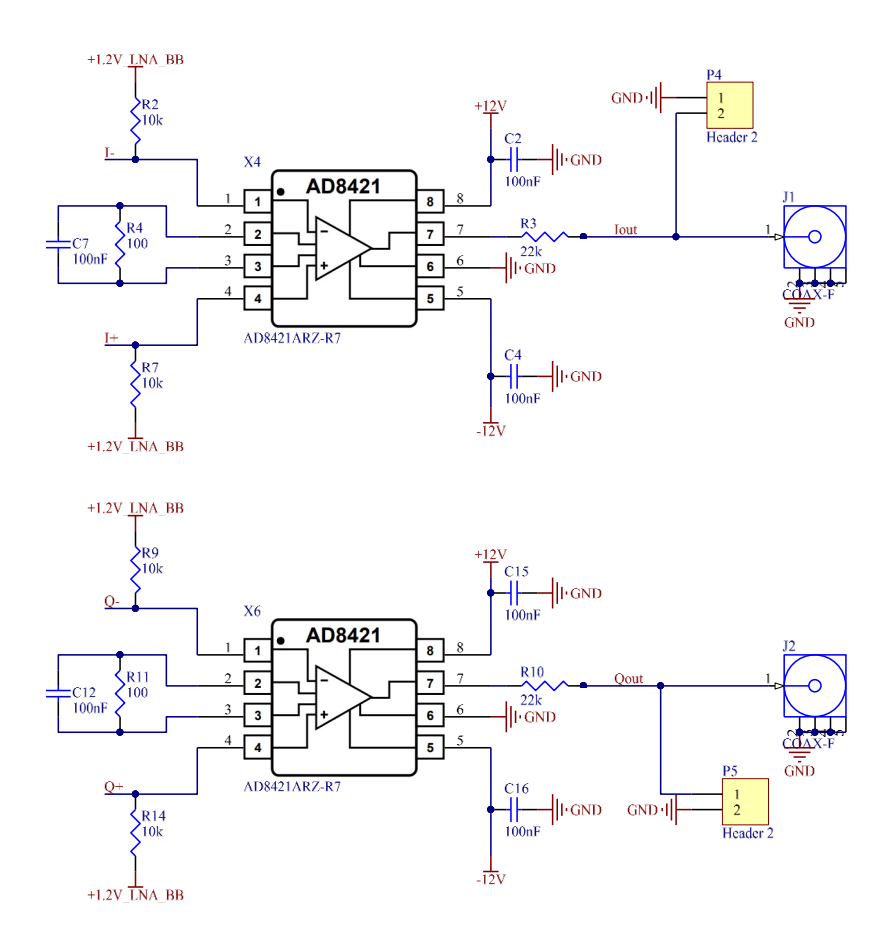


Fig. 6-2. Schematic of baseband amplifiers with 40 dB of differential to single-ended voltage gain.

the E-Band waveguide microprobe. To capture the spectrum of the signal, an R&S SFW spectrum analyzer is used. Since the maximum measuring range of the spectrum analyzer is limited to 67 GHz, the 80-86 GHz signal of the chip is down-converted using an E-band mixer module with an LO signal of 67 GHz, generated by an R&S SMF100A + SMZ75 signal generator. The down-converted signal in the frequency range of 17-21 GHz then feeds to the spectrum analyzer. Another signal generator (Agilent E8257D) is used as the reference signal of the chip at one-third of the output frequency (26.6-28.6 GHz).

The measured locking range of the ILFT and the output power of the chip are plotted in Fig. 6-8. The measurement shows a +2 GHz frequency drift for the ILFT compared to the simulations, shown in Fig. 5-24. Process variations and overestimation of the parasitics of the transistors are the reasons that cause this frequency shift. A locking range of 1.5 GHz is measured in each coarse tuning of the capacitor bank when an estimated input power of

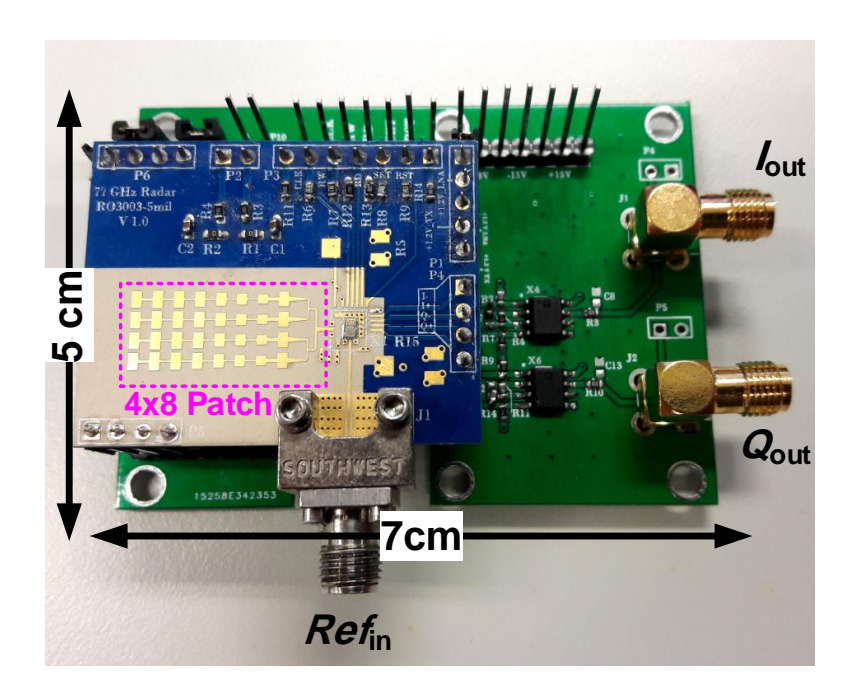


Fig. 6-3. W-band single-antenna radar front-end module including the chip, on-PCB antenna, baseband amplifiers, and voltage regulators.

5 dBm is injected into the chip. It can be seen that there is enough frequency overlapping between neighbored coarse tuning bits to ensure that TX can cover whole the frequency range without any gap. To achieve a consistency between the simulated and measured output powers, in terms of the frequency, another simulation was performed in which the ILFT was bypassed and a signal source with a similar amplitude of the ILFT directly generated the desired frequency. The simulated output power of the chip is also plotted in Fig. 6-8. As previously mentioned, since the LNA was designed for a considerably wider bandwidth, the frequency drift is still within the operational bandwidth of the LNA and the PA and does not affect the performance of the chip.

The PN spectrum of Agilent E8257D signal generator is obtained from the datasheet of the equipment is shown in Fig. 6-9. Fig. 6-10 shows the PN performance of the chip. It can be seen that when the reference signal is turned off, the spectrum of the ILFT is not pure, generating a high level of PN. The measured PN at the frequency offset of 1 MHz is -82 dBc/Hz, which is close to the simulated PN for 65-nm CMOS at W-band. When the ILFT is locked to the reference signal generator, the PN level goes down to

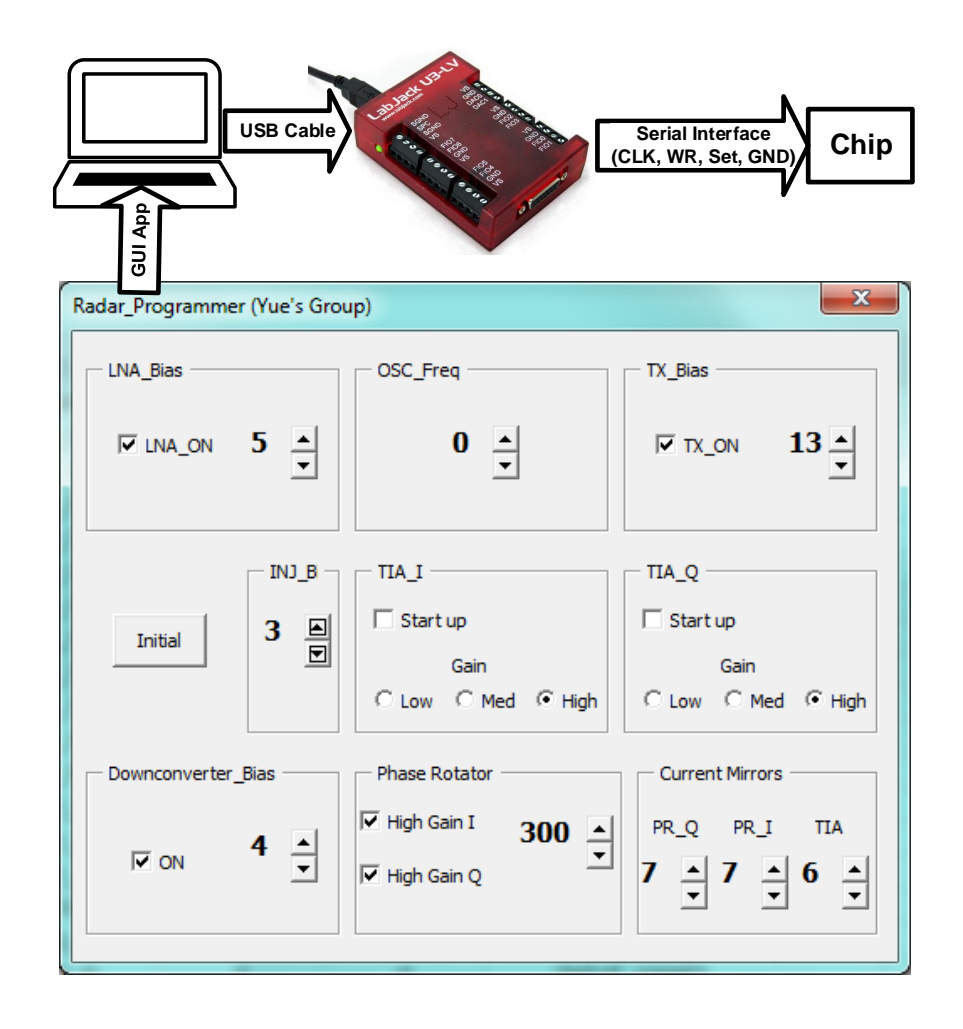


Fig. 6-4. Programming the internal shift register of the chip using the GUI app and the Labjack serial programmer.

-113 dBc/Hz at the frequency of 1 MHz thanks to the spectral purity of the source. As expected, the PN spectrum of the ILFT has a same profile as the PN of the signal generator except for additional 9.5 dB due to the multiplying factor of 3 (i.e, $20 \log N$). As described in Section 3.3.4, the PN performance in LRR, MRR, and SRR needs to be better than -80 dBc/Hz, -60 dBc/Hz, and -40 dBc/Hz, respectively, frequency offsets of 10-70 kHz in case of a big target scenario, as shown in Fig. 3-9. On the other hand, the PN skirt of leakages at the input of the RX can dictate the PN performance of the TX. Accounting the PN correlation effect in (3.9), with a given delay of 1 mm inside the chip, a PN cancellation of 80 dB at 1 MHz frequency offset is achievable. Assuming TX to RX isolation of 40 dB (after the leakage cancellation) and TX output power of 6 dBm, the PN of less than -60 dBc/Hz at 1 MHz is required to ensure the PN level goes below the

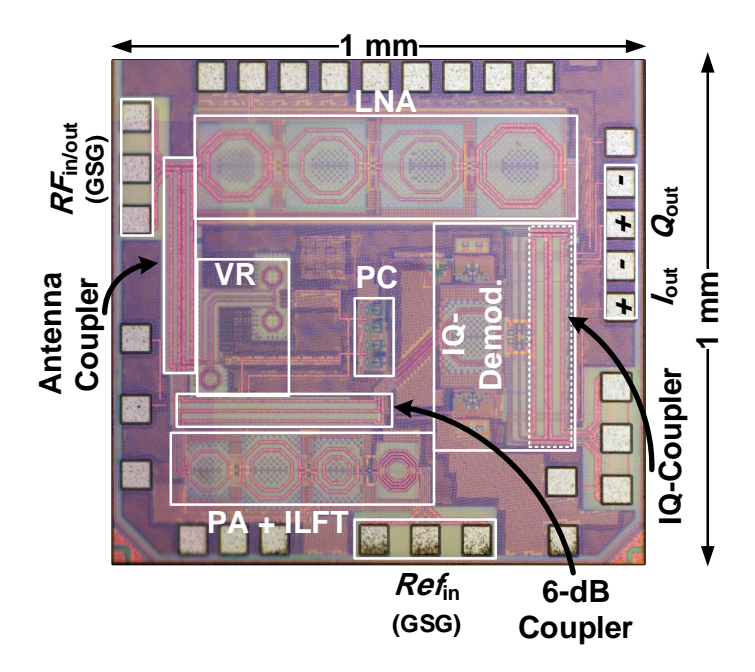


Fig. 6-5. Chip microphotograph of the fabricated chip on 65 nm CMOS technology.

noise floor. As a result, the PN of the TX in the locked condition can meet both of the above criteria.

6.1.2 RX block

The RX characterization includes two measurement setups. In the first setup, the conversion gain and NF of the RX are measured using a calibrated noise source, as shown in Fig. 6-11. The measurement setup uses a signal generator as the reference of the chip, an E-band waveguide noise source with excess noise ratio (ENR) of 15 dB, and the spectrum SWF analyzer, adjusted for NF measurement and drives the noise source power. The spectrum analyzer in the noise measurement mode automatically calculates the gain and NF using the Y-factor method [74]. Since the measured noise in this configuration uses only the I or Q path, the noise folding effect is not eliminated. The SSB NF for the quadrature RX can be calculated by subtracting 3 dB for the noise folding. The noise has an internal isolator at its output. Using the noise source with the isolator prevents the TX output signal, which is simultaneously generated by the TX at the shared antenna port, to reflect inside the RX.

The measured SSB NF and conversion gain of the RX are shown in Fig. 6-12. Com-

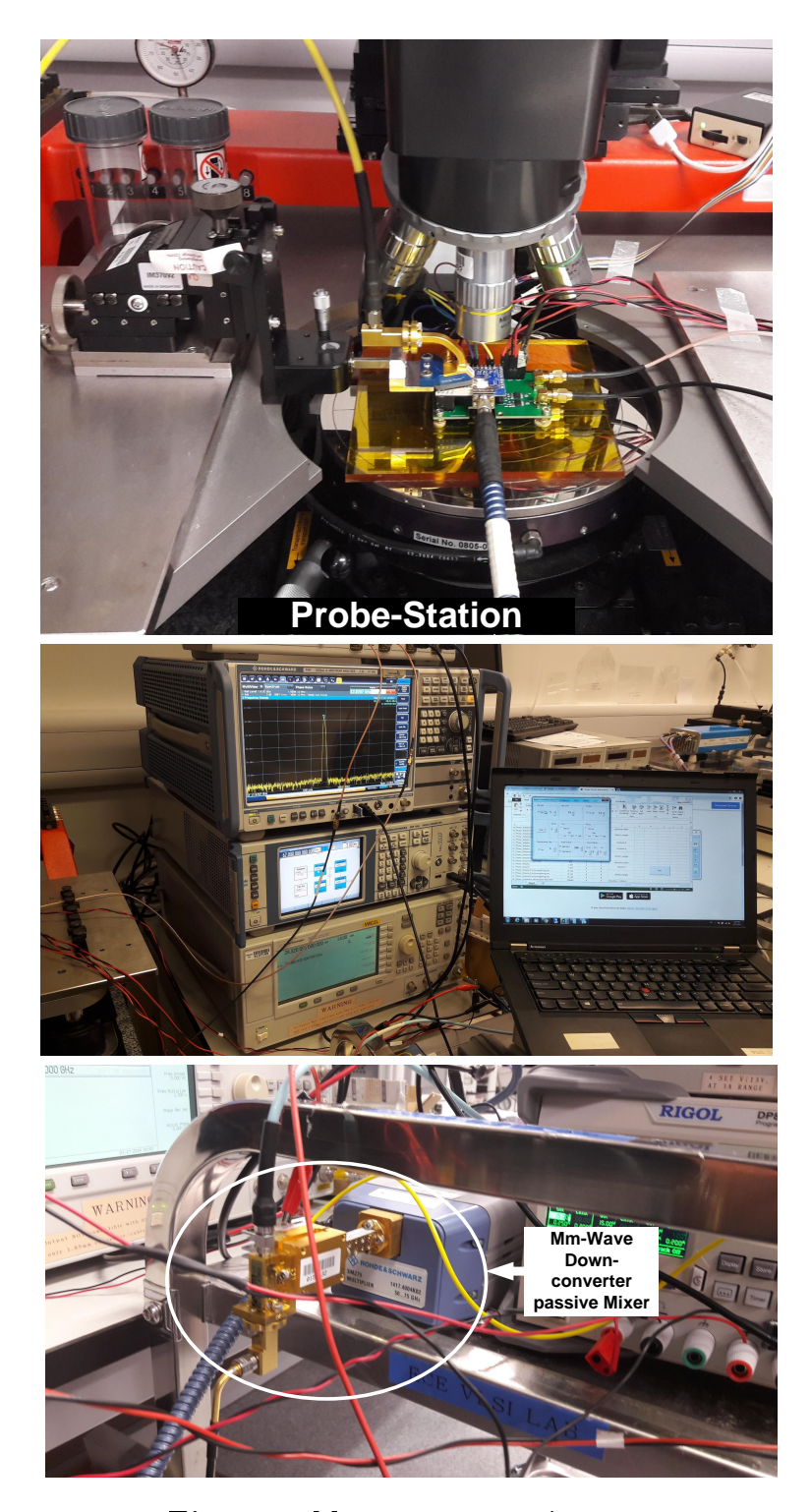
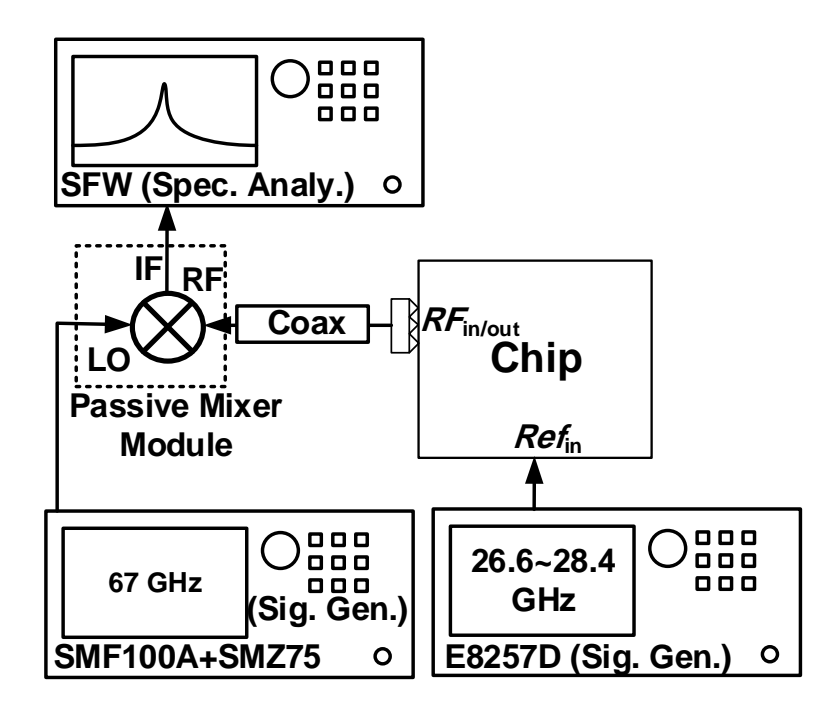


Fig. 6-6. Measurement equipment.

pared to the simulation results, 3 dB reduced gain and 4 dB increased NF is observed. One reason for the discrepancy is the higher insertion loss of using an E-band instrument at W-band. The other factor is the unwanted baseband switching noise, coupled from the noise source power cable to the RX.



The insertion loss of 26dB for the RF path, including the Coaxial + Probe + Passive mixer at 80GHz, is calibrated.

Fig. 6-7. TX measurement setup.

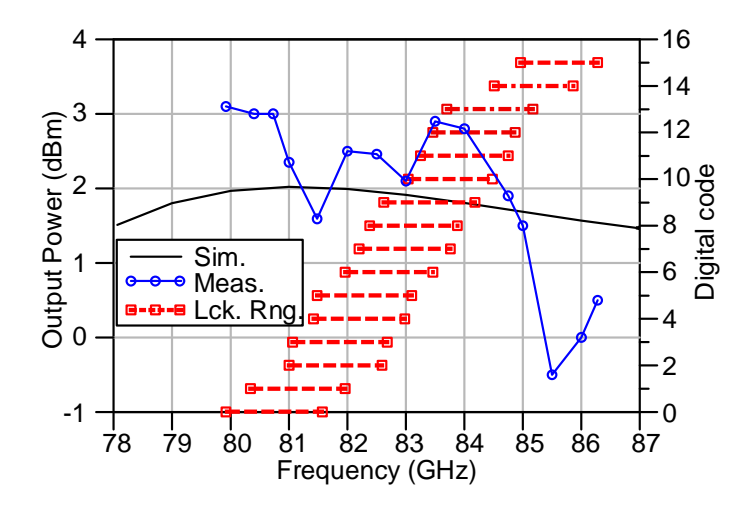


Fig. 6-8. Measured frequency locking range and the output power of the TX.

The second measurement setup is used to characterize the adaptive leakage cancellation of the proposed single-antenna RX. In order to measure it, an external RF source is utilized to inject an emulated leakage signal through the antenna port of the chip. The

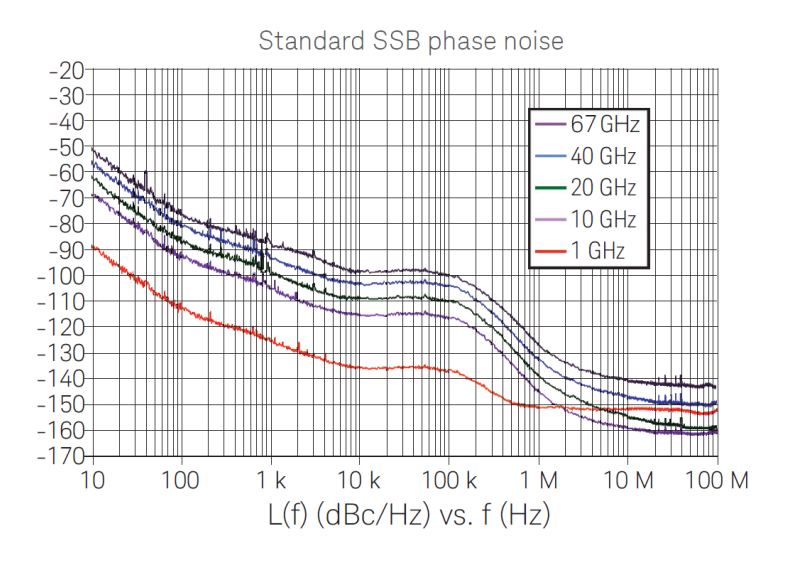


Fig. 6-9. SSB Phase noise performance of Agilent E8527D.

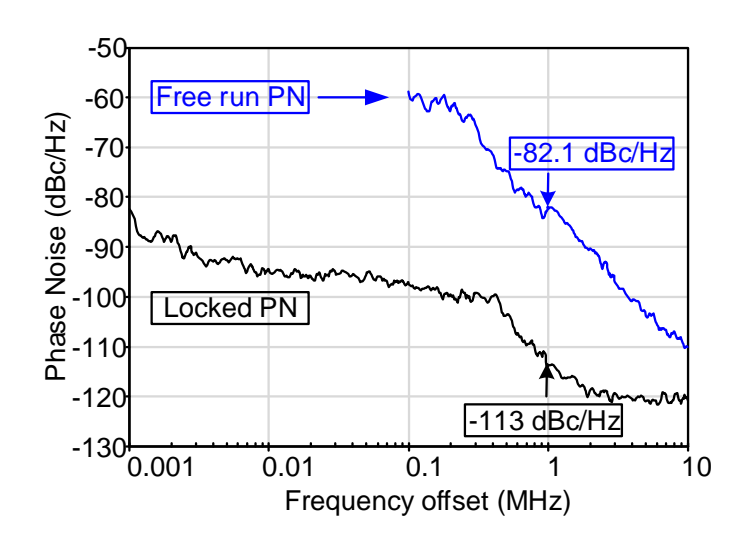


Fig. 6-10. Measured PN of the TX in the locking and unlocking conditions.

frequency of the injected leakage is swept from the TX frequency of the chip (i.e., exactly the same as the TX leakage) to a frequency offset of 100 kHz from that, as shown in Fig. 6-13. The setup uses a passive mixer and two signal generators (SMF100A+SMZ75 and HP8360), synchronized with the reference signal, to generate the RF leakage signal. The generated signal is fed to the chip through a coaxial cable and cascade micro probe. Total insertion loss of 26 dB is calibrated for the passive mixer, coaxial cable, and micro probe at 80 GHz. The attenuation of the coaxial cable at W-band, in this measurement, helps to reduce generating unwanted mixing products between the chip output power and that generated by the mixer at the RF frequency. While the passive mixer is generating

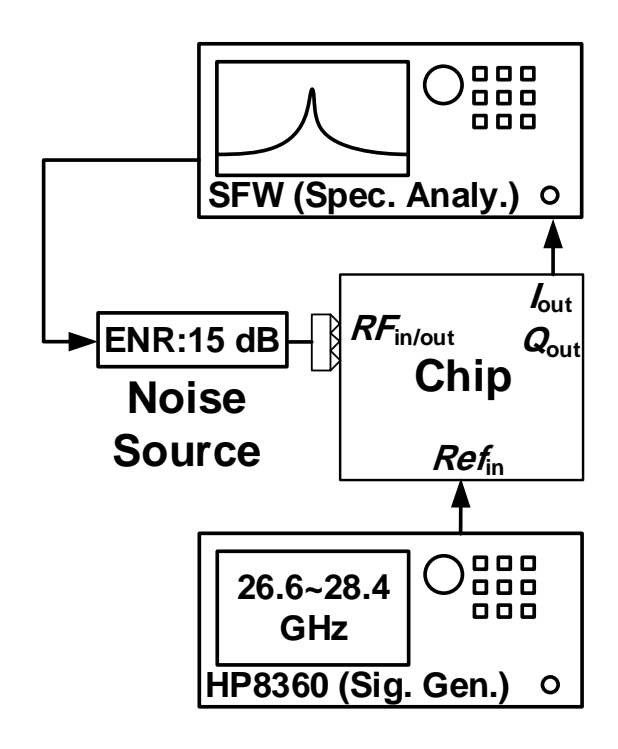


Fig. 6-11. Measurement setup for RX conversion gain and NF.

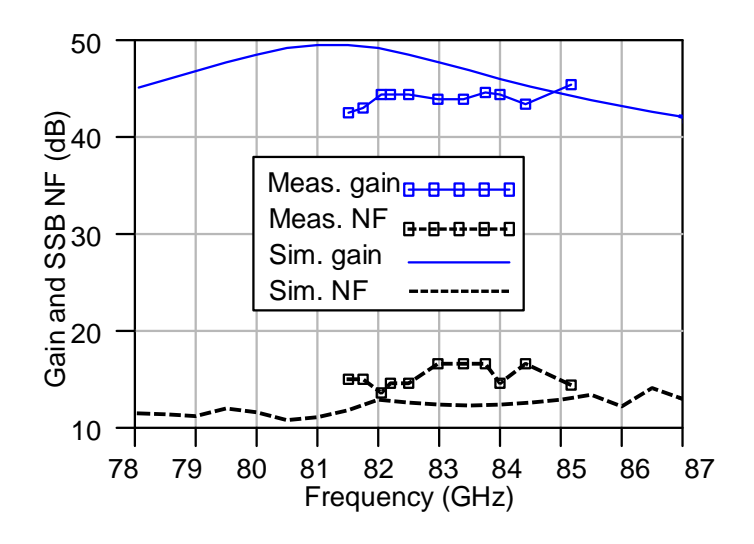
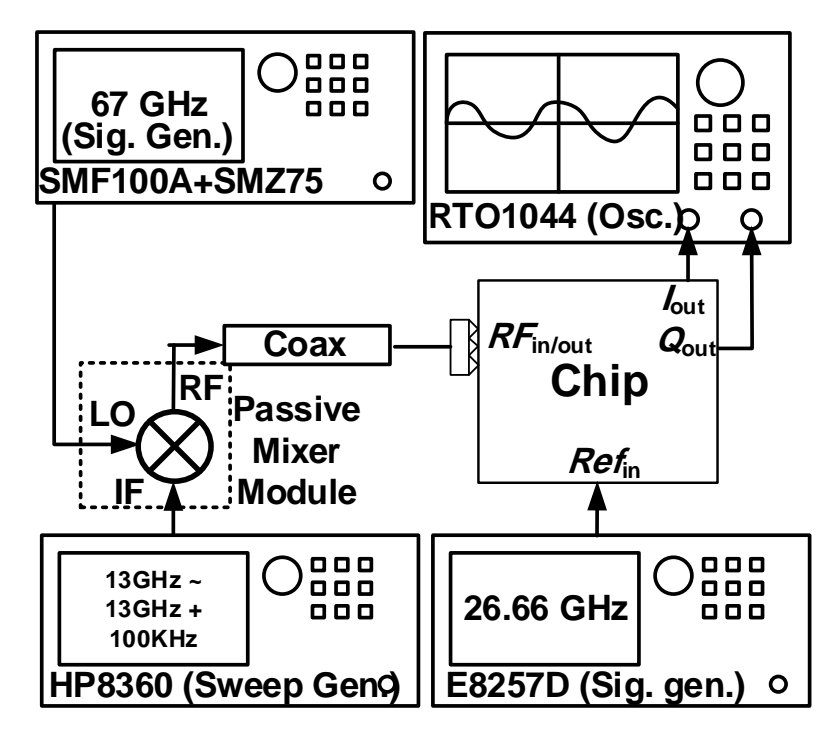


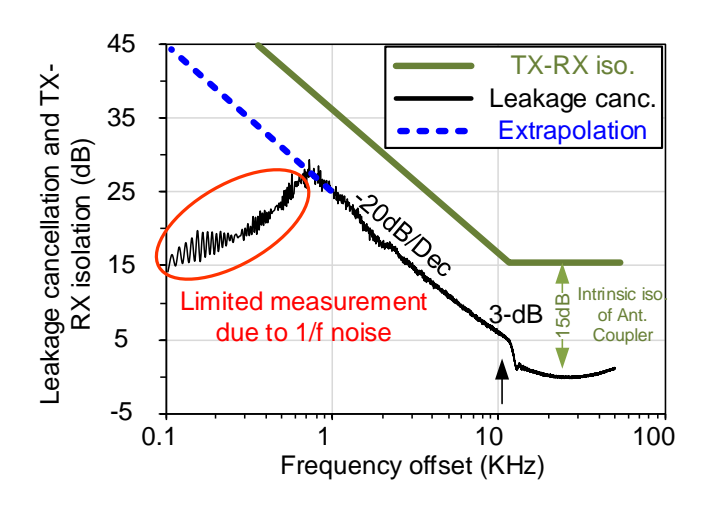
Fig. 6-12. Measured conversion gain and NF of the RX.

the emulated leakage signal at its RF port, the output power of the chip is simultaneously interfere to the RF port of the mixer, which can potentially degrade the linearity and performance of the mixer. Therefore, having a lossy path between the chip and the passive mixer results in a less interference between the signals that arrive at the RF port of the mixer, and allows the mixer to operate with a better linearity.



The insertion loss of 26dB for the RF path, including the Coaxial + Probe + Passive mixer at 80GHz, is calibrated.

Fig. 6-13. Measurement setup for characterization of the RX cancellation.



 $\textbf{Fig. 6-14.} \quad \text{Measured adaptive cancellation characteristic of the proposed closed-loop leakage cancellation RX.}$

The FFT of the baseband output is captured using the oscilloscope (RTO1044). The normalized output spectrum is plotted in Fig. 6-14. It can be seen that the RX has a

minimum cancellation for the frequency offsets of greater than 11 kHz, which is normalized to 0 dB, while the cancellation starts growing up for the lower frequency offsets with a slop of 20 dB/Dec thanks to the first order loop filter (the integrator in the PC). The cancellation is measurable down to the frequency offsets of 1 kHz and is dimmed into the flicker noise of the RX. Continuing the trajectory of the curve by 20 dB/Dec, a cancellation more than 40 dB is expected theoretically at frequency offsets below 100 Hz. The cancellation characteristic is well matched to the theoretical analysis and simulations of the proposed single-antenna TRX. Adding 15 dB for the intrinsic isolation of the antenna coupler (based on simulations), the measured isolation of 40 dB (at the frequency offset of 1 kHz) is obtained. It is estimated that an isolation level of more than 55 dB is also obtained for the lower frequency offsets based on the protracted curve of Fig. 6-14.

6.2 Field tests

To show the functionality of the proposed single-antenna TRX as an FMCW radar frontend, a radar demo module including the antenna on-PCB is designed on a 5-mil RO3003 Rogers material, suggested for automotive radar applications, as shown in Fig. 6-3. The important factor for the single-antenna TRX is the antenna to chip interface since any mismatch at the antenna port reflects the TX power into the RX. Though the flip-chip is a common packaging technique at the mm-wave band, in this work, the conventional low frequency bond wire is employed because of a lack of experience on the flip-chip technology and the higher manufacturing cost of it. The half-wavelength GSG bonding wire technique [75, 76] is employed as the transition medium between the chip and the antenna at W-band, as shown in Fig. 6-15(a). The ground-signal-ground (GSG) bond wires form a CPW t-line on air with a simulated characteristic impedance of 150-200 Ω . Theoretically, any half wavelength t-line with none-50 Ω characteristic impedance does not degrade the impedance matching at the center frequency. In this work, a 4×8 patch antenna array is used to obtain an antenna gain of 15 dBi. The whole patch antenna structure along with its power combiners and the half wavelength (1.9-mm at W-band) bonding wires have been optimized together at the frequency of 77-81 GHz to achieve an antenna return loss of better than 12 dB. Fig. 6-15(b) and (c) show the simulated input matching and the antenna pattern, respectively, using HFSS. The input return loss and the gain of better than 12 dB and 15 dBi, respectively are obtained for the optimized antenna.

The radar demo measurement setup is shown in Fig. 6-16. The setup includes the reference signal generator (HP8360) to create the FMCW frequency ramp at the one-third of the output frequency, the single-antenna module, and the oscilloscope (RTO1044) to process the baseband signal using its real-time FFT function.

The signal source generates a frequency chirp of 150 MHz at the center frequency of 26.6 GHz with a sweeping rate of 300 MHz/mS. The output signal of the radar is a 450 MHz chirp signal at 80 GHz thanks to the ILFT. The captured, amplified and down-converted signals from the objects are processed by the real-time FFT processor of the oscilloscope after 4 times averaging the waveforms to improve the SNR. A metal sheet of 40 cm×50 cm was detected at the distance of 19 m with an SNR of 20 dB. Three frames of the metallic object detection at different distances are shown in Fig. 6-17(a)-(c).

In another field test, the radar module is used to detect a small drone. In this test, the antenna looks upward to the sky and the drone is flied on top of the module. Two frames of the measurements are shown in Fig. 6-18(a) and (b). Since the drone is a tiny object that reflects less signal, the radar module is able to only detect the drone at a distance of up to 10 m with an SNR of higher than 10 dB. The range, however, can be improved by employing multi-channels of the single-antenna radar and forming phased-array to increase the total emission power. In addition, it would enable to create an electronically steerable radar beam, and to measure angular position as well.

The distance measurement accuracy of FMCW radars depends on the quality and accuracy of the generated ramp. From (2.25), the range measurement accuracy can be calculated by

$$\frac{\Delta R}{R} = \frac{\Delta T_0}{T_0} - \frac{\Delta BW}{BW},\tag{6.1}$$

where T_0 and BW is the sweeping time and the sweeping bandwidth, respectively. As a result, any uncertainty in the generated chirp introduces range measurement errors.

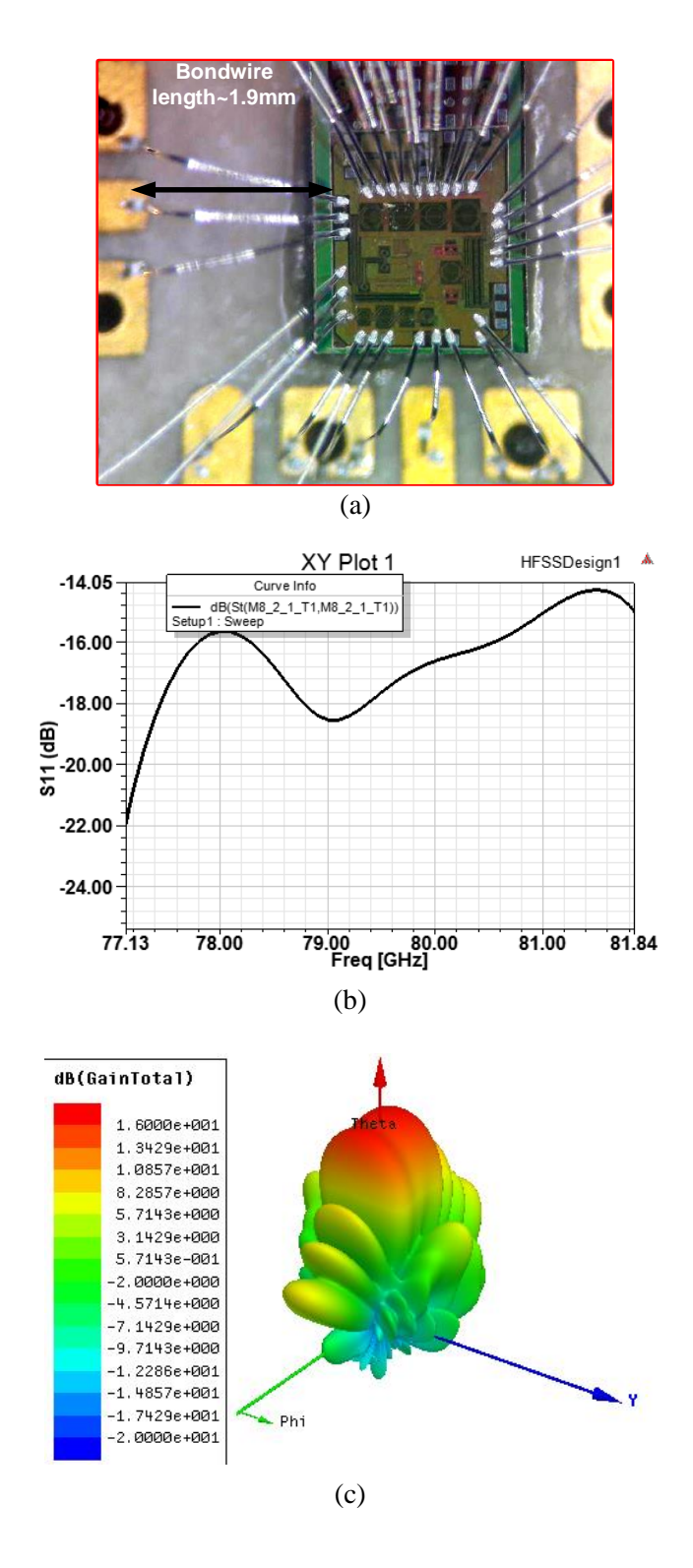
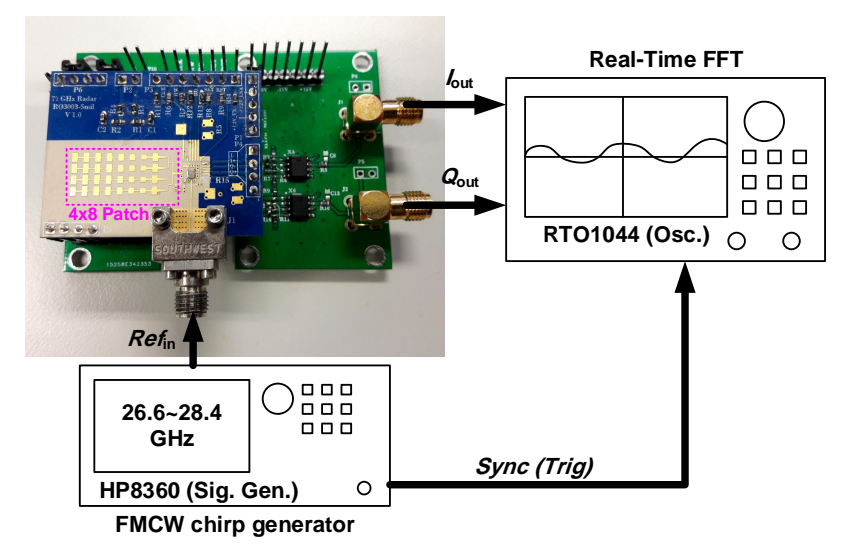


Fig. 6-15. (a) Manufactured chip on the radar PCB module using bonding wires. (b) Simulated input matching of the antenna, including the half wavelength bonding wire transition. (c) Simulated radiation pattern of the 4×8 patch antennas array.

Moreover, the linearity of the chirp is important since it can cause ghost or dispersed targets. In order to generate the ramp accurately, a direct digital synthesizer (DDS)



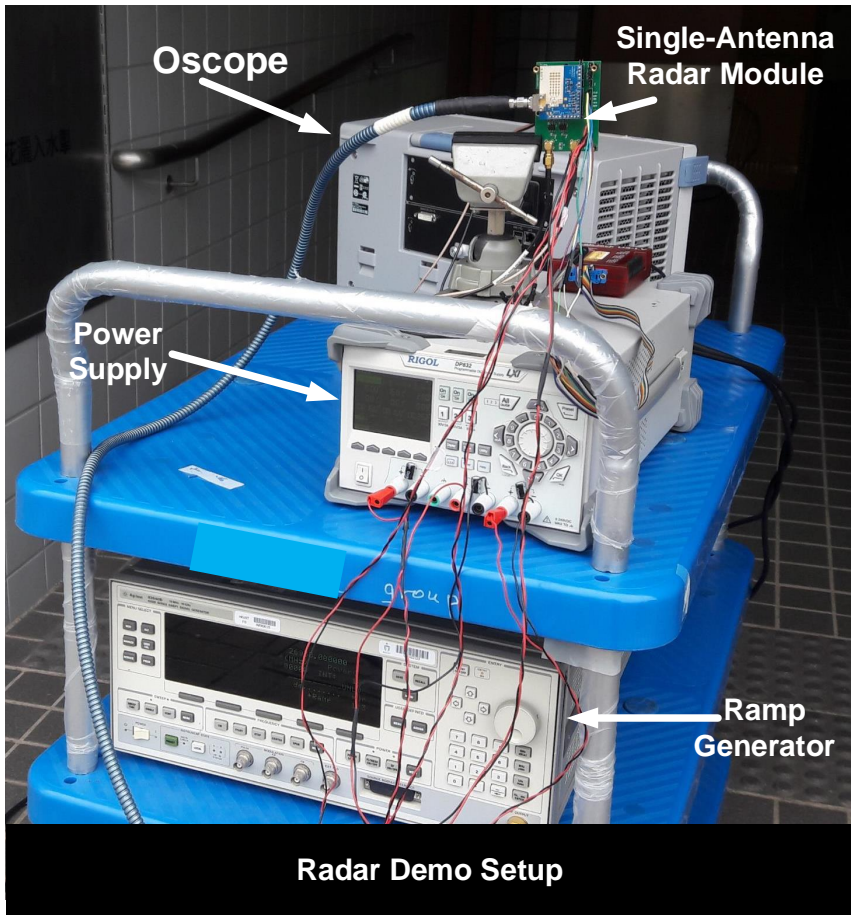


Fig. 6-16. Measurement setup for demonstration of the proposed single-antenna FMCW radar operation.

followed by a frequency synthesizer is required which is out of the scope of this project. Therefore, the accuracy of the field tests is mainly limited to the performance of the equipment that has been used.

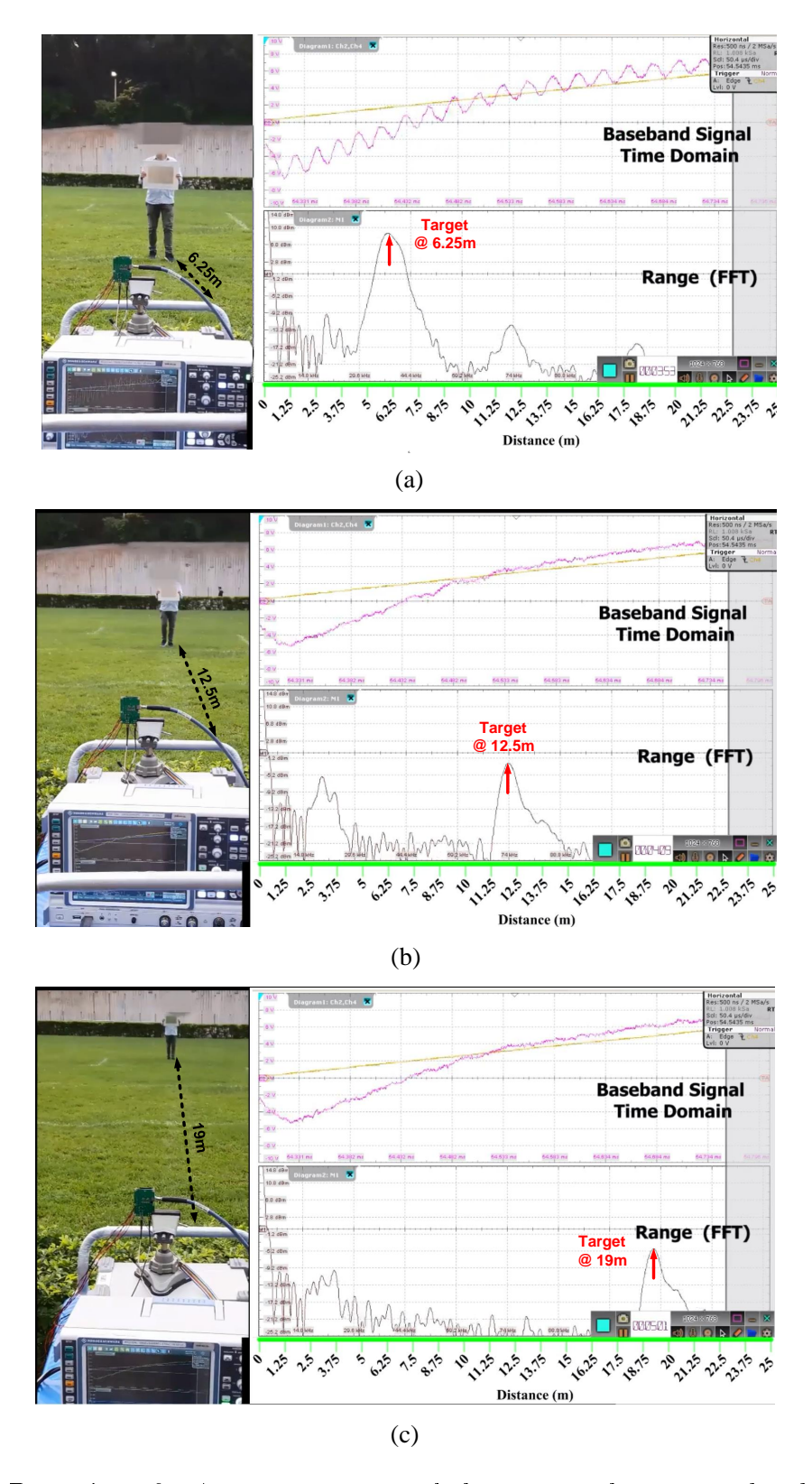


Fig. 6-17. Detection of a $40 \text{ cm} \times 50 \text{ cm}$ metal sheet using the proposed radar chip at a distance of (a) 6.25 m, (b) 12.5 m and (c) 19 m.

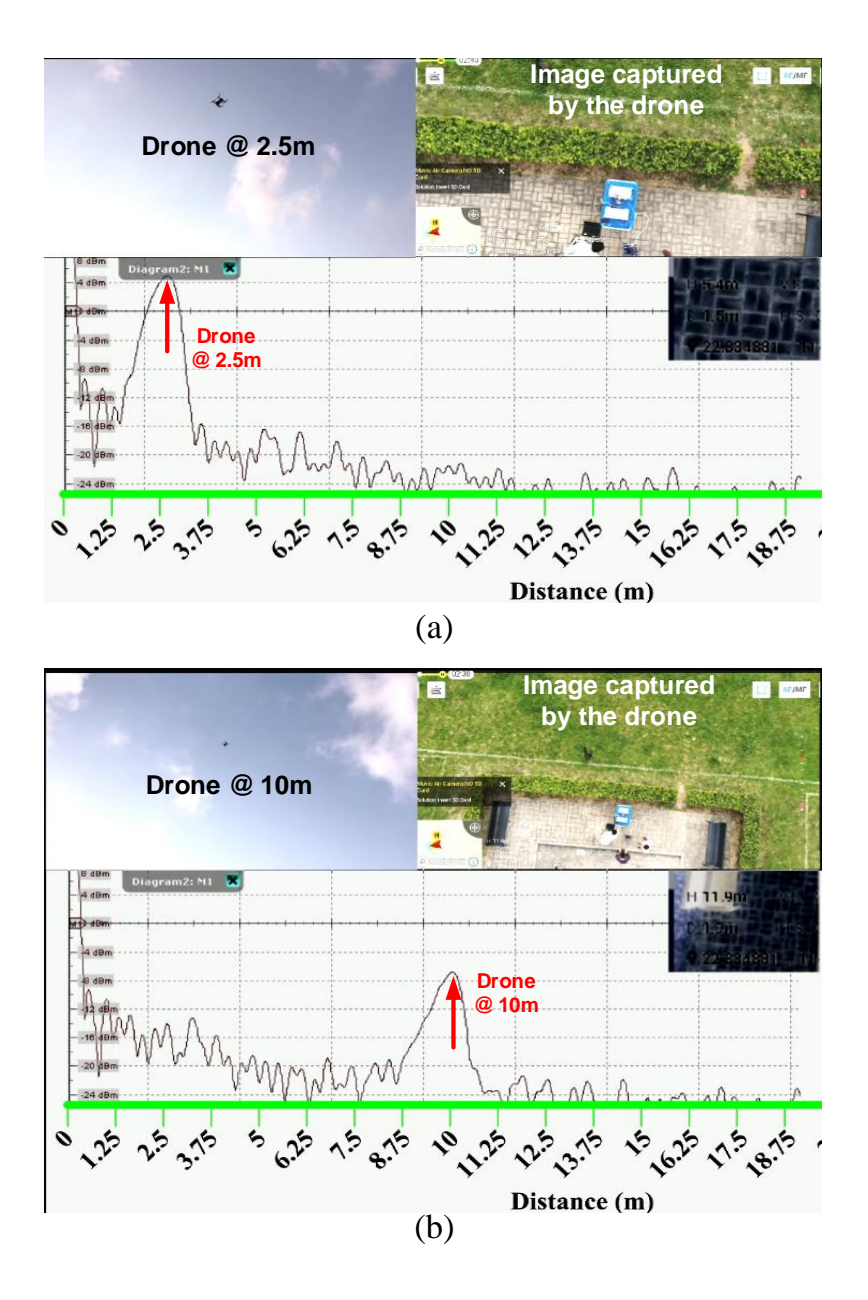


Fig. 6-18. Detection of a flying drone using the proposed radar chip at a distance of (a) 2.5 m, and (b) 10 m.

6.3 Performace summary

The performance of the proposed single-antenna TRX is summarized and compared to the prior works in Table 6.1.

In addition, the performance comparison between the proposed single-antenna and the two commercialized ICs for automotive radar is performed which is shown in Table 6.2. Since the other commercial products use multi-channel TRXs (typically four channels for the RXs and two channels for the TXs), it is assumed that four channels of the

Table 6.1: Performance summary and comparison to the previous arts

	This work	[77]	[55]	[78]	[79]
Process	65-nm	28-nm	90-nm	0.13-um	65-nm
	CMOS	CMOS	CMOS	CMOS	CMOS
Function	Single	LNA+	Single	Single	Single
	Ant.	Leakage	Ant.	Ant.	Ant.
	TRx	Canceller	TRx	TRx	TRx
Freq (GHz)	80-85	80	60	23.8-24.5	9.8-10.2
Tx P _{out} (dBm)	2	_	3	-1.6	10.5
PN (dBc/Hz)	-82.1	_	-92	-105.4	-102.3
@ 1 MHz	-02.1				
Rx Gain (dB)	45	15.2	10.5	15.3	32
NF (dB)	15	5.5^{a}	_	11.6	16.8
Iso. (dB)	45	27.5	53.4	47.3	45
P _{dc} (mW)	108	47	217	111	147^{b}
Area (mm ²)	1	1.44	4	1.53	3.8^{b}

^aOnly for LNA.

proposed single-antenna TRXs are employed in a phased array configuration to make a fair comparison. In Table. 6.2, the normalized maximum range of the radars is calculated using (4.3).

The comparison shows acceptable performance for the proposed design. It is noteworthy that despite 20% range degradation of the proposed radar, the power consumption and the total antenna size are 50% and 33% smaller, respectively.

^bIncluding front-end, synthesizer, baseband and ADC circuits.

Table 6.2: Comparison with two commercialized products

Parameter	NXP [39,40]	TI [41]	This Work	
Frequency (GHz)	76-77	76-81	77-81	
Supply Voltage (V)	3.3	1.3	1.2	
Number of RXs	4	4	1	
Number of TXs	2	2	1	
Power Consumption	1.63^a	2.1^{a}	0.113^{b}	
(W)	1.03		0.452^{c}	
RX Gain (dB)	23-60	48	45	
Noise Figure (dB)	14	15	15	
RX Architecture	Mixer First	LNA + IQ Mixer	Leakage Cancellation	
1071 Michieleute	WHACT THIS	DIVIT TO WINCI	(Single-Antenna)	
TX Output Power	10	12	2	
(dBm)	10	12		
Normalized Maximum	0.94	1	0.79	
${\bf Maximum}{\bf Range}^d$	0.34	1		
Technology	BiCMOS (SiGe)	45-nm RFCMOS	65-nm CMOS	

 $[^]a$ Power consumption for 2 TX and 4 RX b For single TX and single RX c For 4 TX and 4 RX d Assumed 4-channel single-antenna architecture

Chapter 7

Conclusion

In this dissertation, a novel single-antenna architecture for FMCW radar TRXs was proposed at W-band. Sharing a single antenna for both the transmitter and receiver though reduces the size of the sensor by a factor of two, creates a transmit to receive leakage issue which can easily saturate the receiver. The transmitter leakage issue is a disadvantage of the CW radars which usually omitted by using highly isolated antennas for the transmitter and receiver. In this project, we have addressed and solved the leakage problem for a single-antenna architecture using a new leakage cancellation technique for the first time at W-band. For this propose, a variable reflector with only two orthogonal tuning parameters was proposed to increase the isolation of the input antenna directional coupler. The variable reflector is adjusted by an analog feedback loop to track and cancel out the leakage of the transmitter, adaptively.

The single-antenna architecture was implemented on a 65-nm CMOS chip with a die area of only 1 mm² for W-band which is assigned for automotive radar applications. The measurements of the chip show a TX output power of 2 dBm, an NF of 15 dB, and an RX conversion gain of 45 dB at W-band. The cancellation characteristic of the chip was also measured to be greater than 40 dB.

The chip then was utilized in a radar module including an antenna on-PCB to demonstrate the operation of the chip in the practical radar tests. Using the module, a metal sheet of 40 cm×50 cm was detected at a distance of 19 m with an SNR of 20 dB, which successfully justifies the proposed single-antenna architecture for short-range automotive

applications. In addition, a small drone was detected at a range of 10 m. For the clarity of the radar tests the following remarks should be mentioned:

- Despite the chip bandwidth of 4 GHz, the radar tests have been performed in a narrower bandwidth of 450 MHz because of a difference between the frequency alignment of the chip and the antenna. Moreover, a digital controller synced to the frequency ramp generator is required to switch between the tuning bits of the ILFT block.
- Radars, unlike communication systems, do not need to meet any particular waveform. As a result, different configurations for the chirp is possible to achieve radar performance. In our experiments, the sweeping rate of the frequency ramp was limited to 300 MHz/ms due to the limitation of the signal generator.
- The measurement accuracy of the radar is a function of many parameters including the quality and accuracy of the frequency ramp generator. Any non-ideality of the chirp, such as non-linearity of the ramp, sweep time and the sweeping bandwidth, will result in range measurement errors.

7.1 Future works

The introduced architecture can be applied to the following items to improve the performance of future integrated radar systems.

- Though the focus of the thesis was on designing a radar for automotive applications, the proposed technique can be applied for any mm-wave imaging radar applications in security and medical systems, and also Doppler radars.
- Particularly, at higher mm-wave frequencies and terahertz band where the antenna on-chip becomes a feasible approach for exploiting the output power of the chip, using the proposed architecture significantly reduces the die area. In this regime, the on-chip antenna with a reasonable gain and efficiency would be yet the bulky

part of the silicon die, which can be reused for both the TX and RX thanks to the single-antenna architecture.

- Generation of an accurate fast chirp signal at the mm-wave band, as a heart of FMCW radars, can be a potential research topic for future projects.
- Employing this architecture in phased array TRXs can be another milestone for this project, which would significantly improve the performance of phased-arrays radars in terms of range, size and complexity of the system.
- Finally, integrating a fast chirp FMCW signal generator, phased-array, and base-band digital processor on the same chip would be the next step toward fully integrated radar on a chip, which has been out of the scope of this dissertation.

Acronym Glossary

ADC Analog to Digital Converter

ACC Automatic Cruise Control

AN Amplitude Noise

BER Bit Error Rate

BiCMOS Bipolar Complementary Metal Oxide Semiconductor

CMOS Complementary Metal Oxide Semiconductor

CPW Co-Planar Waveguide

CW Continuous-Wave

DDS Direct Digital Synthesizer

EIRP Equivalent Isotropically Radiated Power

EM Electromagnetic

FAR False Alarm Rate

FFT Fast Fourier Transform

FMCW Frequency-Modulated Continuous-Wave

GaAs Gallium Arsenide

GaN Gallium Nitride

GSG Ground-Signal-Ground

ILFT Injection Locked Frequency Tripler

InP Indium Phosphide

ISM Industrial, Scientific and Medical

Light detection and ranging

LNA Low Noise Amplifier

LO Local Oscillator

LRR Long Range Radar

mm-wave millimeter-wave

MOM Metal-Oxide-Metal

MRR Medium Range Radar

NF Noise Figure

PA Power Amplifier

PC Phase Compensator

PCB Printed Circuit Board

PD Probability of Detection

PMCW Pulse-Modulated Continuous-Wave

PN Phase Noise

PPF Polyphase Filter

PRF Pulse Repetition Frequency

PRI Pulse Repetition Interval

PVT Process Voltage and Tempreture

Radio detection and ranging

RCS Radar Cross Section

RF Radio Frequency

RPC Reflected Power Canceller

RX Receiver

SFC Sensitivity Frequency Control

SiGe Silicon Germanium

SNR Signal to Noise Ratio

SSB Single-Sideband

SRR Short Range Radar

TIA Transimpedance Amplifier

TRX Transceiver

TX Transmitter

T-line Transmission-line

UHF Ultra High Frequency

VGA Variable Gain Amplifier

VR Variable Reflector

Bibliography

- [1] D. Pozar, Microwave and RF Wireless Systems. Wiley, 2000.
- [2] M. Skolnik, Introduction to Radar Systems. McGraw-Hill Education, 2002.
- [3] "IEEE standard for information technology-telecommunications and information exchange between systems-local and metropolitan area networks-specific requirements-part 11: Wireless LAN Medium Access control (MAC) and Physical Layer (PHY) specifications amendment 3: Enhancements for very high throughput in the 60 GHz band," IEEE Std 802.11ad-2012 (Amendment to IEEE Std 802.11-2012, as amended by IEEE Std 802.11ae-2012 and IEEE Std 802.11aa-2012), pp. 1-628, Dec. 2012.
- [4] A. Arbabian, S. Callender, S. Kang, M. Rangwala, and A. M. Niknejad, "A 94 GHz mm-wave-to-baseband pulsed-radar transceiver with applications in imaging and gesture recognition," *IEEE Journal of Solid-State Circuits*, vol. 48, no. 4, pp. 1055–1071, April 2013.
- [5] A. Babakhani, X. Guan, A. Komijani, A. Natarajan, and A. Hajimiri, "A 77-GHz phased-array transceiver with on-chip antennas in silicon: Receiver and antennas," *IEEE Journal of Solid-State Circuits*, vol. 41, no. 12, pp. 2795–2806, Dec 2006.
- [6] A. Natarajan, A. Komijani, X. Guan, A. Babakhani, and A. Hajimiri, "A 77-GHz phased-array transceiver with on-chip antennas in silicon: Transmitter and local LO-path phase shifting," *IEEE Journal of Solid-State Circuits*, vol. 41, no. 12, pp. 2807–2819, Dec 2006.
- [7] K. Koh, J. W. May, and G. M. Rebeiz, "A millimeter-wave (40–45 GHz) 16-element phased-array transmitter in 0.18-μm SiGe BiCMOS technology," *IEEE Journal of Solid-State Circuits*, vol. 44, no. 5, pp. 1498–1509, May 2009.
- [8] S. Y. Kim and G. M. Rebeiz, "A low-power BiCMOS 4-element phased array receiver for 76–84 GHz radars and communication systems," *IEEE Journal of Solid-State Circuits*, vol. 47, no. 2, pp. 359–367, Feb 2012.
- [9] S. Kim and L. E. Larson, "A 44-GHz SiGe BiCMOS phase-shifting sub-harmonic upconverter for phased-array transmitters," *IEEE Transactions on Microwave Theory* and Techniques, vol. 58, no. 5, pp. 1089–1099, May 2010.
- [10] A. Santra, R. V. Ulaganathan, T. Finke, A. Baheti, D. Noppeney, J. R. Wolfgang, and S. Trotta, "Short-range multi-mode continuous-wave radar for vital sign measurement and imaging," in 2018 IEEE Radar Conference (RadarConf18), Apr. 2018, pp. 0946– 0950.

- [11] M. Alizadeh, H. Abedi, and G. Shaker, "Low-cost low-power in-vehicle occupant detection with mm-wave FMCW radar," arXiv e-prints, p. arXiv:1908.04417, Aug 2019.
- [12] A. Santra, I. Nasr, and J. Kim, "Reinventing radar: The power of 4D sensing," *MICROWAVE JOURNAL*, vol. 61, no. 12, pp. 26–38, 2018.
- [13] C. Shannon, W. Weaver, R. Blahut, J. T. T. C. U. of Illinois at Urbana-Champaign Library), U. of Illinois (Urbana), W. W. Collection, and B. Hajek, *The Mathematical Theory of Communication*, ser. Illini books. University of Illinois Press, 1963, no. pt. 11.
- [14] E. Juntunen, D. Dawn, S. Pinel, and J. Laskar, "A high-efficiency, high-power millimeter-wave oscillator using a feedback class-E power amplifier in 45 nm CMOS," *IEEE Microwave and Wireless Components Letters*, vol. 21, no. 8, pp. 430–432, Aug 2011.
- [15] O. Momeni and E. Afshari, "High power terahertz and millimeter-wave oscillator design: A systematic approach," *IEEE Journal of Solid-State Circuits*, vol. 46, no. 3, pp. 583–597, March 2011.
- [16] R. Adomat, G.-O. Geduld, M. Schamberger, and P. Rieth, "Advanced driver assistance systems for increased comfort and safety current developments and an outlook to the future on the road," in *Advanced Microsystems for Automotive Applications* 2003, J. Valldorf and W. Gessner, Eds. Berlin, Heidelberg: Springer Berlin Heidelberg, 2003, pp. 431–446.
- [17] S. M. Broek, E. van Nunen, and H. Zwijnenberg, "Definition of necessary vehicle and infrastructure systems for automated driving," 2011.
- [18] R. Rasshofer and K. Gresser, "Automotive radar and lidar systems for next generation driver assistance functions," *Advances in Radio Science*, vol. 3, no. B. 4, pp. 205–209, 2005.
- [19] P. Zador, S. Krawchuk, and R. Vocas, "Final report automotive collision avoidance (acas) program," Nat. Highway Traffic Safety Admin., Washington, DC, USA, Tech. Rep. DOT HS, vol. 809, p. 080, 2000.
- [20] C. Cui, S. Kim, R. Song, J. Song, S. Nam, and B. Kim, "A 77-GHz FMCW radar system using on-chip waveguide feeders in 65-nm CMOS," *IEEE Trans. Microw.* Theory Tech., vol. 63, no. 11, pp. 3736–3746, Nov. 2015.
- [21] J. Lee, Y.-A. Li, M.-H. Hung, and S.-J. Huang, "A fully-integrated 77-GHz FMCW radar transceiver in 65-nm CMOS technology," *IEEE Journal of Solid-State Circuits*, vol. 45, no. 12, pp. 2746–2756, 2010.
- [22] L. Wang, S. Glisic, J. Borngraeber, W. Winkler, and J. C. Scheytt, "A single-ended fully integrated SiGe 77/79 GHz receiver for automotive radar," *IEEE J. Solid-State Circuits*, vol. 43, no. 9, pp. 1897–1908, Sep. 2008.
- [23] Z. Chen, C. Wang, H. Yao, and P. Heydari, "A BiCMOS W-band 2×2 focal-plane array with on-chip antenna," *IEEE J. Solid-State Circuits*, vol. 47, no. 10, pp. 2355–2371, Oct. 2012.

- [24] N. Pohl, T. Jaeschke, and K. Aufinger, "An ultra-wideband 80 GHz FMCW radar system using a SiGe bipolar transceiver chip stabilized by a fractional-N PLL synthesizer," *IEEE Trans. Microw. Theory Tech.*, vol. 60, no. 3, pp. 757–765, Mar. 2012.
- [25] S. Trotta, M. Wintermantel, J. Dixon, U. Moeller, R. Jammers, T. Hauck, A. Samulak, B. Dehlink, K. Shun-Meen, H. Li, A. Ghazinour, Y. Yin, S. Pacheco, R. Reuter, S. Majied, D. Moline, T. Aaron, V. P. Trivedi, D. J. Morgan, and J. John, "An RCP packaged transceiver chipset for automotive LRR and SRR systems in SiGe BiCMOS technology," *IEEE Trans. Microw. Theory Tech.*, vol. 60, no. 3, pp. 778–794, Mar. 2012.
- [26] R. Feger, C. Wagner, S. Schuster, S. Scheiblhofer, H. Jager, and A. Stelzer, "A 77-GHz FMCW MIMO radar based on an SiGe single-chip transceiver," *IEEE Trans. Microw. Theory Tech.*, vol. 57, no. 5, pp. 1020–1035, May 2009.
- [27] S. T. Nicolson, K. H. K. Yau, S. Pruvost, V. Danelon, P. Chevalier, P. Garcia, A. Chantre, B. Sautreuil, and S. P. Voinigescu, "A low-voltage SiGe BiCMOS 77-GHz automotive radar chipset," *IEEE Trans. Microw. Theory Tech.*, vol. 56, no. 5, pp. 1092–1104, May 2008.
- [28] S. T. Nicolson, P. Chevalier, B. Sautreuil, and S. P. Voinigescu, "Single-chip W-band SiGe HBT transceivers and receivers for doppler radar and millimeter-wave imaging," *IEEE J. Solid-State Circuits*, vol. 43, no. 10, pp. 2206–2217, Oct. 2008.
- [29] V. Jain, F. Tzeng, L. Zhou, and P. Heydari, "A single-chip dual-band 22–29-GHz/77–81-GHz BiCMOS transceiver for automotive radars," *IEEE J. Solid-State Circuits*, vol. 44, no. 12, pp. 3469–3485, Dec. 2009.
- [30] T. Mitomo, N. Ono, H. Hoshino, Y. Yoshihara, O. Watanabe, and I. Seto, "A 77 GHz 90 nm CMOS transceiver for FMCW radar applications," *IEEE J. Solid-State Circuits*, vol. 45, no. 4, pp. 928–937, Apr. 2010.
- [31] B.-H. Ku, O. Inac, M. Chang, H.-H. Yang, and G. M. Rebeiz, "A high-linearity 76-85 GHz 16-element 8-transmit/8-receive phased-array chip with high isolation and flip-chip packaging," *IEEE Transactions on Microwave Theory and Techniques*, vol. 62, no. 10, pp. 2337–2356, 2014.
- [32] B. P. G. et al., "A multimode 76-to-81GHz automotive radar transceiver with autonomous monitoring," in *IEEE Int. Solid-State Circuits Conf. (ISSCC) Dig. Tech. Papers*, Feb. 2018, pp. 158–160.
- [33] J. Hasch, E. Topak, R. Schnabel, T. Zwick, R. Weigel, and C. Waldschmidt, "Millimeter-wave technology for automotive radar sensors in the 77 GHz frequency band," *IEEE Transactions on Microwave Theory and Techniques*, vol. 60, no. 3, pp. 845–860, 2012.
- [34] M. C. Budge and M. P. Burt, "Range correlation effects in radars," in *Radar Conference*, 1993., Record of the 1993 IEEE National. IEEE, 1993, pp. 212–216.
- [35] H. Jia, L. Kuang, W. Zhu, Z. Wang, F. Ma, Z. Wang, and B. Chi, "A 77 GHz frequency doubling two-path phased-array FMCW transceiver for automotive radar," IEEE J. Solid-State Circuits, vol. 51, no. 10, pp. 2299–2311, Oct. 2016.

- [36] Y. H. et al., "A 77-GHz 2T6R transceiver with injection-lock frequency sextupler using 65-nm CMOS for automotive radar system application," *IEEE Trans. Microw. Theory Tech.*, vol. 64, no. 10, pp. 3031–3048, Oct. 2016.
- [37] B. Ku, O. Inac, M. Chang, H. Yang, and G. M. Rebeiz, "A high-linearity 76-85-GHz 16-element 8-transmit/8-receive phased-array chip with high isolation and flip-chip packaging," *IEEE Trans. Microw. Theory Tech.*, vol. 62, no. 10, pp. 2337–2356, Oct. 2014.
- [38] B. Ku, P. Schmalenberg, O. Inac, O. D. Gurbuz, J. S. Lee, K. Shiozaki, and G. M. Rebeiz, "A 77-81-GHz 16-element phased-array receiver with ±50° beam scanning for advanced automotive radars," *IEEE Trans. Microw. Theory Tech.*, vol. 62, no. 11, pp. 2823–2832, Nov. 2014.
- [39] 76-77 GHz RF transmitter front-end for W-band radar applications, NXP Semiconductors, 8 2016, rev. 2.0.
- [40] 76-77 GHz RF receiver front-end for W-band radar applications, NXP Semiconductors, 9 2016, rev. 2.0.
- [41] AWR1642 Single-Chip 77- and 79-GHz FMCW Radar Sensor, Texas Instruments, 4 2018, rev. 2.0.
- [42] J. D. Adam, L. E. Davis, G. F. Dionne, E. F. Schloemann, and S. N. Stitzer, "Ferrite devices and materials," *IEEE Trans. Microw. Theory Tech.*, vol. 50, no. 3, pp. 721– 737, Mar. 2002.
- [43] M. Porranzl, C. Wagner, H. Jaeger, and A. Stelzer, "An active quasi-circulator for 77 GHz automotive FMCW radar systems in SiGe technology," *IEEE Microw. Wireless Compon. Lett.*, vol. 25, no. 5, pp. 313–315, May 2015.
- [44] S. Hung, Y. Lee, C. Su, and Y. Wang, "High-isolation millimeter-wave subharmonic monolithic mixer with modified quasi-circulator," *IEEE Trans. Microw. Theory Tech.*, vol. 61, no. 3, pp. 1140–1149, Mar. 2013.
- [45] J. Chang, J. Kao, Y. Lin, and H. Wang, "Design and analysis of 24-GHz active isolator and quasi-circulator," *IEEE Trans. Microw. Theory Tech.*, vol. 63, no. 8, pp. 2638–2649, Aug. 2015.
- [46] T. Kijsanayotin and J. F. Buckwalter, "Millimeter-wave dual-band, bidirectional amplifier and active circulator in a CMOS SOI process," *IEEE Trans. Microw. Theory Tech.*, vol. 62, no. 12, pp. 3028–3040, Dec. 2014.
- [47] N. Reiskarimian and H. Krishnaswamy, "Magnetic-free non-reciprocity based on staggered commutation," *Nature communications*, vol. 7, p. 11217, 2016.
- [48] T. Dinc and H. Krishnaswamy, "17.2 a 28GHz magnetic-free non-reciprocal passive CMOS circulator based on spatio-temporal conductance modulation," in 2017 IEEE International Solid-State Circuits Conference (ISSCC), Feb 2017, pp. 294–295.
- [49] T. Dinc, A. Nagulu, and H. Krishnaswamy, "A millimeter-wave non-magnetic passive SOI CMOS circulator based on spatio-temporal conductivity modulation," *IEEE J. Solid-State Circuits*, vol. 52, no. 12, pp. 3276–3292, Dec. 2017.

- [50] A. Medra, D. Guermandi, K. Vaesen, S. Brebels, A. Bourdoux, W. V. Thillo, P. Wambacq, and V. Giannini, "An 80 GHz low-noise amplifier resilient to the TX spillover in phase-modulated continuous-wave radars," *IEEE Journal of Solid-State Circuits*, vol. 51, no. 5, pp. 1141–1153, May 2016.
- [51] J.-G. Kim, S. Ko, S. Jeon, J.-W. Park, and S. Hong, "Balanced topology to cancel Tx leakage in CW radar," *IEEE Microwave and Wireless Components Letters*, vol. 14, no. 9, pp. 443–445, Sept 2004.
- [52] C. Kim, J. Kim, and S. Hong, "A quadrature radar topology with Tx leakage canceller for 24-GHz radar applications," *IEEE Transactions on Microwave Theory and Techniques*, vol. 55, no. 7, pp. 1438–1444, July 2007.
- [53] G. Pyo, C. Kim, and S. Hong, "Single-antenna FMCW radar CMOS transceiver IC," IEEE Transactions on Microwave Theory and Techniques, vol. 65, no. 3, pp. 945–954, March 2017.
- [54] K. Lin, Y. E. Wang, C. Pao, and Y. Shih, "A ka-band fmcw radar front-end with adaptive leakage cancellation," *IEEE Transactions on Microwave Theory and Techniques*, vol. 54, no. 12, pp. 4041–4048, Dec 2006.
- [55] H. K. et al., "A fully integrated 60-GHz CMOS direct-conversion doppler radar RF sensor with clutter canceller for single-antenna noncontact human vital-signs detection," *IEEE Trans. Microw. Theory Tech.*, vol. 64, no. 4, pp. 1018–1028, Apr. 2016.
- [56] P. D. L. Beasley, A. G. Stove, B. J. Reits, and B. As, "Solving the problems of a single antenna frequency modulated CW radar," in *IEEE Int. Conf. Radar*, May 1990, pp. 391–395.
- [57] B. Razavi, "Translational circuits [a circuit for all seasons]," *IEEE Solid-State Circuits Magazine*, vol. 8, no. 1, pp. 8–13, winter 2016.
- [58] Y. Zhao, S. Hemour, T. Liu, and K. Wu, "Nonuniformly distributed electronic impedance synthesizer," *IEEE Trans. Microw. Theory Tech.*, vol. 66, no. 11, pp. 4883–4897, Nov. 2018.
- [59] W. Bischof, "Variable impedance tuner for MMIC's," *IEEE Microw. Guided Wave Lett.*, vol. 4, no. 6, pp. 172–174, Jun. 1994.
- [60] J. Papapolymerou, K. L. Lange, C. L. Goldsmith, A. Malczewski, and J. Kleber, "Reconfigurable double-stub tuners using MEMS switches for intelligent RF frontends," *IEEE Trans. Microw. Theory Tech.*, vol. 51, no. 1, pp. 271–278, Jan. 2003.
- [61] Z. Iskandar, J. Lugo-Alvarez, A. Bautista, E. Pistono, F. Podevin, V. Puyal, A. Siligaris, and P. Ferrari, "A 30–50 GHz reflection-type phase shifter based on slow-wave coupled lines in BiCMOS 55 nm technology," in 2016 46th European Microwave Conference (EuMC), Oct. 2016, pp. 1413–1416.
- [62] R. B. Yishay and D. Elad, "A 57–66 GHz reflection-type phase shifter with near-constant insertion loss," in 2016 IEEE MTT-S International Microwave Symposium (IMS), May 2016, pp. 1–4.

- [63] C. Chang, Y. Chen, and S. Hsieh, "A V-band three-state phase shifter in CMOS-MEMS technology," *IEEE Microw. Wireless Compon. Lett.*, vol. 23, no. 5, pp. 264–266, May 2013.
- [64] R. S. Engelbrecht and K. Kurokawa, "A wide-band low noise L-band balanced transistor amplifier," *Proc. IEEE*, vol. 53, no. 3, pp. 237–247, Mar. 1965.
- [65] M. Kalantari, X. Meng, A. Fotowat-Ahmady, and C. P. Yue, "A tunable reflection/transmission coefficient circuit using a 45° hybrid coupler with two orthogonal variables," *IEEE Trans. Microw. Theory Tech.*, vol. 67, no. 4, pp. 1402–1411, Apr. 2019.
- [66] H. Rashid, P. Y. Aghdam, D. Meledin, V. Desmaris, and V. Belitsky, "Wideband planar hybrid with ultralow amplitude imbalance," *IEEE Microw. Wireless Compon. Lett.*, vol. 27, no. 3, pp. 230–232, Mar., 2017.
- [67] H. J. Yoon and B. W. Min, "Two section wideband 90° hybrid coupler using parallel-coupled three-line," *IEEE Microw. Wireless Compon. Lett.*, vol. 27, no. 6, pp. 548–550, Jun. 2017.
- [68] M. E. Bialkowski and Y. Wang, "Wideband microstrip 180° hybrid utilizing ground slots," *IEEE Microw. Wireless Compon. Lett.*, vol. 20, no. 9, pp. 495–497, Sep. 2010.
- [69] W.-S. Tung, H.-H. Wu, and Y.-C. Chiang, "Design of microwave wide-band quadrature hybrid using planar transformer coupling method," *IEEE Trans. Microw. Theory Tech.*, vol. 51, no. 7, pp. 1852–1856, Jul. 2003.
- [70] S. Reshma and M. K. Mandal, "Miniaturization of a 90° hybrid coupler with improved bandwidth performance," *IEEE Microw. Wireless Compon. Lett.*, vol. 26, no. 11, pp. 891–893, Nov. 2016.
- [71] J. Kim and J. G. Yook, "A miniaturized 3 dB 90° hybrid coupler using coupledline section with spurious rejection," *IEEE Microw. Wireless Compon. Lett.*, vol. 24, no. 11, pp. 766–768, Nov. 2014.
- [72] V. Napijalo, "Coupled line 180° hybrids with Lange couplers," *IEEE Trans. Microw. Theory Tech.*, vol. 60, no. 12, pp. 3674–3682, Dec. 2012.
- [73] J. Reed and G. J. Wheeler, "A method of analysis of symmetrical four-port networks," *IRE Trans. Microw. Theory Techn.*, vol. 4, no. 4, pp. 246–252, Oct. 1956.
- [74] Noise figure measurement accuracy: The Y-factor method. Keysight Technology. [Online]. Available: http://literature.cdn.keysight.com/litweb/pdf/5952-3706E.pdf
- [75] K. W. Goossen, "On the design of coplanar bond wires as transmission lines," *IEEE Microw. Guided Wave Lett.*, vol. 9, no. 12, pp. 511–513, Dec. 1999.
- [76] S. Beer, C. Rusch, B. Göttel, H. Gulan, T. Zwick, M. Zwyssig, and G. Kunkel, "A self-compensating 130-GHz wire bond interconnect with 13% bandwidth," in 2013 IEEE Antennas and Propagation Society International Symposium (APSURSI), Jul. 2013, pp. 2133–2134.

- [77] A. M. et al., "An 80 GHz low-noise amplifier resilient to the TX spillover in phase-modulated continuous-wave radars," *IEEE J. Solid-State Circuits*, vol. 51, no. 5, pp. 1141–1153, May 2016.
- [78] G. Pyo, C. Kim, and S. Hong, "Single-antenna FMCW radar CMOS transceiver IC," *IEEE Trans. Microw. Theory Tech.*, vol. 65, no. 3, pp. 945–954, Mar. 2017.
- [79] H. Chou, Y. Kao, C. Peng, Y. Wang, and T. Chu, "An X-band frequency-modulated continuous-wave radar sensor system with a single-antenna interface for ranging applications," *IEEE Trans. Microw. Theory Tech.*, vol. 66, no. 9, pp. 4216–4231, Sep. 2018.